Fermi National Accelerator Laboratory

TM-1528

# Study of Two-Dimensional Transient Cavity Fields Using the Finite-Difference Time-Domain Technique

James L. Crisp
Fermi National Accelerator Laboratory
P.O. Box 500, Batavia, Illinois 60510

June 1988

Operated by Universities Research Association Inc. under contract with the United States Department of Energy

Fermilab

TM-1528

# STUDY OF TWO-DIMENSIONAL TRANSIENT CAVITY FIELDS USING THE FINITE-DIFFERENCE TIME-DOMAIN TECHNIQUE

June 1988

James L. Crisp

TABLE OF CONTENTS

LIST OF FIGURES

LIST OF FIGURES (continued)

# LIST OF ABBREVIATIONS

| | |
|---|---|
| MOM | Method of moments |
| FD-TD | Finite-difference time-domain |
| FIT | Finite-integration theory |
| TM | Transverse magnetic |
| TE | Transverse electric |
| GHz | $10^9$ hertz |
| MHz | $10^6$ hertz |
| KHz | $10^3$ hertz |
| psec | $10^{-12}$ seconds |
| nsec | $10^{-9}$ seconds |
| Q | Quality factor of resonator |
| j | Square root of minus one |

## SUMMARY

This study concerns the application of the finite-difference time-domain, or FD-TD, technique to the analysis of transient cavity fields. In order to reduce the amount of computer time required, and to simplify the understanding of the results, only two-dimensional cases were considered. The results, however, are applicable to the study of three-dimensional cases. In two dimensions Maxwell's equations reduce to two orthogonal sets classified, according to their field polarization, as the transverse electric, or TE, and transverse magnetic, or TM, cases. Both are considered here. In order to verify the FD-TD results, an alternative approach using the method of moments, or MOM, technique was implemented to calculate the surface currents. The derivation of the algorithms used for both the FD-TD and MOM codes are presented.

The first scatterer modeled was an infinitely long solid square copper cylinder. This geometry provided a simple test case to become acquainted with the FD-TD code used. It also proved to be a simple geometry to solve with the MOM technique. Using a rectangular cross section allowed the square discretizations of space to conform perfectly with the surface of the scatterer.

The two-dimensional cavity geometry chosen was a hollow slotted cavity with an outside dimension coincident with that of the solid square cylinder. The infinite slot provided the means of exciting

the interior with an external plane wave traveling along the y axis.

For both the TE and TM polarizations, the surface current was used to compare the FD-TD and MOM results. The MOM algorithm solved for the surface currents directly. For the FD-TD method, the surface currents were calculated from the magnetic fields at the surface of the scatterer.

The FD-TD code was then modified to investigate the surface current amplitude in the time domain. For the TM polarization the pole at zero frequency, due to an infinite length, was found to have a significant effect. For the TE polarization a mode related to the circumference of the scatterer is revealed. A fast fourier transform applied to the time domain data helped to identify these phenomena.

In order to excite more than one mode at a time, the incident plane wave was given a gaussian time dependance. Results of the application of a fourier transform to this time domain data are presented. To improve the fourier transform results, the application of several types of time domain windows are discussed.

# I. INTRODUCTION

## 1.1 Purpose for study

Many devices are used in a particle accelerator, such as the one at Fermi Laboratory, to interact with the electromagnetic fields of the particle beam. Resonant radio-frequency cavities are used to accelerate the beam, large high field magnets are used to steer the beam, and a variety of detectors are used to monitor such things as beam position, intensity, and density. All share the common trait of interacting with electromagnetic fields. As the understanding of these devices improves, higher energy, more efficient, and more reliable accelerators can be built. Since Fermi Lab has been commissioned, theorists have come to realize that even the shape of the vacuum chamber the beam travels in plays an important role in the stability of the beam. Resonant structures such as vacuum bellows, detectors, or cavities can induce modulations, or instabilities in the beam if the fields generated by the beam passing through them are of sufficient amplitude. These instabilities cause the beam to dilute, which either limits maximum intensity, or requires larger aperture, or equivalently more expensive machines (8).

This work is intended to be a study into the application of the finite-difference time-domain, or FD-TD technique, to some of the problems faced by designers of equipment used in modern accelerators. In particular it discusses using the FD-TD algorithm

to study the field distribution of a simple two-dimensional cavity in both space and time.

The frequency range of interest is limited to essentially DC to several gigahertz. The interaction of passive devices with the beam is through the frequency components contained within the beam current. For circular accelerators, the lowest possible frequencies of interest are the go-around rate and its harmonics, the order of 10 to 100 KHz. Such things as intentional beam steering and synchrotron frequencies may be disregarded as these are easily controllable by other methods. Lower frequencies are usually not a problem as the fields required to significantly affect the beam increase as the frequency decreases. An upper frequency limit is set by the beam's velocity and the required clear aperture. The electromagnetic fields of a relativistic point charge are contained within an angle given roughly by 1/gamma, where gamma is the ratio of its total energy to its rest energy. Thus for a particle velocity of .9 times the speed of light and an aperture of 2 cm, the fields would be .84 cm wide at the inside surface of any device. Equating this to a wavelength, the highest frequency is about 3.6 GHz. Another upper frequency limit is the cutoff frequency of the beam tube. Rather than building up, the fields within a spurious resonator can propagate away.

The FD-TD algorithm is particularly well suited for this purpose as it uses a time stepping algorithm to solve Maxwell's curl equations in the time domain. As implemented here, the time

dependence of the incident plane wave is easily modified to the users specification. This allows studying the results directly in the time domain or alternatively using a Fourier transform to investigate the frequency response.

## 1.2 Background

In general, analytic solutions to Maxwell's equations cannot be found. With exception for a few special two-dimensional cases such as the circular cylinder. For three dimensions, only the spherical geometry has been solved. Asymptotic and series approximations have been used to extend solutions to slightly more complex shapes. The use of analytic solutions limits the design of devices to shapes approximating ones with known solutions. Because of the approximations used, models must be constructed and tested in order to verify their performance. This can be an expensive and time consuming process.

Numerical solutions to Maxwell's equations performed on a computer, have proven a powerful and versatile tool. They can be used with all types of materials including mixtures of inhomogeneous, anisotropic and nonlinear. They are applicable to all frequency ranges from magnetostatic or electrostatic to microstrip and microwave circuits. The bandwidth of a particular model is limited by computer storage and running time. However, three-dimensional FD-TD codes have been used with structures spanning up to nine wavelengths (11).

The most versatile and widely used techniques involve using a first order accurate numerical approximation to either Maxwell's integral or differential equations. Space is discretized into rectangular cells with each scaler field quantity defined at an appropriate location within each cell. The scatterer is specified with the permittivity, permeability, electrical conductivity, and magnetic resistivity at each field location. The techniques can be implemented in either the frequency or time domain. For the frequency domain, a single frequency is assumed and the time derivatives of a scaler field quantity are replaced with $j\omega$ times that quantity. For time domain solutions, the time derivative is replaced with a difference equation. Frequency domain solutions for high Q cavity modes are usually performed more efficiently by formulating a matrix whose eigenvalues characterize those modes (14).

The finite-integral theory, or FIT, and the finite-difference time-domain, or FD-TD, methods reduce to identical difference equations and are thus synonymous, provided rectangular cells are used to discretize the volume of space being modeled. The stepped edge approximation to curved surfaces can have anomalous effects if the wavelength used approaches the cell size. Recent work has provided a solution to this problem by imposing Faraday's law in integral form to the intersection of the spatial cells and the curved surface (15). This effectively allows a curved surface to slice through the appropriate cells.

Reference (9) provides an excellent introduction to some of the current uses of the FD-TD technique. They include penetration of narrow slots and lapped joints, coupling of wires and wire bundles, penetration of biological tissue, scattering by relativistically moving surfaces, and inverse scattering reconstructions in one and two dimensions.

Existing programs commonly used for the calculation of electromagnetic fields in the accelerator community include the following:

POISSON calculates electrostatic and magnetostatic fields (1).

SUPERFISH computes resonant frequencies and fields in radio-frequency cavities using linear dielectric and magnetic materials and triangular cells (1).

URMEL uses the FIT method to formulate a matrix which is used to solve for the eigenmodes of high Q cavities (14, 17).

TBCI uses the FIT method in the time domain to calculate beam wake fields (15, 17).

MAFIA is a combination of three-dimensional versions of URMEL and TBCI within one integrated program (17).

The FD-TD code used in these studies was authored by Dr. Allen Taflove at Northwestern University. The code is documented in reference (10). This code, unlike the above, has implemented a radiation boundary condition which allows modeling fields external to a cavity. Because it solves only two of the four Maxwell's equations it will not work for static fields, however.

# II. THE TWO-DIMENSIONAL FINITE-DIFFERENCE TIME-DOMAIN ALGORITHM

## 2.1 Solving Maxwell's equations

The FD-TD technique is a computer algorithm used in solving Maxwell's curl equations given below. The curl equations will satisfy Maxwell's other two equations, $\nabla \cdot \bar{D} = \rho$ and $\nabla \cdot \bar{B} = 0$, for time varying fields (4).

$$\frac{\partial \bar{H}}{\partial t} = -\frac{1}{\mu} \nabla \times \bar{E} - \frac{\rho_m}{\mu} \bar{H} \tag{2.1}$$

$$\frac{\partial \bar{E}}{\partial t} = \frac{1}{\epsilon} \nabla \times \bar{H} - \frac{\sigma_e}{\epsilon} \bar{E} \tag{2.2}$$

| | | |
|---|---|---|
| E | Electric field | volts/meter |
| H | Magnetic field | amps/meter |
| $\epsilon$ | Permittivity | farads/meter |
| $\mu$ | Permeability | henrys/meter |
| $\sigma_e$ | Electric conductivity | mhos/meter |
| $\rho_m$ | Magnetic resistivity | ohms/meter |

For the three-dimensional case, the FD-TD algorithm divides a volume of space fully containing the scatterer, or cavity, into cubes and assigns the six field quantities Hx, Hy, Hz, Ex, Ey, and Ez to an appropriate location within each cube. The scatterer is specified with the values of permeability, permittivity, electrical conductivity, and magnetic resistivity for each scaler field quantity. On alternate half time steps Hx, Hy, and Hz are determined, then Ex, Ey, and Ez. This will simulate the propagation of an electromagnetic wave though the data space of the model. The radiation boundary condition allows the volume of space being modeled to have a finite size. In order to reduce the

computation time and storage requirements only two-dimensional algorithms are investigated. The results, however, should be applicable to three-dimensional problems.

In order to implement a two-dimensional case, both the excitation and the modeled geometry are not allowed to vary along the z axis. This makes all partial derivatives with respect to z identically zero. With this simplification, Maxwell's curl equations reduce to two orthogonal sets termed the transverse magnetic,or TM, and the transverse electric, or TE, cases.

TM case (Ez, Hx, Hy fields only)

$$\frac{\partial Hx}{\partial t} = -\frac{1}{\mu}\left(\frac{\partial Ez}{\partial y} + \rho_m Hx\right) \tag{2.3}$$

$$\frac{\partial Hy}{\partial t} = \frac{1}{\mu}\left(\frac{\partial Ez}{\partial x} - \rho_m Hy\right) \tag{2.4}$$

$$\frac{\partial Ez}{\partial t} = \frac{1}{\epsilon}\left(\frac{\partial Hy}{\partial x} - \frac{\partial Hx}{\partial y} - \sigma_e Ez\right) \tag{2.5}$$

TE case (Hz, Ex, Ey fields only)

$$\frac{\partial Hz}{\partial t} = \frac{1}{\mu}\left(\frac{\partial Ex}{\partial y} - \frac{\partial Ey}{\partial x} - \rho_m Hz\right) \tag{2.6}$$

$$\frac{\partial Ex}{\partial t} = \frac{1}{\epsilon}\left(\frac{\partial Hz}{\partial y} - \sigma_e Ex\right) \tag{2.7}$$

$$\frac{\partial Ey}{\partial t} = -\frac{1}{\epsilon}\left(\frac{\partial Hz}{\partial x} + \sigma_e Ey\right) \tag{2.8}$$

The above equations are equally valid when applied to total, scattered, or incident fields separately. If used for the total fields, however, the required continuity of the tangential field components at the interface to dissimilar media is automatically accounted for.

It is interesting to note that the TE and TM cases are the dual of each other with the following mapping.

| TM | | TE |
|---|---|---|
| Hx | ⇔ | -Ex |
| Hy | ⇔ | -Ey |
| Ez | ⇔ | Hz |
| $\epsilon$ | ⇔ | $\mu$ |
| $\mu$ | ⇔ | $\epsilon$ |
| $\rho_m$ | ⇔ | $\sigma_e$ |
| $\sigma_e$ | ⇔ | $\rho_m$ |

Thus code written for the TM case is equally applicable to the TE case. The code used for this study, however, did not take advantage of this symmetry and used separate algorithms for the two cases. This requires offsetting the TE and TM fields within the grid. This approach correlates better with the three-dimensional case but requires more computer storage as both cases are solved simultaneously.

In 1966, an algorithm using second-order accurate central-difference approximations for the space and time derivatives of the electric and magnetic fields was introduced (18). A unique point in space and time is specified with the four integer components (i,j,k,n) which represents the point ($i\Delta x, j\Delta y, k\Delta z, n\Delta t$). Using F to denote a generic field quantity Hx, Hy, Hz, Ex, Ey, or Ez the amplitude of a field at a unique point in space and time is specified with;

$$F^n(i,j,k) = F(i\Delta x, j\Delta y, k\Delta z, n\Delta t)$$

The space and time derivatives become;

$$\frac{\partial F^n(i,j,k)}{\partial x} = \frac{F^n(i+1/2,j,k) - F^n(i-1/2,j,k)}{\Delta x} \tag{2.9}$$

$$\frac{\partial F^n(i,j,k)}{\partial t} = \frac{F^{n+1/2}(i,j,k) - F^{n-1/2}(i,j,k)}{\Delta t} \tag{2.10}$$

As seen later, space and time discretizations are selected to bound errors in the sampling process and to insure numerical stability of the algorithm. In all subsequent work it is assumed that $\Delta x = \Delta y = \Delta$. For two-dimensions, the location of the fields within a cell, and the cross section of an arbitrary cavity are shown in figure (2-1) below.

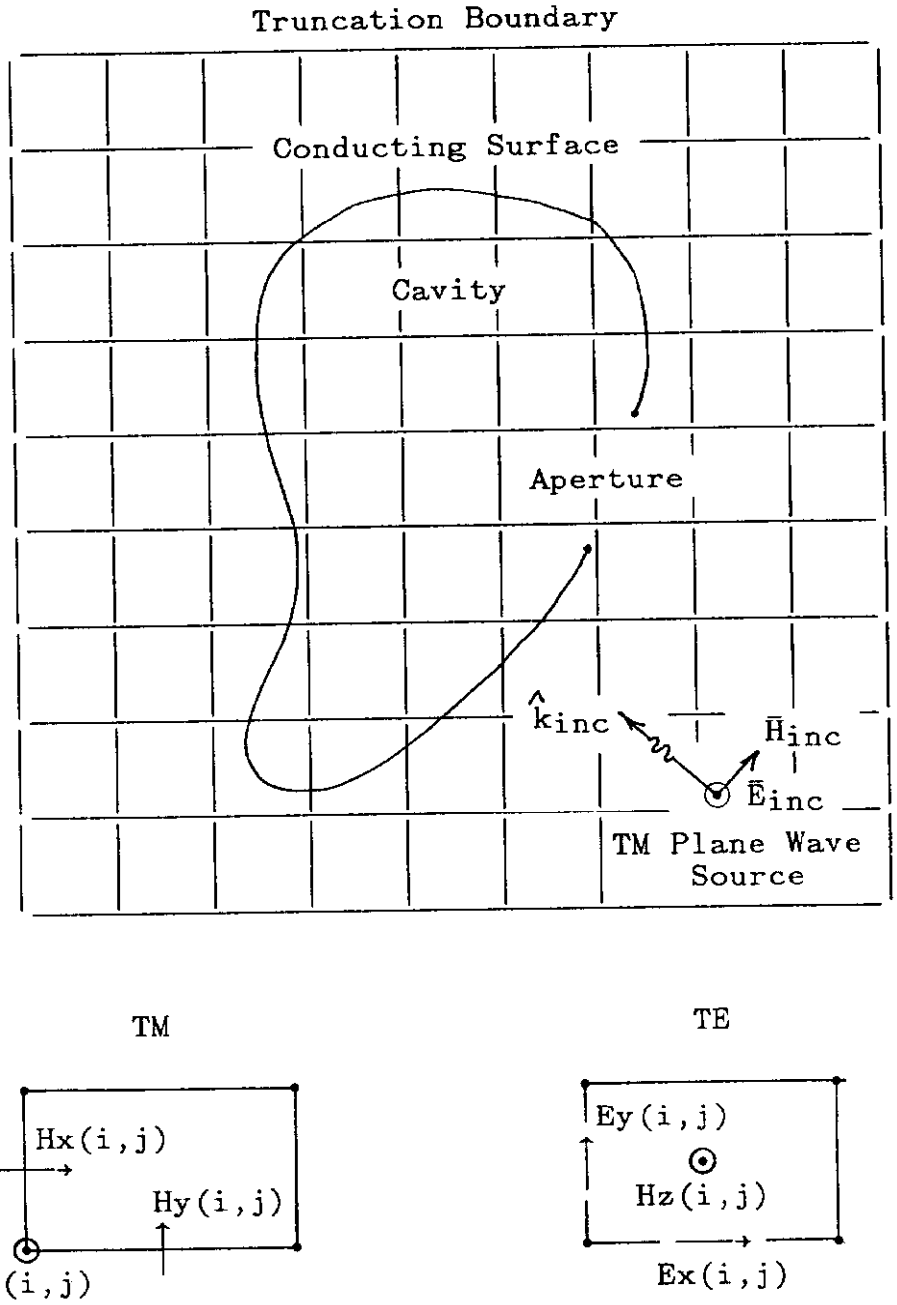


figure 2-1. An arbitrary two-dimensional cavity and the location of field components within the FD-TD cell

Applying the Yee approximations, equations (2.9) and (2.10), to equations (2.3), (2.4), (2.5) and simplifying, the following equivalent equations for the TM case are obtained (18, 13).

$$m = \text{mediaHx}(i,j+1/2)$$

$$Hx^{n+1/2}(i,j+1/2) = Da(m)\ Hx^{n-1/2}(i,j+1/2) + Db(m)\ [Ez^{n}(i,j) - Ez^{n}(i,j+1)] \tag{2.11}$$

$$m = \text{mediaHy}(i+1/2,j)$$

$$Hy^{n+1/2}(i+1/2,j) = Da(m)\ Hy^{n-1/2}(i+1/2,j) + Db(m)\ [Ez^{n}(i+1,j) - Ez^{n}(i,j)] \tag{2.12}$$

$$m = \text{mediaEz}(i,j)$$

$$Ez^{n+1}(i,j) = Ca(m)\ Ez^{n}(i,j) + Cb(m)\ [Hy^{n+1/2}(i+1/2,j) - Hy^{n+1/2}(i-1/2,j) + Hx^{n+1/2}(i,j-1/2) - Hx^{n+1/2}(i,j+1/2)] \tag{2.13}$$

$$Ca(m) = \frac{1 - \frac{\sigma_{\epsilon}(m)\Delta t}{2\epsilon(m)}}{1 + \frac{\sigma_{\epsilon}(m)\Delta t}{2\epsilon(m)}} \tag{2.14}$$

$$Cb(m) = \frac{\Delta t}{\epsilon(m)\Delta}\ \frac{1}{1 + \frac{\rho_m(m)\Delta t}{2\epsilon(m)}} \tag{2.15}$$

$$Da(m) = \frac{1 - \frac{\rho_m(m)\Delta t}{2\mu(m)}}{1 + \frac{\rho_m(m)\Delta t}{2\mu(m)}} \tag{2.16}$$

$$Db(m) = \frac{\Delta t}{\mu(m)\Delta}\ \frac{1}{1 + \frac{\rho_m(m)\Delta t}{2\mu(m)}} \tag{2.17}$$

With only a few types of material being modeled it becomes more efficient to use a media type array which points to the media constants. For example one integer contains 16 bits. This could be allocated to the 3 field quantities Hx, Hy, and Ez with 5 bits for each, these 5 bits could point to $2^5 = 32$ types of media. This will require significantly less computer storage than storing the

two floating point media variables for each field quantity. Again note that Ca is the dual of Da and Cb is the dual of Db.

Looking at equations (2.11), (2.12) and (2.13), an important aspect of the algorithm is revealed. Each new value of the magnetic field at a specific point depends on the same quantity at the same point but one time step earlier and two electric field quantities evaluated one half time step earlier. This is similar for the electric field. Thus, the algorithm first steps through all space points updating the magnetic fields then one half time step later updates all of the electric fields. This calculation is performed in place and does not require extra computer storage. In order to obtain time domain information one must allocate storage and copy the appropriate field quantities at each half time step.

Because it is necessary to discretize both space and time, this algorithm provides a step approximation to smoothly curved surfaces and smoothly changing time domain functions. In many cases this has been found to provide adequate solutions. For the rectangular geometries considered here, the spatial cells conform perfectly to the surface. For curved surfaces, a model has been developed using Faraday's law in the integral form to allow a curved surface to slice the appropriate cells (15).

## 2.2 The total/scattered field interface

The modeled volume of space is divided into two regions: the

total field region near the object and the scattered field region. The interface between these two regions is chosen to be a simple geometry, usually a cube for three dimensions which reduces to a square for two dimensions. Equations (2.11), (2.12) and (2.13) are equally valid within either region, however, steps must be taken at the interface to insure the separation of total and scattered fields. The use of total fields near the object simplifies the calculation of incident waves and improves the dynamic range of the algorithm. Code which keeps track of scattered and incident fields separately must calculate the difference of two possibly large magnitudes at the interface of dissimilar media, if the difference is small, numerical noise will result. This will require the calculation of the incident fields at this possibly complex surface. Use of the scattered field region is required for the application of the radiation boundary condition but also allows the definition of a virtual surface on which the scattered fields are defined and from which the far fields may be calculated, as for the radar cross section.

For the TM case, the necessary corrections applied at the front of the grid, the side parallel with the x axis and nearest to it, are discussed below. The other sides are similar. The interface is chosen to coincide with the Ez field points. Points lying on or inside the interface are defined as representing total field. The simple relation that must be maintained for tangential fields is simply that the total field be continuous. In order to correct the numerical algorithm, Ez incident is required on the interface

at all four sides, Hx incident on the front and back sides, and Hy incident on the right and left sides. Hx and Hy incident are evaluated one half cell outside of the interface. Rewriting equations (2.11) and (2.13) explicitly indicating total, incident, and scattered fields, the correction at the interface becomes quite simple. The equations for Hx and Ez at the front interface are shown here.

$$\begin{aligned} Hx_{scat}^{n+1/2}(i,j-1/2) &= Da(m)\ Hx_{scat}^{n-1/2}(i,j-1/2) \\ &\quad + Db(m)\ [Ez_{tot}^{n}(i,j) - Ez_{scat}^{n}(i,j-1)] \\ &\quad - Db(m)\ Ez_{inc}^{n}(i,j) \\ &= Hx^{n+1/2}(i,j-1/2)\Big|_{Yee} + Db(m)\ Ex_{inc}^{n}(i,j) \end{aligned} \tag{2.18}$$

$$\begin{aligned} Ez_{tot}^{n+1}(i,j) &= Ca(m)\ Ez_{tot}^{n}(i,j) \\ &\quad + Cb(m)\ [Hy_{tot}^{n+1/2}(i+1/2,j) - Hy_{tot}^{n+1/2}(i-1/2,j) \\ &\quad + Hx_{scat}^{n+1/2}(i,j-1/2) - Hx_{tot}^{n+1/2}(i,j+1/2)] \\ &= Ez^{n+1}(i,j)\Big|_{Yee} + Cb(m)\ Hx_{inc}^{n+1/2}(i,j-1/2) \end{aligned} \tag{2.19}$$

The correction is performed by adding the appropriate incident fields to those given by the numerical algorithm at the surface of the interface, equations (2.11) through (2.13). At the corners, Ez requires two extra terms. This can be absorbed into the algorithm easily by allowing it to operate on the corner value while correcting both adjacent sides. As described in the next section, these equations allow the introduction of arbitrary incident fields.

## 2.3 Excitation with the incident fields

In order to improve the efficiency or decrease the number of calculations, a look-up table method is used to determine the required incident field values. The total/scattered field boundary with an incident plane wave is shown in figure (2-2). The angle of incidence with respect to the x axis is $\phi$ where $0 \leq \phi < 90°$.

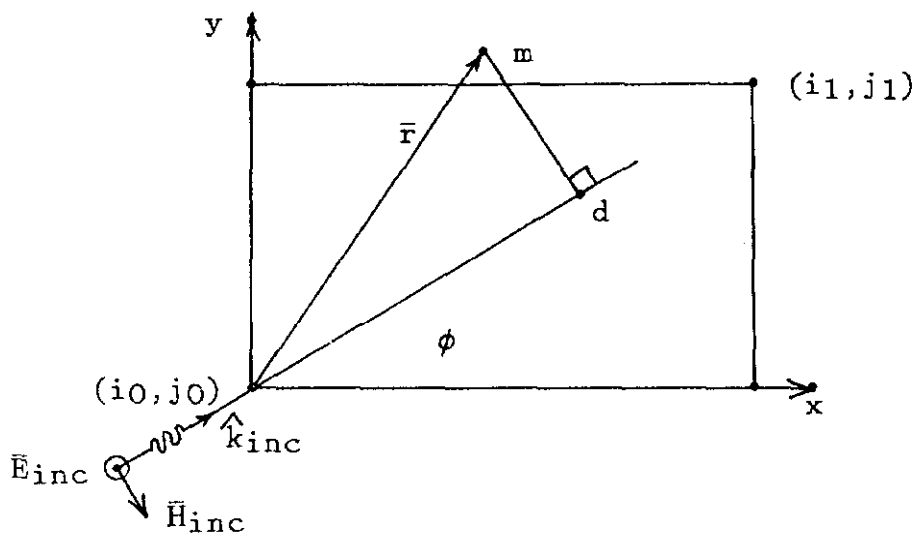


figure 2-2. Incident plane wave with total/scattered field interface.

The incident plane wave will make initial contact with the lower left corner. The time required to reach a point m, where the incident field is to be calculated, is the same as the time required for the wave to travel from the initial contact corner to point d. This is the basis for the look-up table approach. Simulate the propagation of a plane wave along a one-dimensional grid parallel with the unit $\hat{k}_{inc}$ vector. In order to calculate a

field quantity at point m, d is determined and a linear interpolation is used between discrete steps in the one-dimensional grid. Letting $i_c$ and $j_c$ represent the x and y coordinates of the first corner the plane wave reaches, then the following relations are used.

$$\begin{aligned}
0° \le \phi < 90° \quad & (i_c, j_c) = (i_0, j_0) \\
90° \le \phi < 180° \quad & (i_1, j_0) \\
180° \le \phi < 270° \quad & (i_1, j_1) \\
270° \le \phi < 360° \quad & (i_0, j_1)
\end{aligned}$$

$$\hat{k}_{inc} = (\cos\phi, \sin\phi)$$

$$\bar{r}(m) = (i-i_c, j-j_c) \quad \text{for } m = (i,j)$$

$$d = |(i-i_c)\cos\phi, (j-j_c)\sin\phi|$$

In order to generate the look-up table, or propagate the incident wave, equations (2.11), (2.12) and (2.13) are simplified to one dimension below.

$$H_{inc}^{n+1/2}(d+1/2) = H_{inc}^{n-1/2}(d+1/2) + \frac{\Delta t}{\mu\Delta \frac{v_p(\phi=0°)}{v_p(\phi)}} [E_{inc}^{n+1/2}(d) - E_{inc}^{n}(d+1)] \tag{2.20}$$

$$E_{inc}^{n+1}(d) = E_{inc}^{n}(d) + \frac{\Delta t}{\epsilon\Delta \frac{v_p(\phi=0°)}{v_p(\phi)}} [H_{inc}^{n+1/2}(d-1/2) - H_{inc}^{n+1/2}(d+1/2)] \tag{2.21}$$

The ratio $v_p(\phi=0°)/v_p(\phi)$ is used to adjust $\Delta$ so that the wave propagates along the one-dimensional grid at the same velocity it

would propagate along the $\hat{k}_{inc}$ direction in the two-dimensional grid. This will be discussed more thoroughly in section 2.5 which covers dispersion. The required x and y components of the field are extracted from the incident components according to the following relations.

$$Hx_{inc}(d) = H_{inc}(d)\sin(\phi)$$
$$Hy_{inc}(d) = -H_{inc}(d)\cos(\phi)$$
$$Ez_{inc}(d) = E_{inc}(d)$$

To induce a wave on the one-dimensional grid, simply set one end point electric field to the time function required. If $d_c$ is the point coincident with the corner and $d_c$-2 is the first point in the grid then the following relation is used.

$$E_{inc}^{n}(d_c-2) = E_o\, g(n\Delta t) \qquad (2.22)$$

The magnetic field quantities will be generated by the FD-TD algorithm one half time step and one half cell later. In order to terminate the end of the grid, the last point is set to the previous value of the next to the last point as shown below.

$$Ez^{n+1}(last) = Ez^{n}(last-1) \qquad (2.23)$$
$$Ez^{n+1}(last-1) = Ez^{n+1}(last-1)\Big|_{Yee} \qquad (2.24)$$

The magnetic field is terminated similarly. This is equivalent to the wave traveling through the boundary and is an exact solution, at least to the order of the numerical resolution of the computer, for the one-dimensional case.

## 2.4 The radiation boundary condition

The computation zone or lattice is limited in size by the amount of computer memory available. In order to eliminate the simulated reflection of waves from the lattice truncation planes a radiation boundary condition is applied. Basically, a "one-way" wave equation is enforced on the tangential field components at the boundary.

Assuming two dimensions, the wave equation operating on a generic scaler field component, can be expressed in operator form (13).

$$\left(\nabla^2 - \frac{1}{c^2}\frac{\partial^2}{\partial t^2}\right)F = 0$$

$$LF = (Dxx + Dyy - \frac{1}{c^2}Dtt)F = \left(\frac{\partial^2}{\partial x^2} + \frac{\partial^2}{\partial y^2} - \frac{1}{c^2}\frac{\partial^2}{\partial t^2}\right)F = 0 \qquad (2.25)$$

dividing L into two parts;

$$LF = L^+L^-F = 0$$

$$L^- \equiv Dx - \frac{Dt}{c}\sqrt{1-S^2} \qquad (2.26)$$

$$L^+ \equiv Dx + \frac{Dt}{c}\sqrt{1-S^2} \qquad (2.27)$$

$$S = \frac{1}{c}\frac{Dy}{Dt}$$

The radical term involving S classifies $L^-$ and $L^+$ as a pseudo differential operator that is nonlocal in both space and time. In equations (2.26) and (2.27), $L^-$ represents a "one-way" wave equation for waves traveling in the negative x direction with $L^+$

for the positive x direction. Exchanging Dx and Dy provides the relations for the y direction.

It has been shown in (2) that that equations (2.26) and (2.27) are exact solutions and would provide perfect absorption if applied to the tangential scaler field components at the lattice truncation boundaries. The presence of the radical prevents an exact implementation, however, a two-term Taylor series approximation as shown below is given in (6).

$$\sqrt{1-S^2} \simeq 1 - S^2/2 \tag{2.28}$$

or for a negative x directed plane wave;

$$L^- F = \left(Dx - \frac{Dt}{c} + \frac{c}{2}\frac{Dyy}{Dt}\right) F = 0 \tag{2.29}$$

multiplying by Dt and expanding;

$$\left(\frac{\partial}{\partial x}\frac{\partial}{\partial t} - \frac{1}{c}\frac{\partial^2}{\partial t^2} + \frac{c}{2}\frac{\partial^2}{\partial y^2}\right) F = 0 \tag{2.30}$$

Equation (2.30) is a "one-way" wave equation for the negative x direction. The equations for the other three directions are similar. The same set of equations have been derived by factoring the dispersion relation and using a similar approximation for the radical term (12).

The finite differencing scheme for equation (2.30) was originally developed in (6), however the equations illustrated here for two dimensions at the left boundary were obtained from (13).

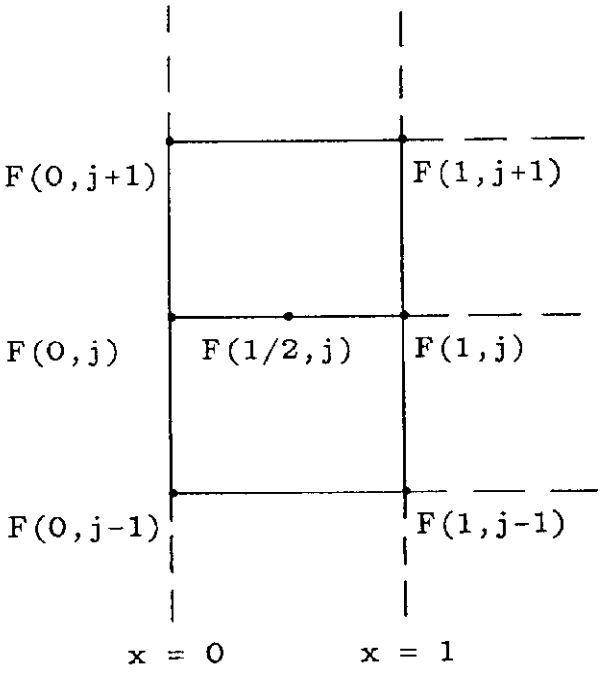


figure 2-3. Field points used to apply the radiation boundary condition on the left side.

$$Dxt\ F^n(1/2,j) = \frac{\frac{\partial}{\partial x} F^{n+1}(1/2,j) - \frac{\partial}{\partial x} F^{n-1}(1/2,j)}{2\Delta t} \qquad (2.31)$$

$$= \frac{\left[\frac{F^{n+1}(1,j) - F^{n+1}(0,j)}{\Delta}\right] + \left[\frac{F^{n-1}(1,j) - F^{n-1}(0,j)}{\Delta}\right]}{2\Delta t}$$

$$Dtt\ F^n(1/2,j) = \frac{1}{2}\left[\frac{\partial^2}{\partial t^2} F^n(0,j) + \frac{\partial^2}{\partial t^2} F^n(1,j)\right] \qquad (2.32)$$

$$= \frac{1}{2}\left[\frac{[F^{n+1}(0,j) - 2\,F^n(0,j) + F^{n-1}(0,j)]}{\Delta t^2}\right.$$

$$\left. + \frac{[F^{n+1}(1,j) - 2\,F^n(1,j) + F^{n-1}(1,j)]}{\Delta t^2}\right]$$

$$\text{Dyy } F^n(1/2,j) = \frac{1}{2}\left[\frac{\partial 2}{\partial t2} F^n(0,j) + \frac{\partial 2}{\partial y2} F^n(1,j)\right] \tag{2.33}$$

$$= \frac{1}{2}\left[\frac{F^n(0,j+1) - 2F^n(0,j) + F^n(0,j-1)}{\Delta y^2}\right.$$

$$+ \left.\frac{F^n(0,j+1) - 2F^n(1,j) + F^n(1,j-1)}{\Delta y^2}\right]$$

Substituting equations (2.31) through (2.33) into (2.30) and solving for $F^{n+1}(0,j)$ the appropriate radiation boundary condition for the negative x direction is obtained.

$$F^{n+1}(0,j) = -F^{n-1}(1,j) + \frac{c\Delta t - \Delta}{c\Delta t + \Delta}\left[F^{n+1}(1,j) + F^{n-1}(0,j)\right]$$

$$+ \frac{2\Delta}{c\Delta t + \Delta}\left[F^n(0,j) + F^n(1,j)\right] \tag{2.34}$$

$$+ \frac{(c\Delta t)2}{2\Delta(c\Delta t + \Delta)}\left[F^n(0,j+1) - 2F^n(0,j) + F^n(0,j-1)\right.$$

$$+ \left.F^n(1,j+1) - 2F^n(1,j) + F^n(1,j-1)\right]$$

Similar equations may be found for the other three directions.

## 2.5 Numerical stability and dispersion

Numerical stability of the algorithm described in section 2.1 places a restriction on the time step size relative to the grid step size. It is shown in (13) that if the following limit is maintained the code will be stable. The velocity is represented by $v$.

$$\Delta t \leq \frac{1}{v}\frac{1}{\sqrt{\frac{1}{\Delta x^2} + \frac{1}{\Delta y^2} + \frac{1}{\Delta z^2}}} \tag{2.35}$$

or if $\Delta x = \Delta y = \Delta z = \Delta$;

$$\Delta t \leq \frac{\Delta}{v\sqrt{3}}$$

For one dimension the time step must be less than or equal to the amount of time required for an electromagnetic wave to propagate from one grid point to the next. Typically for two dimensions, the time step is chosen as $\Delta/2c$ which provides a satisfactory margin for stability.

The dispersion relation for the three-dimensional FD-TD algorithm is found by substituting the equation of a plane wave for the field quantities into equations (2.11), (2.12) and (2.13). Combining the three equations to remove the field amplitudes results in the dispersion relation below. (13)

$$\left(\frac{1}{v\Delta t}\right)^2 \sin^2\left(\frac{\omega\Delta t}{2}\right) = \left(\frac{1}{\Delta x}\right)^2 \sin^2\left(\frac{k_x\Delta x}{2}\right) + \left(\frac{1}{\Delta y}\right)^2 \sin^2\left(\frac{k_y\Delta y}{2}\right) + \left(\frac{1}{\Delta z}\right)^2 \sin^2\left(\frac{k_z\Delta z}{2}\right) \qquad (2.36)$$

In the limit when $\Delta t$, $\Delta x$, $\Delta y$, and $\Delta z$ go to zero, the ideal dispersion case, which may be derived similarly from Maxwell's equations, is obtained.

$$\frac{\omega^2}{v^2} = k_x^2 + k_y^2 + k_z^2 \qquad (2.37)$$

For two dimensions, with the added simplification that $\Delta x = \Delta y = \Delta$ and allowing $\alpha$ to represent the propagation angle with respect to the x axis, the following equation is obtained.

$$\left(\frac{\Delta}{v\Delta t}\right)^2 \sin^2\left(\frac{\omega\Delta t}{2}\right) = \sin^2\left(\frac{k\ \cos\alpha\ \Delta}{2}\right) + \sin^2\left(\frac{k\ \sin\alpha\ \Delta}{2}\right) \qquad (2.38)$$

The above equation was solved numerically in (13). Figure (2-4) shows the phase velocity versus propagation angle for three grid sizes. Selecting a grid size of $\lambda/20$ results in less than one half of one percent variation in phase velocity with propagation angle. Figure (2-5) shows the dependence of phase velocity on the grid cell size for the two extreme propagation angles 0° and 45°. The propagation velocity goes to zero between a grid size of $\lambda/3$ and $\lambda/2$, depending on propagation angle.

Because the phase velocity decreases with increasing grid size, or equivalently increasing frequency, pulse distortion will occur. This will show up as high frequency ringing on the trailing edge of fast changing fields. There are special cases where there is no dispersion. For three dimensions this occurs when $\Delta t = \Delta/c\sqrt{3}$ and $kx = ky = kz = k/\sqrt{3}$. Equation (2.36) reduces to the ideal case with these substitutions. For one dimension this case is equivalent to setting $\Delta t = \Delta/c$. Figure (2-6) compares a gaussian pulse, with $\sigma_t$ of 796 psec, after propagating 7367 time steps in a one-dimensional FD-TD grid with $\Delta t = \Delta/c$, the ideal case, and $\Delta t = \Delta/2c$. The parameters were chosen to equate with those of the two-dimensional FD-TD test case to be discussed in section 6.4. The grid step size was .0397888 meters and the nominal velocity was c. Figure (2-7) uses the same model parameters as figure (2-6) except with a 5 nsec wide square pulse. Because the rising and falling edges are much faster, there is significantly more ringing after only 393 time steps.

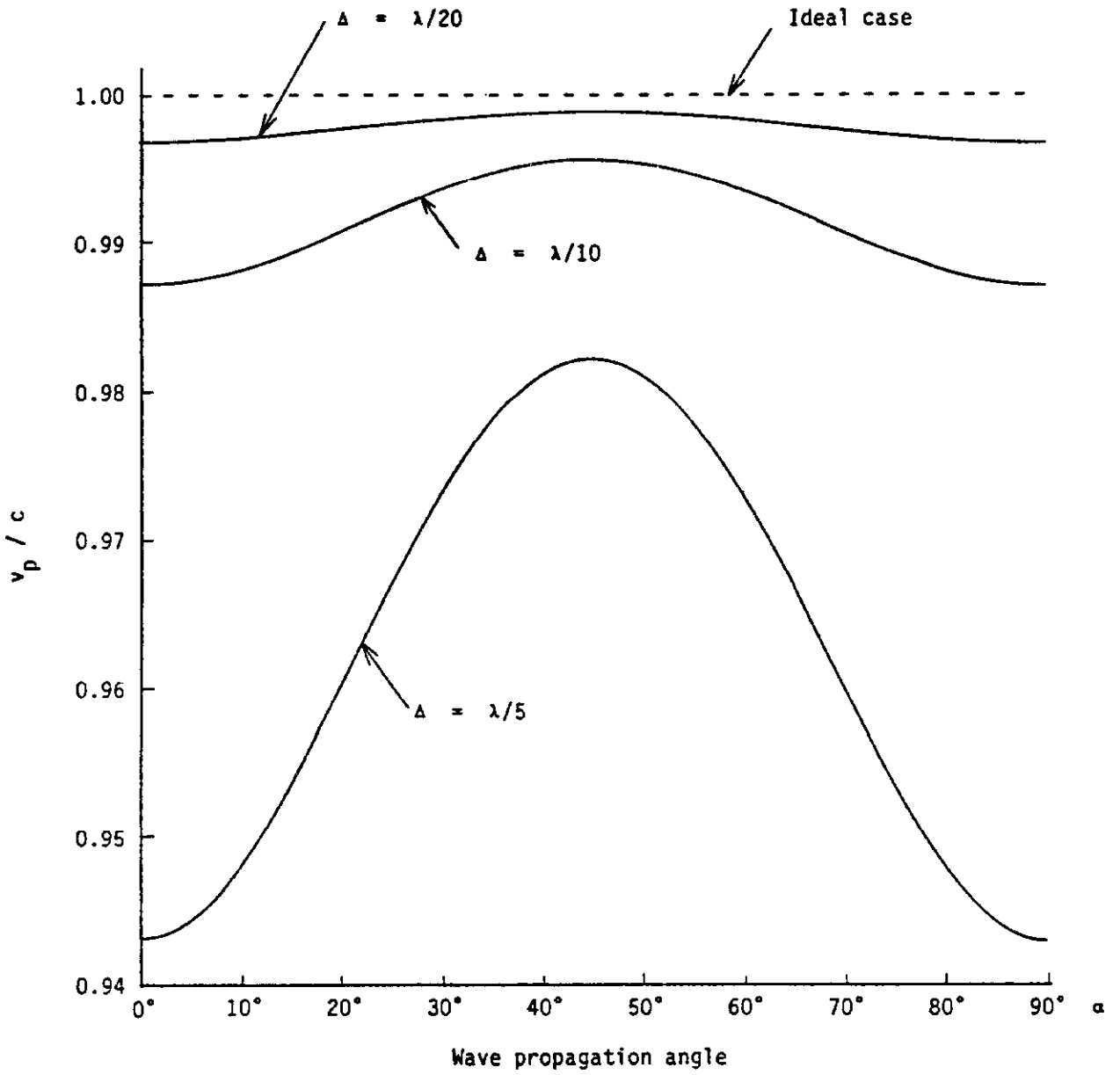


figure 2-4. Variation of phase velocity with wave propagation angle; reproduced from (14) with permission of author

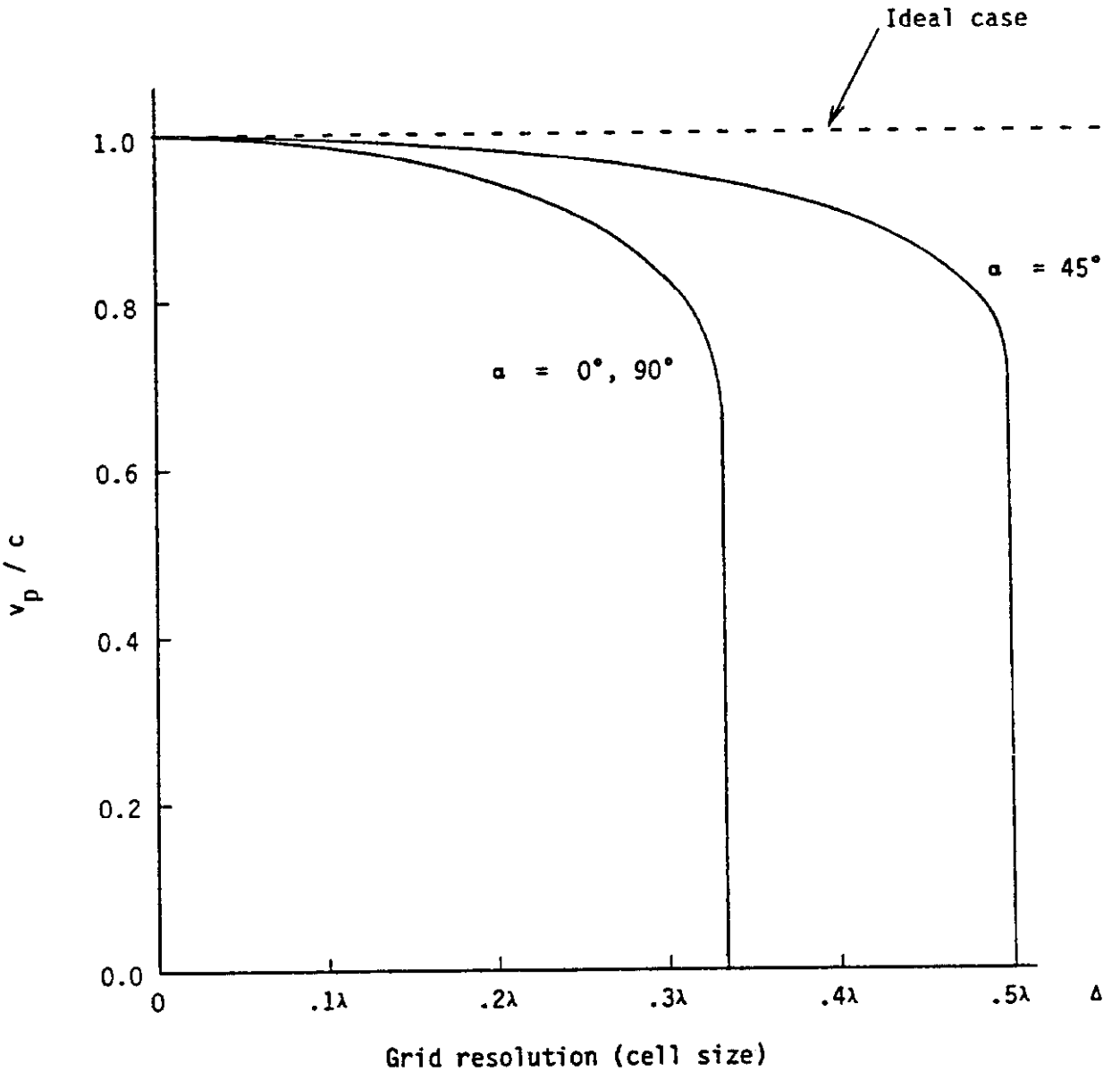


figure 2-5. Variation of phase velocity with grid step size; reproduced from (14) with permission of author

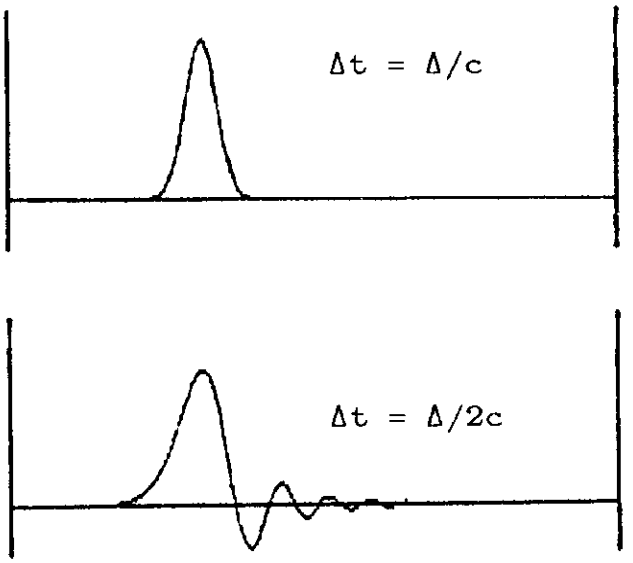


figure 2-6. Effect of time step size on the dispersion of a gaussian pulse, with $\sigma t$ = 796 psec, after 7367 time steps in a one-dimensional FD-TD grid

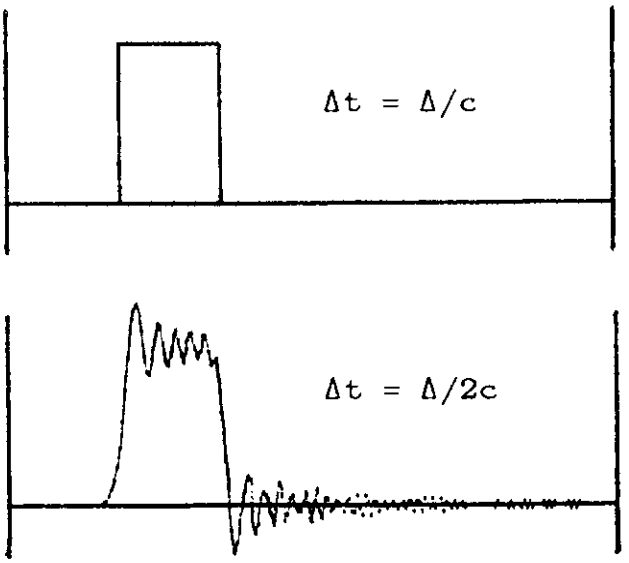


figure 2-7. Effect of time step size on the dispersion of a square 5 nsec wide pulse after 393 time steps in a one-dimensional FD-TD grid

## 2.6 Obtaining magnitude and phase

Because the FD-TD algorithm calculates the scaler field quantities, a special algorithm is required to obtain the magnitude and phase at each time step (10). Shannon's sampling theorem states that that at least two separate time samples are required within one period to uniquely specify a sine wave. This of course assumes that a pure sine wave is being measured. The presence of DC or more than one frequency will complicate the requirements.

The algorithm in the code used requires the storage of five floating point numbers for each field quantity; Hx, Hy or Ez for the TM case. The cost in terms of computer storage is quite high, increasing the field storage requirements by a factor of five. The qualities of each field component that are stored are the field amplitude, the change or difference from the last time step, the minimum and maximum value of the field quantity, and the phase.

The algorithm works by monitoring the time derivative or the stored difference number. If the difference changes from negative to positive and the field component is negative, the minimum number is replaced with the current field amplitude. If the difference changes from positive to negative and the field is positive, a maximum is assumed and both the maximum and phase are updated. The phase is calculated by multiplying the current time step by the number of degrees per time step at the excitation frequency. The

phase is also corrected by interpolating between the old and new difference values to estimate the fractional time step when the difference passed through zero. This algorithm does not work when the DC offset is larger than the sine wave's amplitude.

# III. THE METHOD OF MOMENTS ALGORITHM

## 3.1 The transverse magnetic case

The method of moments, hereafter referred to as MOM, is a technique for solving integral equations using a computer. For an arbitrary shaped, two-dimensional, perfectly conducting scatterer, the electric field can be obtained with the application of the Helmholtz wave equation to the scattered field and equating the sum of the incident and scattered field to zero at the surface of the conductor. The wave equation is given below.

$$\nabla^2 Ez_{scat} + k_o^2 Ez_{scat} = j\omega_o\mu_o Jz \qquad (3.1)$$

$k_o$ is the wave number, or $2\pi/\lambda$, and Jz is the z directed surface current induced by the total transverse magnetic field at the surface. Figure (3-1) shows the cross section for the two-dimensional problem assumed.

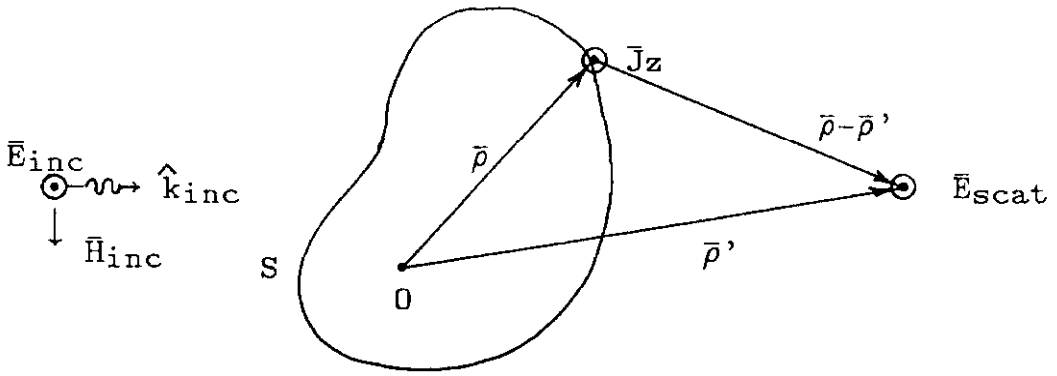


figure 3-1. Cross section of an arbitrary two-dimensional scatterer for the TM case.

The solution to the Helmholtz equation is given in equation (3.2) below (3). The zeroth order Hankel function of the second kind is denoted by $H_o^{(2)}$, $\bar{\rho}$ is a vector which denotes the source location, or position of Jz, and $\bar{\rho}'$ indicates the field location, or position of $Ez_{scat}$. As Jz exists only on the surface of the conductor the integral is confined to the boundary of the scatterer S. At the surface of a perfect conductor the total electric field must be zero.

$$Ez_{scat}(\bar{\rho}') = -\frac{\omega_o\mu_o}{4}\int_{\partial S} Jz(\bar{\rho})H_o^{(2)}(k_o|\bar{\rho}-\bar{\rho}'|)dl \tag{3.2}$$

$$Ez_{scat} + Ez_{inc} = 0 \qquad \text{(on the surface of S)} \tag{3.3}$$

Combining equation (3.3) with (3.2), the integral equation which must be solved through the method of moments, or MOM, technique is obtained.

$$Ez_{inc}(\bar{\rho}') = \frac{\omega_o\mu_o}{4}\int_{\partial S} Jz(\bar{\rho})H_o^{(2)}(k_o|\bar{\rho}-\bar{\rho}'|)dl \tag{3.4}$$

($\bar{\rho}$ and $\bar{\rho}'$ are both on the surface of S)

Let $fn(\bar{\rho})$ be the set of basis functions used to discretize the surface current. Choosing the pulse function, fn may be defined as shown below.

$$fn(\bar{\rho}) = \begin{cases} 1 & \bar{\rho}_n-\Delta/2 < \bar{\rho} < \bar{\rho}_n+\Delta/2 \\ 0 & \text{otherwise} \end{cases} \tag{3.5}$$

The symbol $\Delta$ is used for the separation of samples along the surface of S. Using $f_n$, the surface current may be expressed as a sum over N points.

$$Jz(\bar{\rho}) = \sum_{n=1}^{N} \alpha_n \, fn(\bar{\rho}) \tag{3.6}$$

Thus $\alpha_n$ represents the surface current along the interval $\Delta$. Equivalently, the scatterer is replaced by N current filaments equally spaced by $\Delta$ around the surface of S.

Now define a set of weighting functions $w_m$, inner product $\langle w_m, f \rangle$, and linear operator L. Choosing the set of delta functions as $w_m$;

$$w_m = \delta(\bar{\rho}' - \bar{\rho}_m) = \begin{cases} 1 & \text{for } \bar{\rho}' = \bar{\rho}_m \\ 0 & \text{otherwise} \end{cases} \tag{3.7}$$

$$Lf(\bar{\rho}) = \frac{\omega_o \mu_o}{4} \int_{\partial S} f(\bar{\rho}) H_o^{(2)}(k_o |\bar{\rho} - \bar{\rho}'|) dl \tag{3.8}$$

$$\langle w_m, f(\bar{\rho}') \rangle = \int_{\partial S} f(\bar{\rho}') w_m \, dl' = f(\bar{\rho}_m) \tag{3.9}$$

Let $\rho$, l and n indicate source location, $\rho'$, l' and m indicate field location. Equation (3.4) may be rewritten using equations (3.7), (3.8) and (3.9) as shown below.

$$\langle w_m, Ez_{inc}(\bar{\rho}') \rangle = \langle w_m, LJz(\bar{\rho}) \rangle \tag{3.10}$$

Expanding the left hand side;

$$\langle w_m, Ez_{inc}(\bar{\rho}') \rangle = \int_{\partial S} \delta(\bar{\rho}'-\bar{\rho}_m) Ez_{inc}(\bar{\rho}')dl' = Ez_{inc}(\bar{\rho}_m) \tag{3.11}$$

Expanding the right hand side of equation (3.10);

$$\begin{aligned}
\langle w_m, LJz(\bar{\rho}) \rangle &= \int_{\partial S} \delta(\bar{\rho}'-\bar{\rho}_m) \frac{\omega_o\mu_o}{4} \int_{\partial S} Jz(\bar{\rho}) H_o^{(2)}(k_o|\bar{\rho}-\bar{\rho}'|)dldl' \\
&= \frac{\omega_o\mu_o}{4} \int_{\partial S} \left( \sum_{n=1}^{N} \alpha_n f_n(\bar{\rho}) \right) H_o^{(2)}(k_o|\bar{\rho}-\bar{\rho}_m|)dl \\
&= \sum_{n=1}^{N} \alpha_n \left( \frac{\omega_o\mu_o}{4} \int_{\partial S} f_n(\bar{\rho}) H_o^{(2)}(k_o|\bar{\rho}-\bar{\rho}_m|)dl \right) \\
&= \sum_{n=1}^{N} \alpha_n \left( \frac{\omega_o\mu_o}{4} \int_{\bar{\rho}_n-\Delta/2}^{\bar{\rho}_n+\Delta/2} H_o^{(2)}(k_o|\bar{\rho}-\bar{\rho}_m|)dl \right) \\
&= \sum_{n=1}^{N} \alpha_n \langle w_m, Lf_n(\bar{\rho}) \rangle = \sum_{n=1}^{N} \alpha_n \, l_{mn}
\end{aligned} \tag{3.12}$$

Letting $Jz(\bar{\rho}_n) = \alpha_n$, and using equation (3.11), equation (3.10) can be rewritten in matrix form.

$$\begin{aligned}
Ez_{inc}(\bar{\rho}_m) &= l_{mn} \, Jz(\bar{\rho}_n) \\
Jz(\bar{\rho}_n) &= [l_{mn}]^{-1} \, Ez_{inc}(\bar{\rho}_m)
\end{aligned} \tag{3.13}$$

Thus the discretized surface currents can be found by first calculating the matrix lmn, then inverting it and multiplying by the discretized incident field along the boundary of S. An approximation for lmn is given below (3).

$$d_{mn} = |\bar{\rho}_n - \bar{\rho}_m| = \sqrt{(x_n - x_m)^2 + (y_n - y_m)^2}$$

$$m \neq n \qquad l_{mn} = \frac{k_o \eta_o}{4} \Delta \, H_o^{(2)}(k_o d_{mn}) \tag{3.14}$$

$$m = n \qquad l_{nn} = \frac{k_o \eta_o}{4} \Delta \left(1 - j \frac{2}{\pi} \ln\left(\frac{\gamma k_o \Delta}{4e}\right)\right) \tag{3.15}$$

$$\eta_o = \sqrt{\frac{\mu_o}{\epsilon_o}} \qquad k_o = \frac{2\pi}{\lambda} = \frac{\omega_o}{v} = \omega_o \sqrt{\mu_o \epsilon_o}$$

$$\gamma = 1.781 \quad \text{(eulers constant)}$$

When $m = n$, $d_{mn} = 0$, and $H_o^{(2)}(0) \rightarrow \infty$. In order to overcome this singularity problem the small argument approximation is used for the Hankel function shown below.

$$H_o^{(2)}(z) \simeq 1 - j \frac{2}{\pi} \log\left(\frac{\gamma z}{2}\right) \qquad \text{(for z small)} \tag{3.16}$$

## 3.2 The transverse electric case

An approach for solving the TE case involves the solution to the Helmholtz wave equation applied to the magnetic vector potential $\bar{A}$. Using the solution to the wave equation, $Hz_{scat}$ can be expressed in terms of the surface current as shown below.

$$\nabla^2 \bar{A} + k_o^2 \bar{A} = - \mu_o \bar{J}$$

$$\bar{A}(\bar{\rho}') = \frac{\mu_o}{4j} \int_{\partial S} \bar{J}(\bar{\rho}) H_o^{(2)}(k_o|\bar{\rho}-\bar{\rho}'|)dl$$

$$\bar{H} = \frac{1}{\mu_o} \nabla \times \bar{A}$$

$$\bar{H}_{scat}(\bar{\rho}') = \frac{1}{4j} \nabla \times \int_{\partial S} \bar{J}(\bar{\rho}) H_o^{(2)}(k_o|\bar{\rho}-\bar{\rho}'|)dl \qquad (3.17)$$

Figure (3-2) shows the cross section of an arbitrary two-dimensional perfectly conducting scatterer. As indicated, $\hat{n}$ is the unit normal vector and $\hat{\tau}$ is the unit tangential vector to the surface, so that $\hat{\tau} = \hat{z} \times \hat{n}$. Using the direction of surface current shown, $J\tau$ can be expressed in terms of $Hz_{inc}$ and $Hz_{scat}$.

$$\bar{J} = \hat{n} \times \bar{H}_{tot}$$

$$J\tau = -(Hz_{inc} + Hz_{scat}) \qquad (3.18)$$

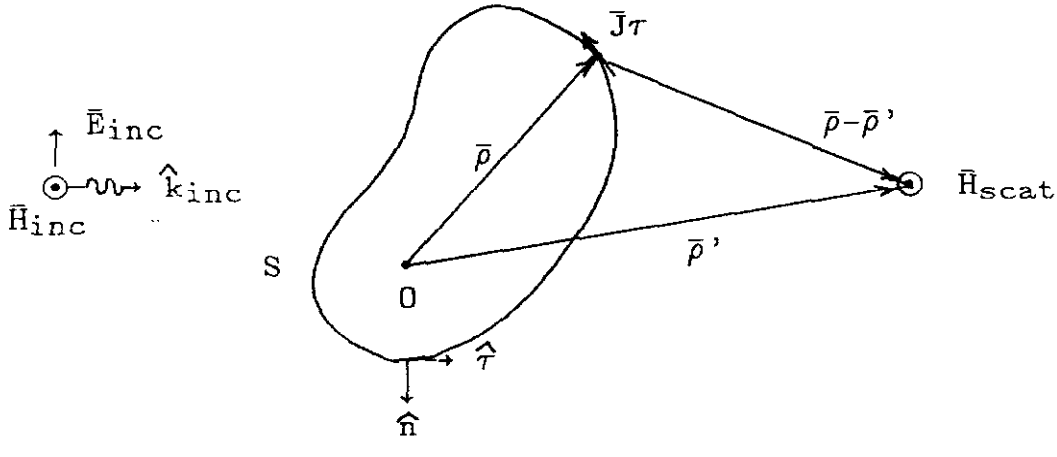


figure 3-2. Cross section of an arbitrary two-dimensional scatterer for the TE case.

Combining equations (3.17) and (3.18) and rearranging equation (3.19) is obtained.

$$-Hz_{inc}(\bar{\rho}') = J\tau(\bar{\rho}) + \frac{1}{4j} \nabla \times \int_{\partial S} \hat{\tau} J\tau(\bar{\rho}) H_o^{(2)}(k_o|\bar{\rho}-\bar{\rho}'|)dl \qquad (3.19)$$

($\bar{\rho}$ and $\bar{\rho}'$ are both on the surface of S)

The integral is then broken into two parts, $\partial S - S_o$ and $S_o$. The singular region of S, denoted by $S_o$, is that location where $J\tau$ and $Hz_{inc}$ coincide. The value of the latter integral is approximately $-J\tau/2$ (3).

$$-Hz_{inc}(\bar{\rho}') = J\tau(\bar{\rho}) + \frac{1}{4j} \nabla \times \int_{\partial S - S_o} \hat{\tau} J\tau(\bar{\rho}) H_o^{(2)}(k_o|\bar{\rho}-\bar{\rho}'|)dl$$

$$+ \frac{1}{4j} \nabla \times \int_{S_o} \hat{\tau} J\tau(\bar{\rho}) H_o^{(2)}(k_o|\bar{\rho}-\bar{\rho}'|)dl$$

$$\simeq -J\tau(\bar{\rho})/2$$

$$-Hz_{inc}(\bar{\rho}') = \frac{1}{2} J\tau(\bar{\rho}) + \frac{1}{4j} \int_{\partial S - S_o} J\tau(\bar{\rho}) \frac{\partial}{\partial \hat{n}} H_o^{(2)}(k_o|\bar{\rho}-\bar{\rho}'|)dl \qquad (3.20)$$

Using the pulse functions for $f_n$ and the delta functions for $w_m$, as in the TM case, an approximation for $l_{mn}$ can be found as shown (3);

$$L = \frac{1}{2} + \frac{1}{4j} \int_{\partial S - S_o} \frac{\partial}{\partial \hat{n}} H_o^{(2)}(k_o|\bar{\rho}-\bar{\rho}'|)dl$$

$$l_{mn} = \langle w_m, L f_n(\bar{\rho}) \rangle = \frac{1}{2} + \frac{1}{4j} \int_{\bar{\rho}_n - \Delta/2}^{\bar{\rho}_n + \Delta/2} \frac{\partial}{\partial \hat{n}} H_o^{(2)}(k_o|\bar{\rho}-\bar{\rho}_m|)dl$$

$$m=n \quad l_{nn} = \frac{1}{2} \qquad (3.21)$$

$$m \neq n \quad l_{mn} = \frac{j}{4} k_o \Delta H_1^{(2)}(k_o d_{mn}) \hat{n} \cdot \hat{R} \qquad (3.22)$$

$\hat{R} = \frac{(x_m - x_n, y_m - y_n)}{|\bar{\rho}_m - \bar{\rho}_n|}$ unit vector pointing from $J\tau(\bar{\rho}_n)$ to $Hz_{inc}(\bar{\rho}_m)$

$\hat{n}$ = unit normal at the location of $J\tau(\bar{\rho}_n)$

$$J\tau(\bar{\rho}_n) = [l_{mn}]^{-1}(-Hz_{inc}(\bar{\rho}_m)) \tag{3.23}$$

# IV. COMPARISON OF METHOD OF MOMENTS AND FINITE-DIFFERENCE TIME-DOMAIN ALGORITHMS

## 4.1 Discussion of method of moments

MOM provides a solution for only a single frequency. Analysis of a structure with an incident field that has arbitrary time dependence would require decomposing the time domain function into a sum of single frequency sinusoidal parts and applying MOM to each separately. The result for each frequency requires storage at least for a few spatial points of interest. Once the frequency domain data has been taken, a Fourier transform could be applied to convert it to the time domain response. Alternatively, if all frequencies are modeled and results saved one could convolve the data with an arbitrary time domain function and obtain the desired response.

MOM requires the evaluation of the incident field along a possibly complex structure. The algorithm becomes complicated if several types of media with arbitrary shape are being modeled. Special treatment is required for the singularity point, and corners on the scatterer must be treated with care. If the structure is excited at resonance it has been shown that the solution is not unique (16).

For N points around the surface, MOM requires the inversion of and storage for, an N X N array. In addition, if analysis in the time domain is performed, storage for each frequency run is required.

For fields not on the surface, a separate integral equation over the surface must be formulated and solved.

## 4.2 Discussion of finite-difference time-domain

The incident fields may have any time dependence desired, however like MOM, analysis in the time domain requires additional storage. For N points around the surface, FD-TD requires approximately $((N+20)/4)^2$ storage when the lattice truncation planes are located 10 cells from the scatterer.

The incident fields are only required on the surface of a simple total/scattered field boundary. In addition the time dependence need only be evaluated at one point on the one-dimensional incident field grid.

If an impulse incident field is used, information about all frequencies can be obtained with only a single run. If a single frequency is applied, FD-TD requires a special algorithm to obtain the magnitude and phase information. This algorithm has a strong effect on the convergence of the final result.

# V. SELECTION OF MODELING PARAMETERS

## 5.1 The geometry and variables used

Two geometries were modeled. The simplicity of a solid square cylinder offered a good starting point for the study. A slotted hollow square cylinder with the same outside dimension, was used as a simple cavity resonator. Both were assumed infinitely long in the z direction. A cross section of the slotted cavity in the FD-TD grid is shown in figure (5-1). The overall lattice size was 46 cells in the x direction and 48 cells in the y direction. This placed the 20 cell by 20 cell cylinder a minimum of 11 cells from the lattice truncation boundary. The total/scattered field interface was 4 cells inside the lattice on all sides.

The permittivity and permeability were set to free space values and the magnetic resistivity was assumed to be zero throughout the grid. The scatterer is defined in the code by setting the electrical conductivity of the cells occupied by the scatterer to that of copper, $3.72 \times 10^7$ mhos/meter. All other cells were defined as having zero conductivity. The code could be easily modified from that for the slotted hollow cylinder to the "solid" cylinder by specifying the conductivity of the cells within the slot. Thus the solid cylinder was really hollow. Several runs of the code were made with the solid cylinder to determine when a significant amount of field would leak into the center. A frequency of 209.297 MHz and cell size of .0397888 meters were used. The frequency was selected so that one half wavelength was equivalent to the inside

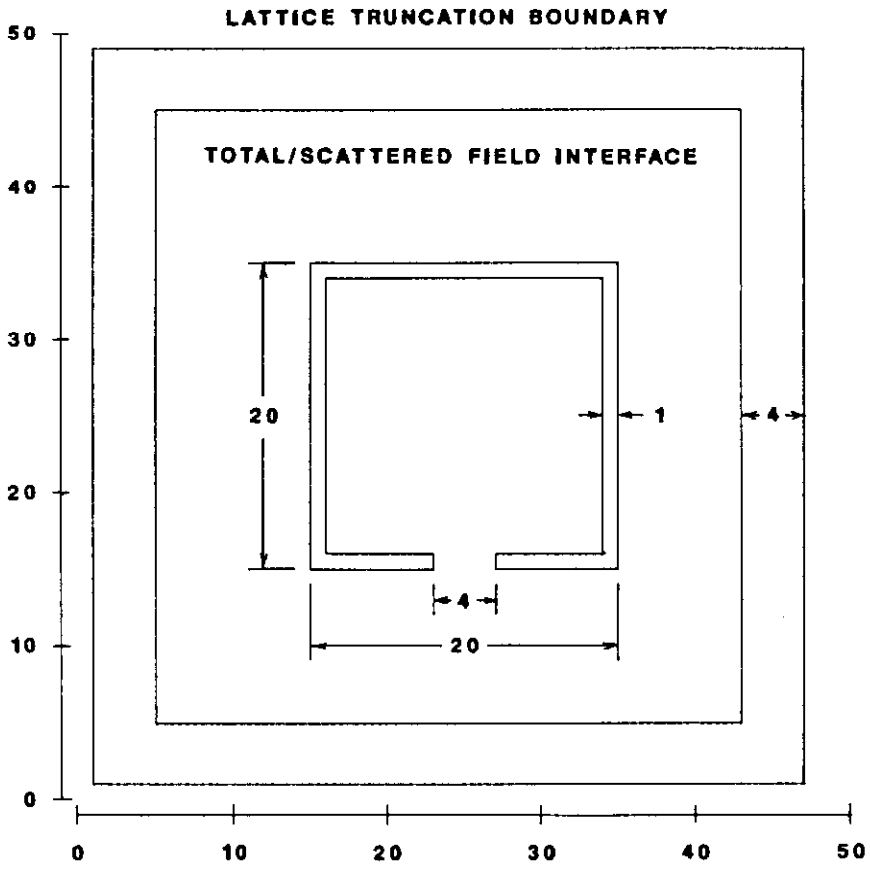


figure 5-1. The FD-TD grid with cross section of the slotted cavity

dimension of the cylinder. This was done to amplify the effect of fields leaking inside. With $\sigma$ = 154 mhos/meter, about .1 to 1 part per thousand of the total field at the outside front surface leaked inside. The skin depth and attenuation through the one cell thick wall is estimated below.

$$f = \frac{1}{2}\frac{c}{18\Delta} = 209.297 \text{ MHz}$$

$$\text{skin depth } \delta = \frac{1}{\sqrt{\sigma \pi f \mu}} = .002803 \text{ meters}$$

$$\text{attenuation through 1 cell} = e^{-\frac{\Delta}{\delta}} = 6.85\text{x}10^{-7}$$

Because the wall is only one cell thick, and the model was being driven near resonance, the FD-TD algorithm indicates more leakage than one might expect. However, since $\delta$ is related to $\sigma$ times f with $\sigma$ = 3.72x10$^7$ mhos/meter, the leakage should be minimal down to frequencies on the order of 209 MHz scaled by (154/3.72x10$^7$), or 870 hertz.

For all of the calculations in this paper the incident fields consisted of a plane wave traveling in the positive y direction. The frequency used for the frequency domain MOM/FD-TD comparisons was arbitrarily chosen as 300 MHz whose sole advantage is providing a wavelength of exactly one meter provided $\mu$ and $\epsilon$ are chosen to yield a velocity of light of exactly 3x10$^8$ meters per second. The cell size was chosen to make the 20 cell length of one side of the scatterer the order of one wavelength. If A is the length of one side in meters then choosing $\Delta$ = .0397888 meters provides a $k_o$A =

5, where $k_o = 2\pi/\lambda$. Thus one side is .7958$\lambda$ long. This seemed far enough away from obvious resonances, for example $A = \lambda/2$. Finally, the time step was chosen to be $\Delta/2c$, or 66.315 psec, which is safely below the numerical stability limit of $\Delta/c\sqrt{2}$. In the model, one wavelength at 300 MHz is about 25 cells, thus there should be small variations in phase velocity with direction at this frequency.

The equivalent surface currents were used to compare the MOM and FD-TD results. The MOM algorithm solves for these directly. For the FD-TD algorithm they are given by the simple relation $\bar{J} = \hat{n} \times \bar{H}_{tot}$, where $\hat{n}$ is the unit normal to the surface and $H_{tot}$ is the magnetic field one half cell from the surface.

# VI. RESULTS OF CALCULATIONS

## 6.1 Square solid cylinder excited with 300 MHz

The FD-TD code was allowed to run for 750 time steps or about 15 cycles. Figures (6-1) and (6-2) compare the resulting surface current magnitude and angle from both the FD-TD and MOM codes, for the TE and TM cases respectively. The vertical lines indicate the position of the corners. For the TE case the difference between the MOM and FD-TD results is less than 1% for both magnitude and angle.

Looking at the TM case in figure (6-2), the MOM points are located in between the FD-TD points. This is because of where the fields are located within the FD-TD unit cell. Secondly, MOM predicts larger currents at the corners of the scatterer. This is because the FD-TD surface currents are calculated with the magnetic field one half cell away from the surface. Finally, on the backside of the scatterer the TM case diverges significantly for the two algorithms. The MOM algorithm indicates the amplitude approaches zero and has a more continuous phase, where the FD-TD result has a larger magnitude and reports a phase of exactly zero. These zero points were excluded from the phase plot. The first attempt at understanding this problem was to increase the incident field magnitude by a factor of 10, in the chance that the magnitude and phase algorithm in the FD-TD code was not detecting zero crossings. The code was also allowed to run for 50 cycles or 2500 time steps; identical results were obtained. Later tests indicate

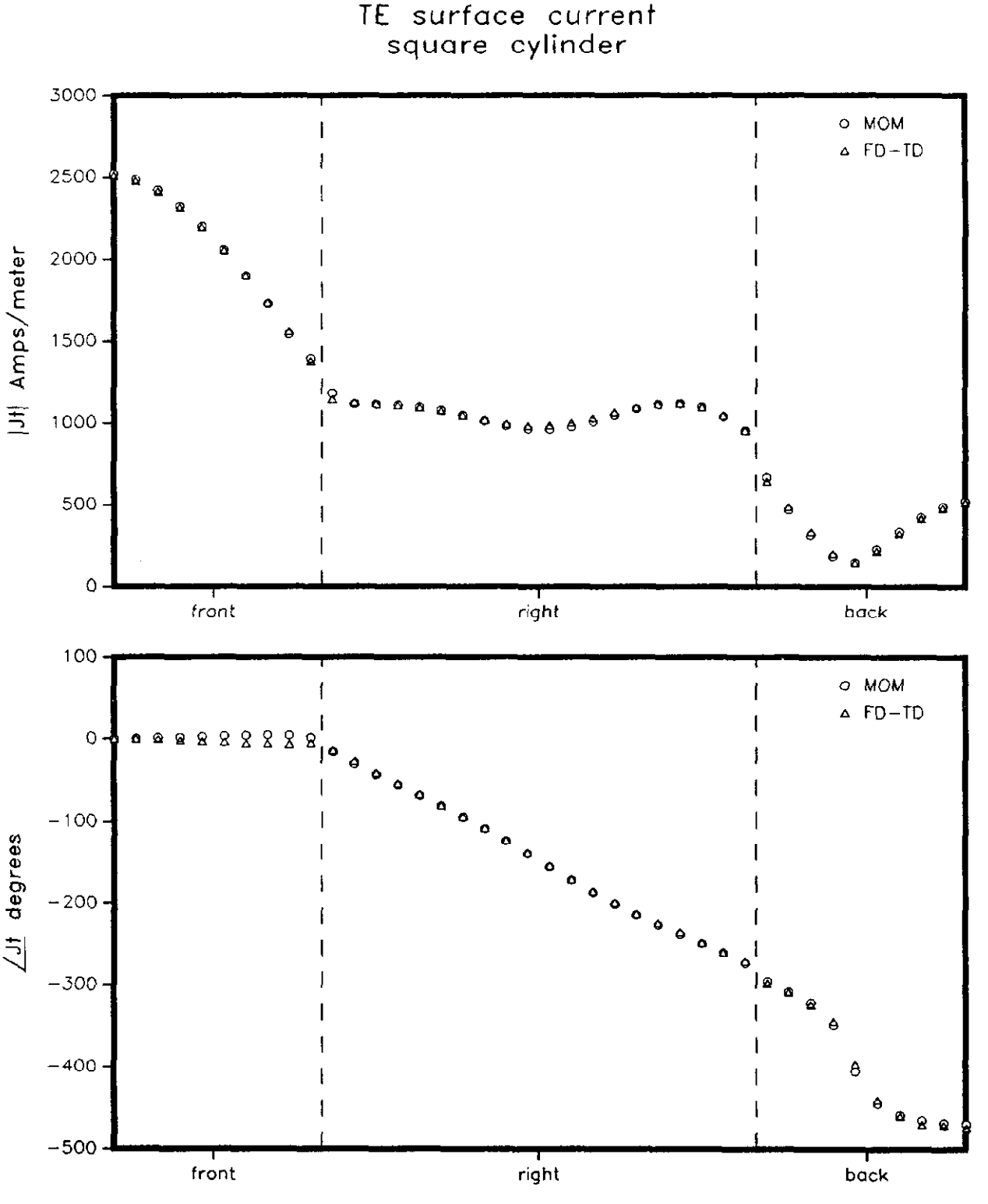


figure 6-1. Comparison of MOM and FD-TD TE mode solutions for the magnitude and phase of the surface current on a square cylinder excited with a 300 MHz incident wave

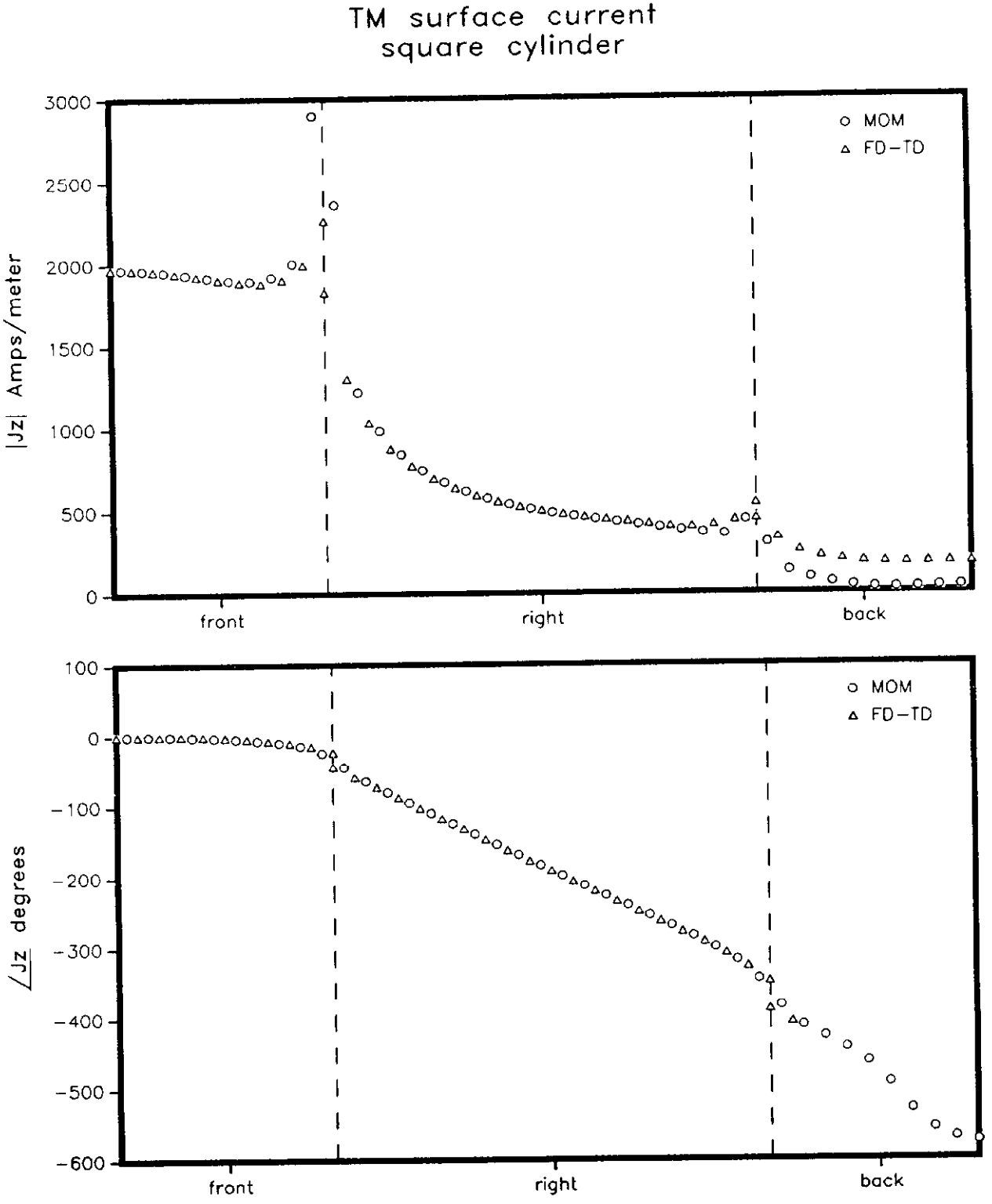


figure 6-2. Comparison of MOM and FD-TD TM mode solutions for the magnitude and phase of the surface current on a square cylinder excited with a 300 MHz incident wave

the magnitude and phase algorithm has difficulty with a DC component present in the backside, or shadow region, of the cylinder. This will be discussed more in the following sections.

## 6.2 Slotted cavity with 300 MHz excitation

Figures (6-3) and (6-4) compare the magnitude and phase of the surface current for the TE and TM cases on the slotted cavity. Both cases show larger differences than with the solid cylinder. Again, the FD-TD TM case has trouble with the backside and the MOM TM case has trouble with corners. The FD-TD numbers were obtained by allowing the code to run for 15 cycles or 750 time steps.

In an effort to understand the difference between the MOM and FD-TD results, the FD-TD code was modified to list the magnitude of a few selected locations for each cycle of the field. The locations chosen were at the center of the inside and outside back surfaces. The code was allowed to run for 50 cycles, or 2500 time steps, see figure (6-5). For both the TE and TM cases, the currents on the outside back surface apparently converged after 15 cycles, or 750 time steps, which was the cycle used for the comparison of figures (6-3) and (6-4). The current on the inside surface for the TE case has roughly a four cycle or 75 MHz oscillation which converges eventually. The TM case, however, has a large low frequency oscillation. These convergence problems are discussed in the next section.

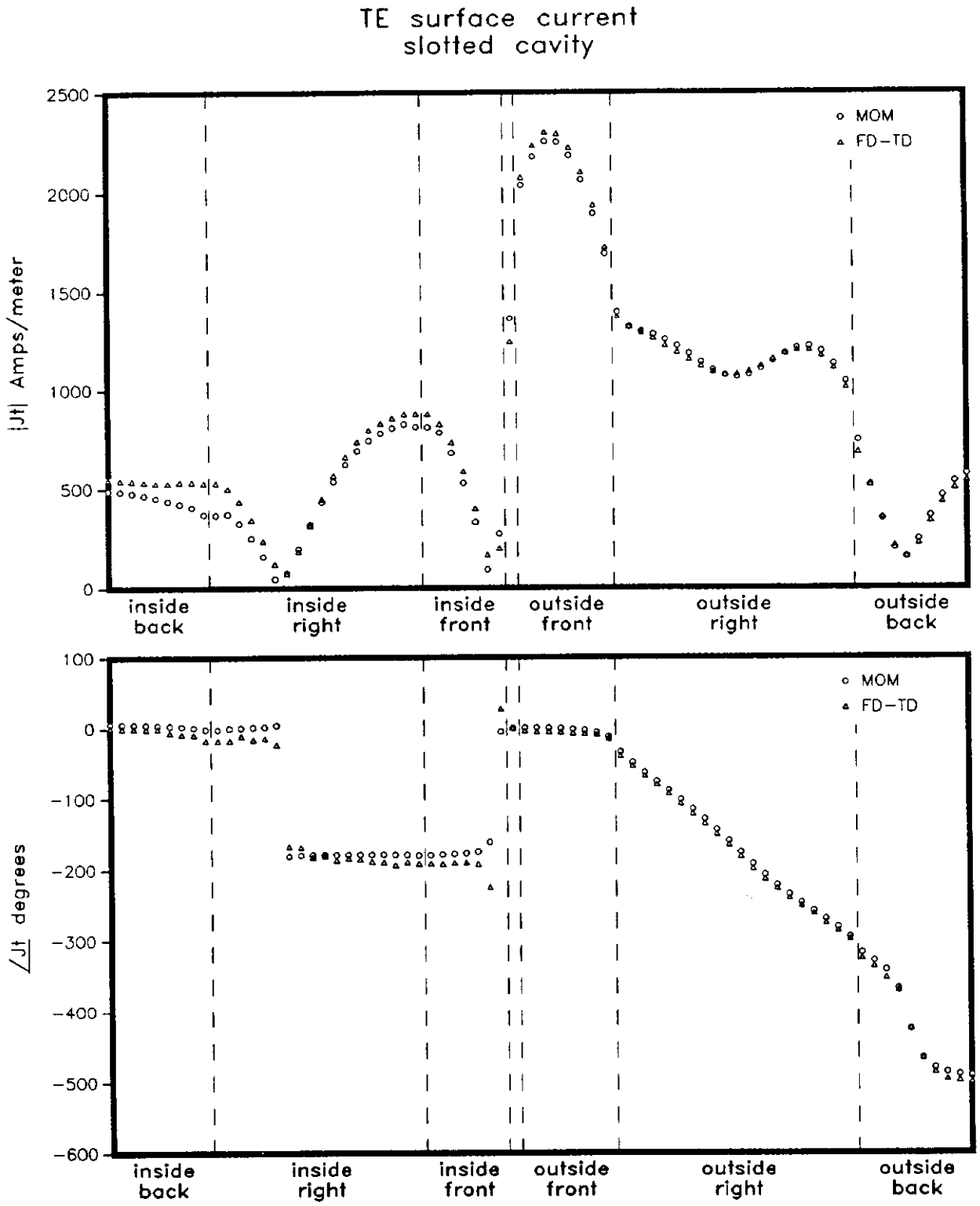


figure 6-3. Comparison of MOM and FD-TD TE mode solutions for the magnitude and phase of the surface current on a slotted cavity excited with a 300 MHz incident wave

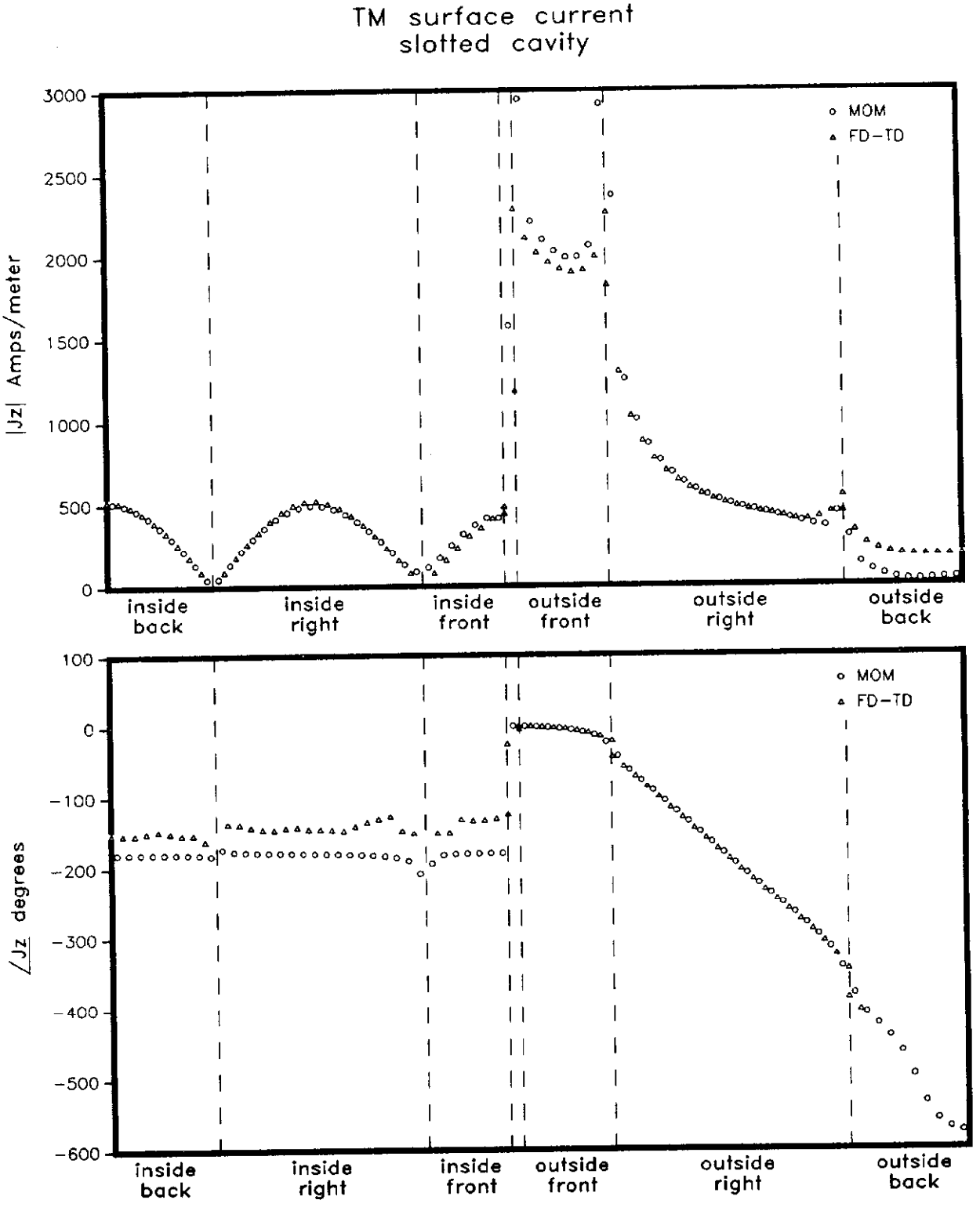


figure 6-4. Comparison of MOM and FD-TD TM mode solutions for the magnitude and phase of the surface current on a slotted cavity excited with a 300 MHz incident wave

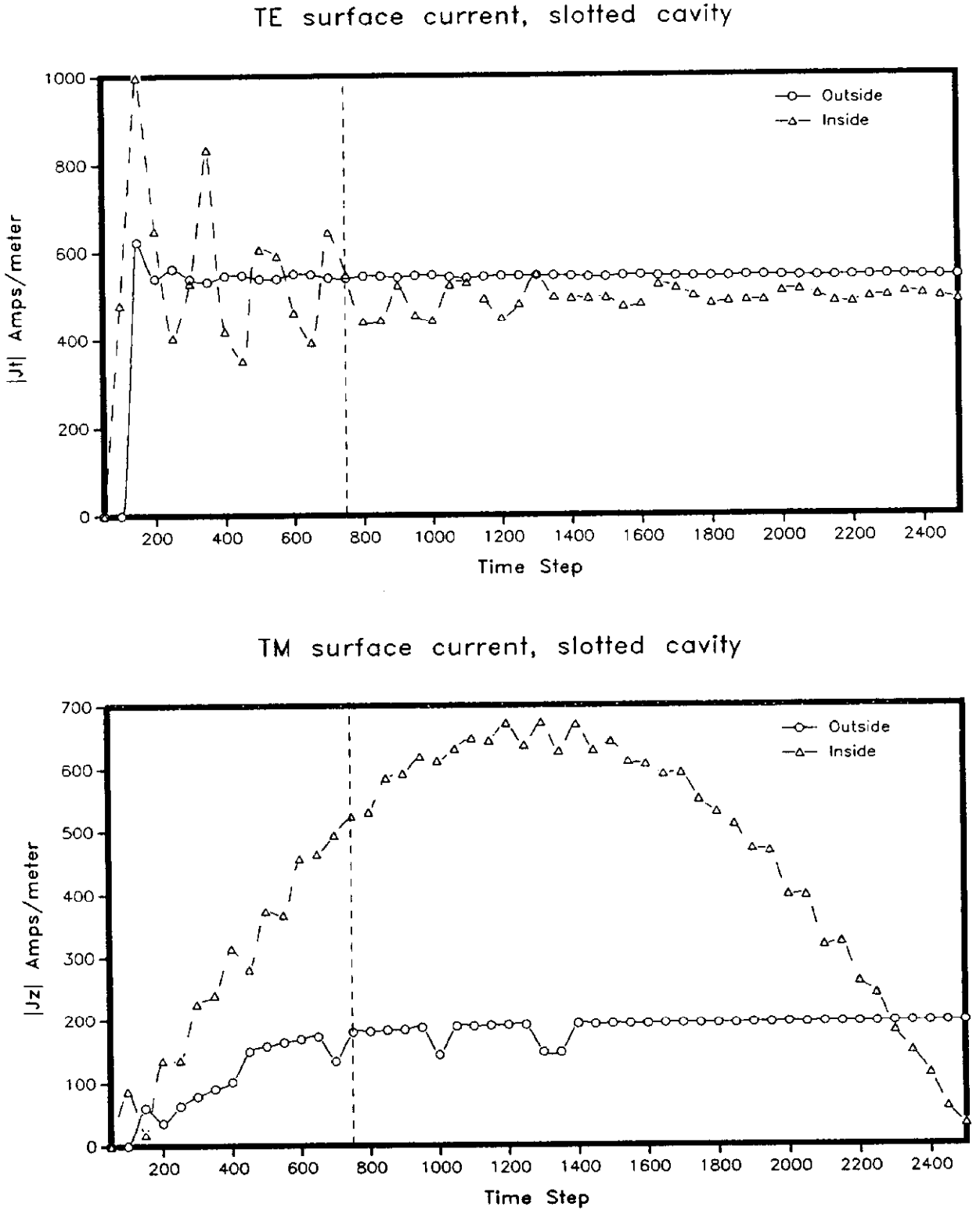


figure 6-5. Convergence of TE and TM solutions to the slotted cavity using the magnitude and phase algorithm, vertical line indicates time step used for MOM/FD-TD comparisons

## 6.3 Slotted cavity excited with 300 MHz in the time domain

The FD-TD code was modified to list scaler field components at each time step. The tangential magnetic field components one half cell from the surface, at the six locations indicated in figure (6-6) below, were stored for each time step for both the TE and TM cases. As both the scatterer and the incident plane wave have symmetry around a line parallel with the y axis and passing through the center of the scatterer, one need only be concerned with one half of the structure.

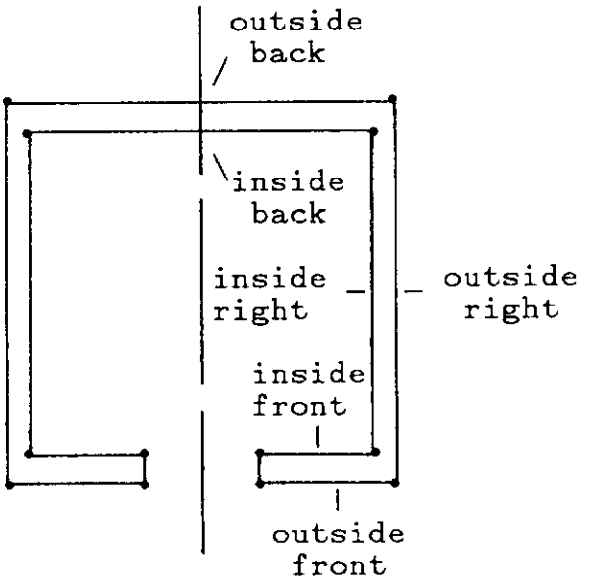


figure 6-6. Locations of the sampled field points.

The relevant parameters to keep in mind for applying a Fourier transform are: 1) the useful bandwidth is less than one over the time sampling rate and 2) the frequency resolution is one over the total sampling period. If $\Delta t$ is the time per sample and N is the total number of samples, then;

$$\text{frequency resolution} = \frac{1}{N\Delta t} = \frac{2c}{N\Delta} \quad \text{for} \quad \Delta t = \frac{\Delta}{2c} \tag{6.1}$$

$$\text{frequency bandwidth} = \frac{1}{2\Delta t} = \frac{c}{\Delta} \tag{6.2}$$

The lowest frequency mode expected with the structure occurs at the frequency when the inside dimension is one half wavelength long, or 209.3 MHz. The largest measurable Q will be the resonant frequency divided by the frequency resolution.

$$\text{resonant frequency} = \frac{c}{2(18\Delta)}$$

$$Q_{max} = \frac{N\Delta}{2c}\,\frac{c}{2(18\Delta)} = \frac{N}{4(18)} \tag{6.4}$$

The FD-TD code was allowed to run for 5000 time steps. This required about 55 minutes of cpu time on a Vax 8650 computer, which was just under the default time limit of one hour. At 300 MHz, the excitation frequency, 5000 time steps corresponds to 100 cycles. This provided a Qmax of only about 69.4 for the 209 MHz mode expected.

Figure (6-7) shows the TE results and figure (6-8) shows the TM results. In order to use a fast Fourier transform algorithm, the 5000 point time record was zero extended to 8192 points. Although the entire time record is plotted, only the DC to one gigahertz frequency domain data is plotted. The most surprising result was the presence of energy at frequencies other than 300 MHz, most noticeable in the Fourier transforms of the inside fields of the cavity.

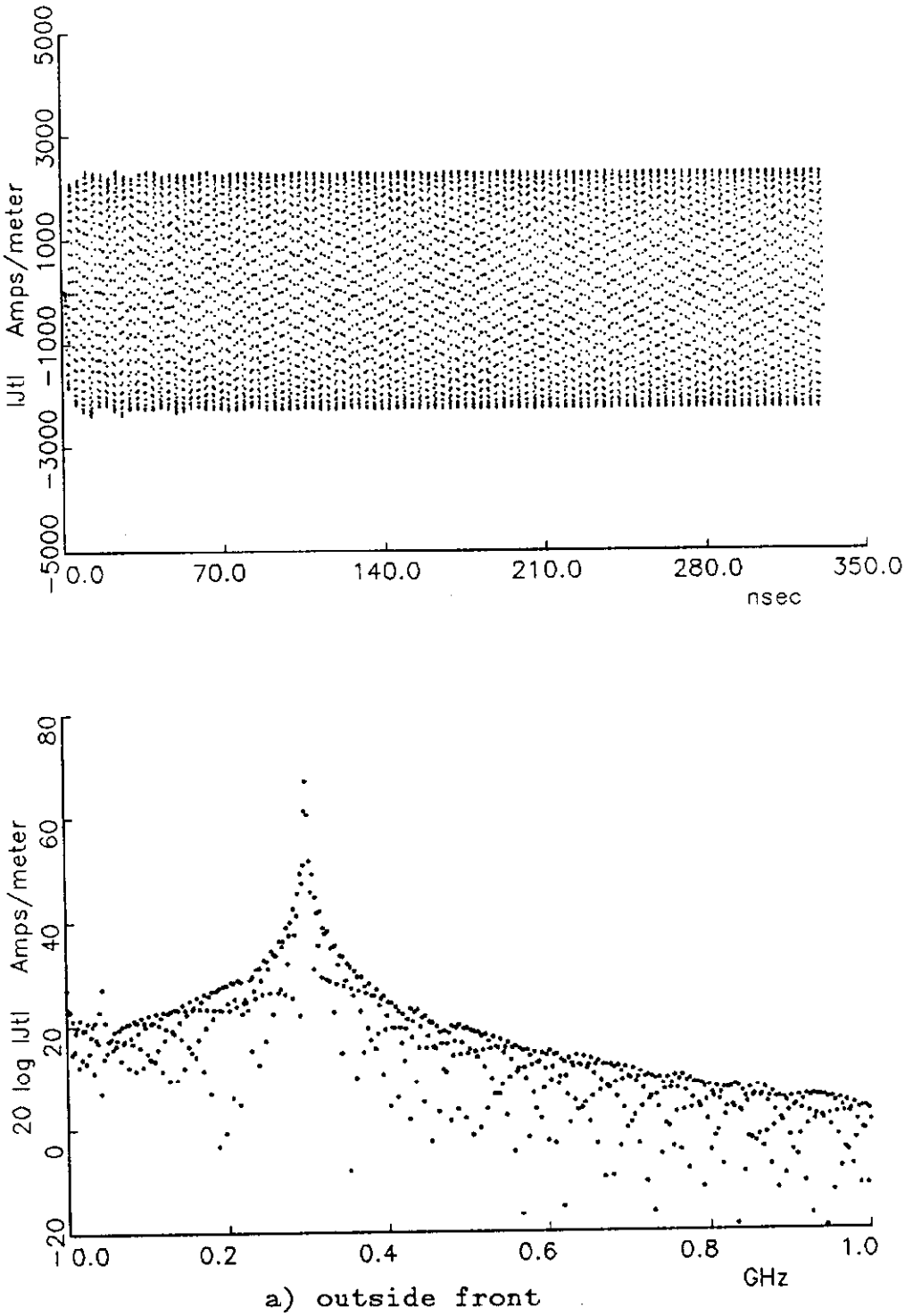


figure 6-7. Time and frequency domain plots of TE mode surface currents at six locations around the surface of a slotted cavity excited with a 300 MHz incident wave; a) outside front, b) outside right, c) outside back, d) inside front, e) inside right, f) inside back

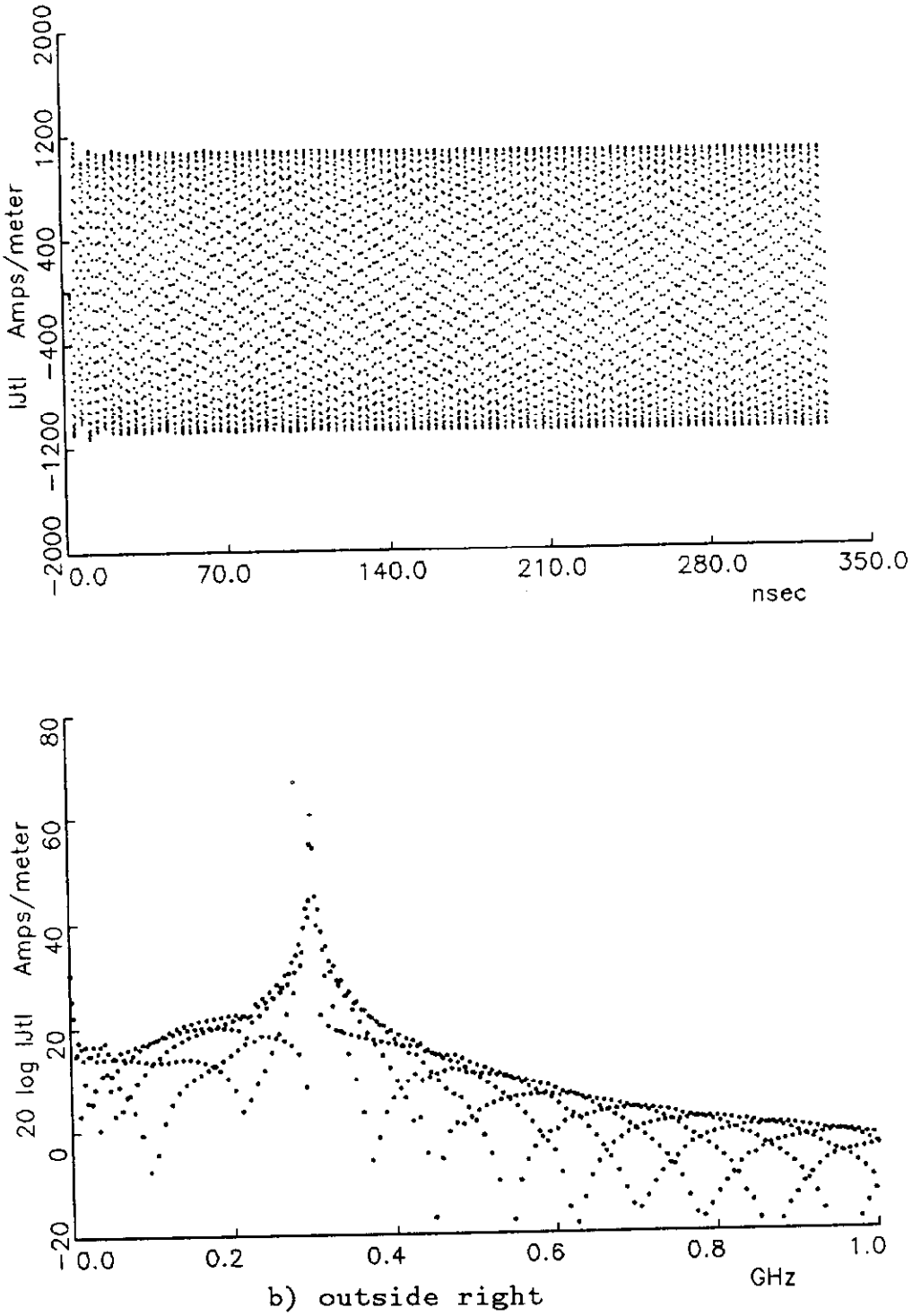


figure 6-7. (continued) Time and frequency domain plots of TE mode surface currents at six locations around the surface of a slotted cavity excited with a 300 MHz incident wave; a) outside front, b) outside right, c) outside back, d) inside front, e) inside right, f) inside back

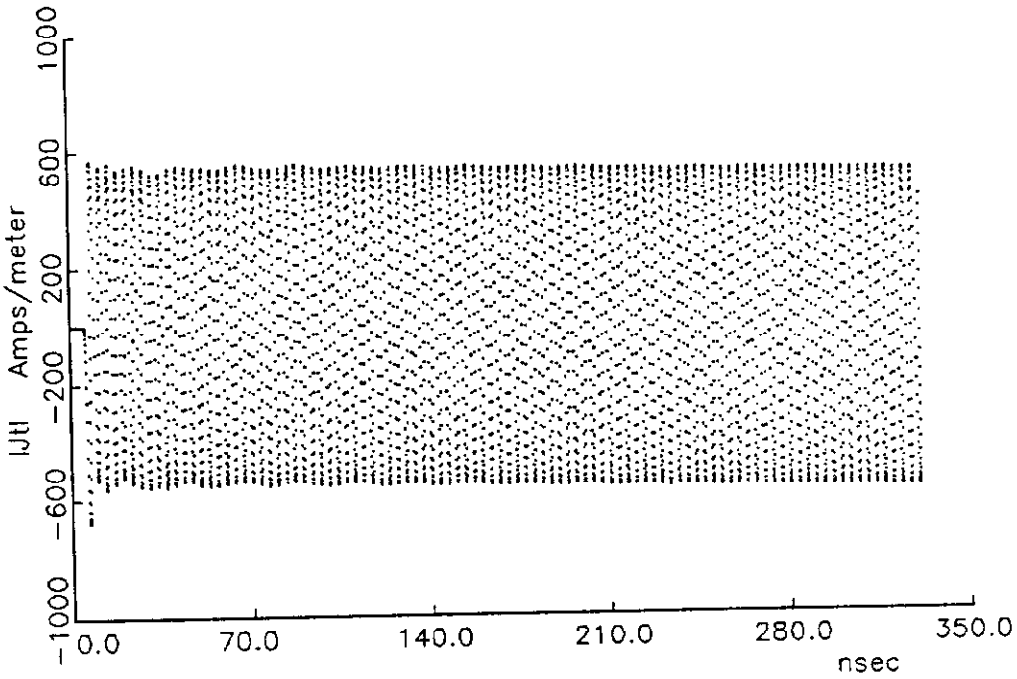


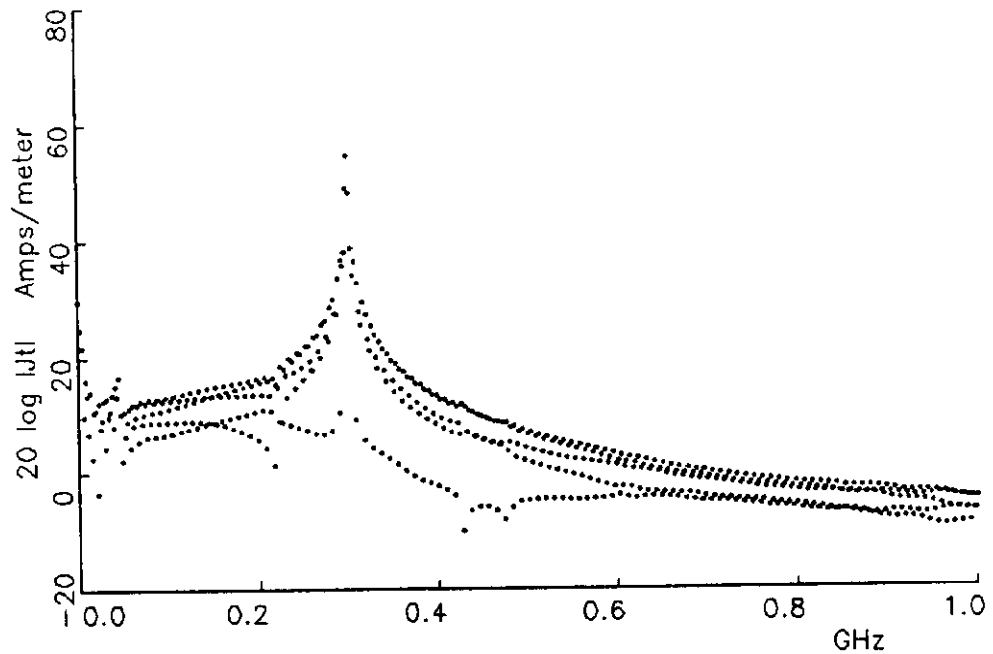


c) outside back

figure 6-7. (continued) Time and frequency domain plots of TE mode surface currents at six locations around the surface of a slotted cavity excited with a 300 MHz incident wave; a) outside front, b) outside right, c) outside back, d) inside front, e) inside right, f) inside back

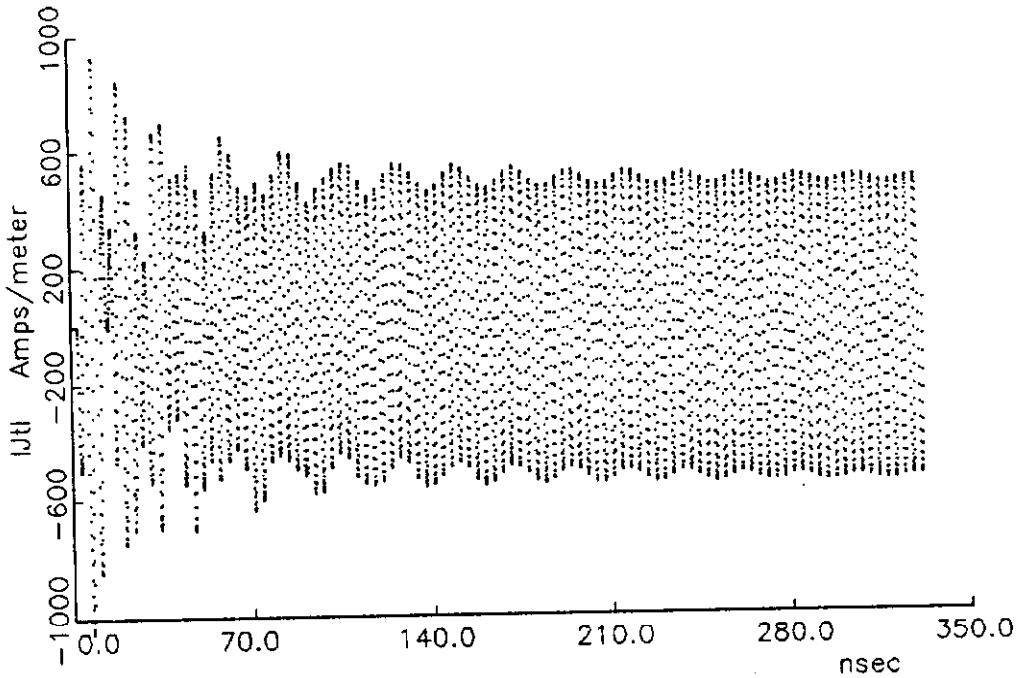


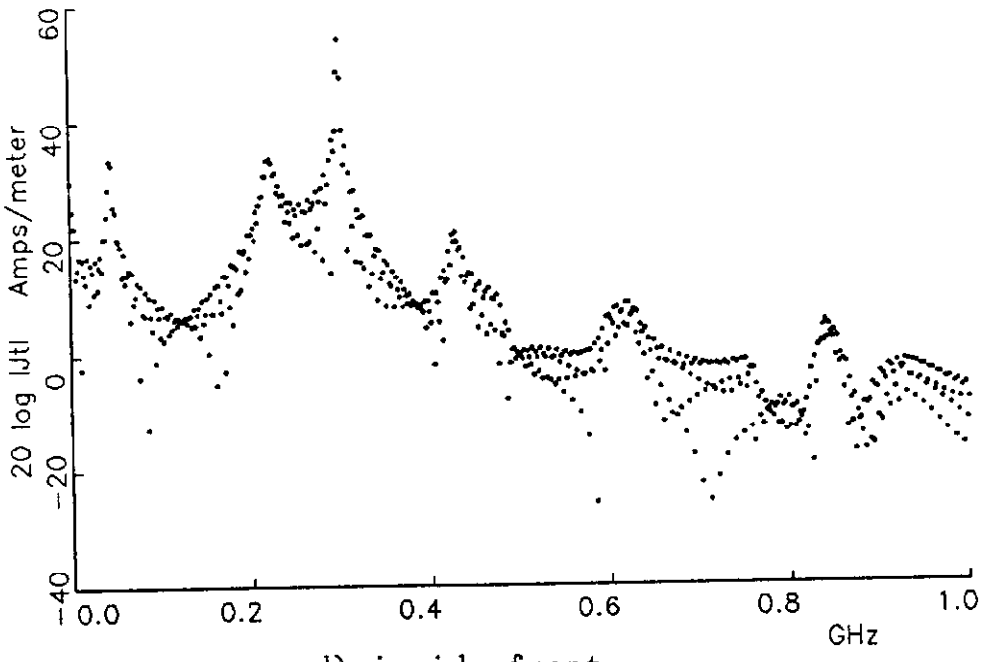


d) inside front

figure 6-7. (continued) Time and frequency domain plots of TE mode surface currents at six locations around the surface of a slotted cavity excited with a 300 MHz incident wave; a) outside front, b) outside right, c) outside back, d) inside front, e) inside right, f) inside back

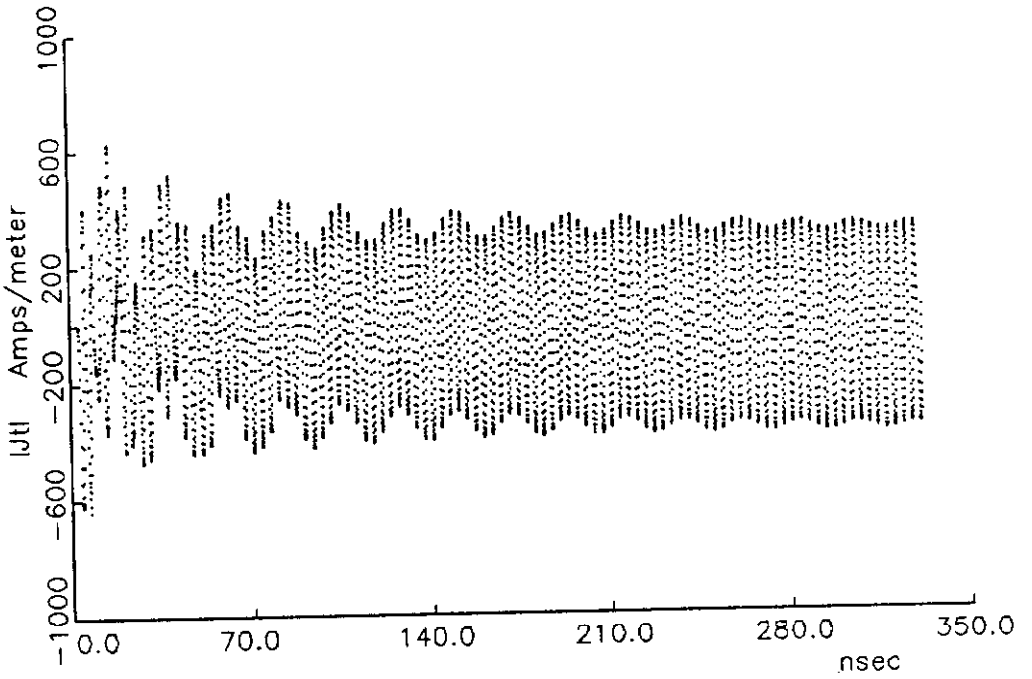


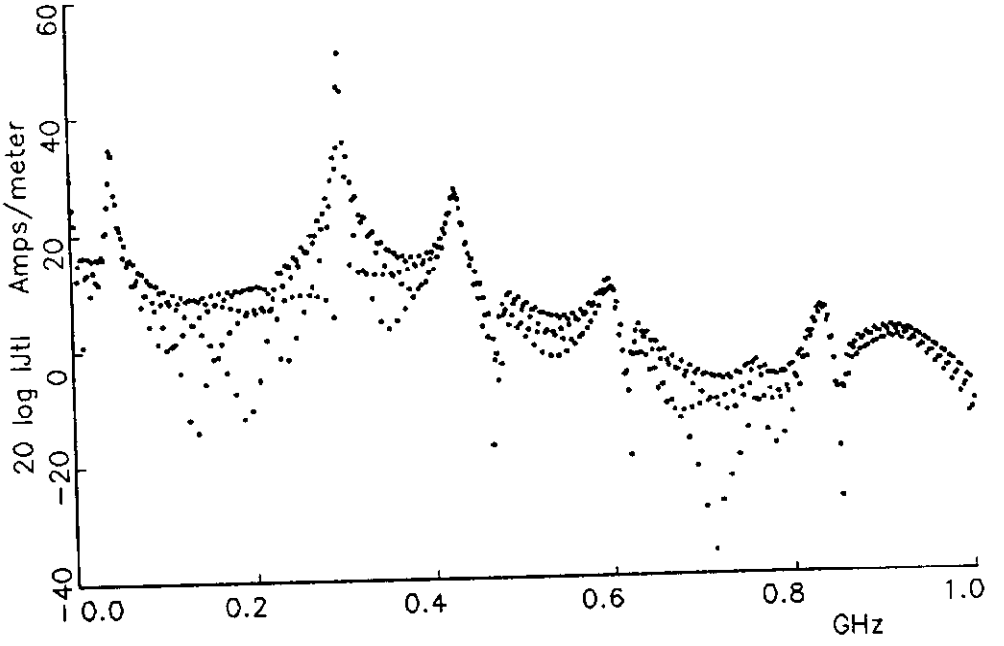


e) inside right

figure 6-7. (continued) Time and frequency domain plots of TE mode surface currents at six locations around the surface of a slotted cavity excited with a 300 MHz incident wave; a) outside front, b) outside right, c) outside back, d) inside front, e) inside right, f) inside back

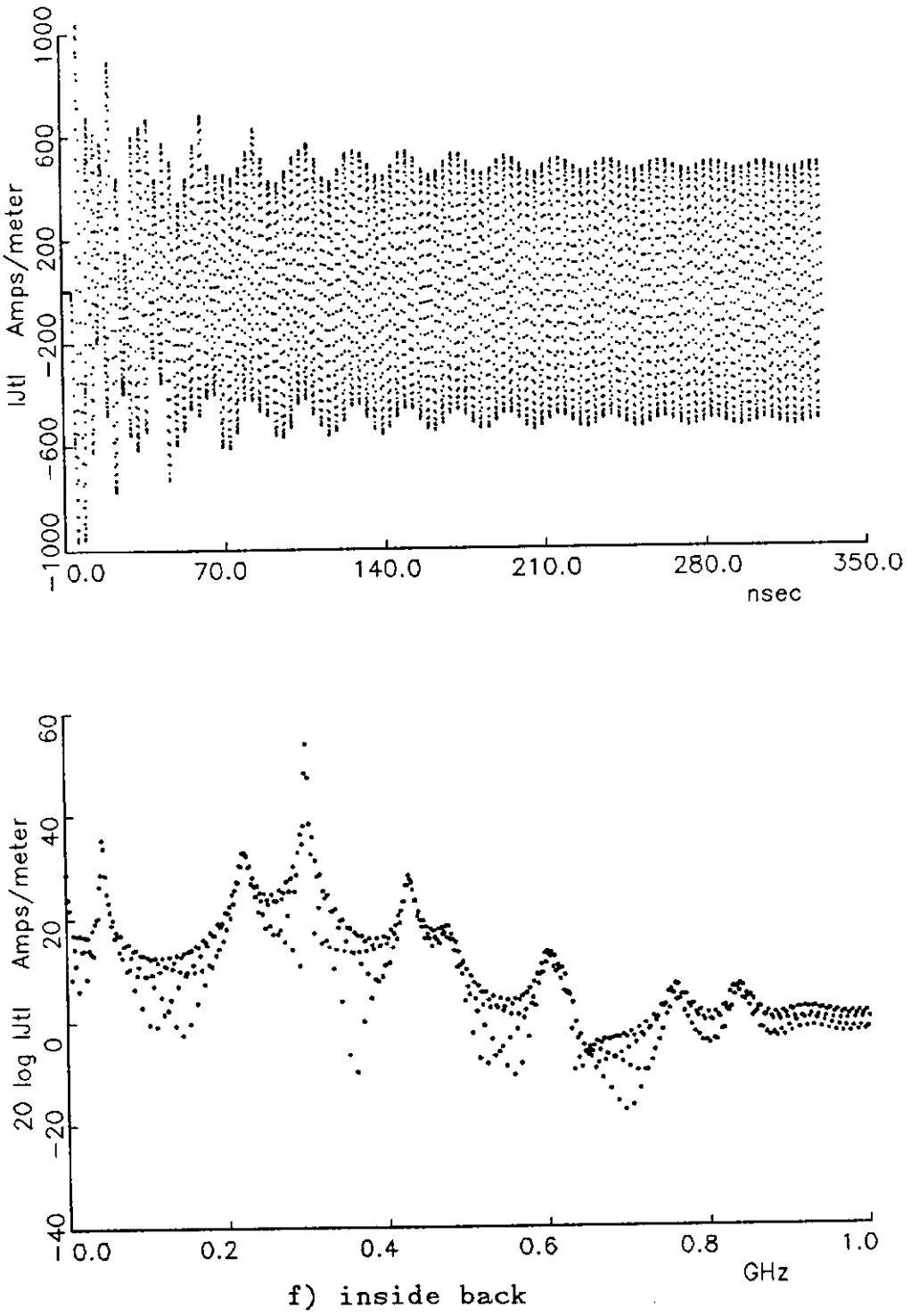


figure 6-7. (continued) Time and frequency domain plots of TE mode surface currents at six locations around the surface of a slotted cavity excited with a 300 MHz incident wave; a) outside front, b) outside right, c) outside back, d) inside front, e) inside right, f) inside back

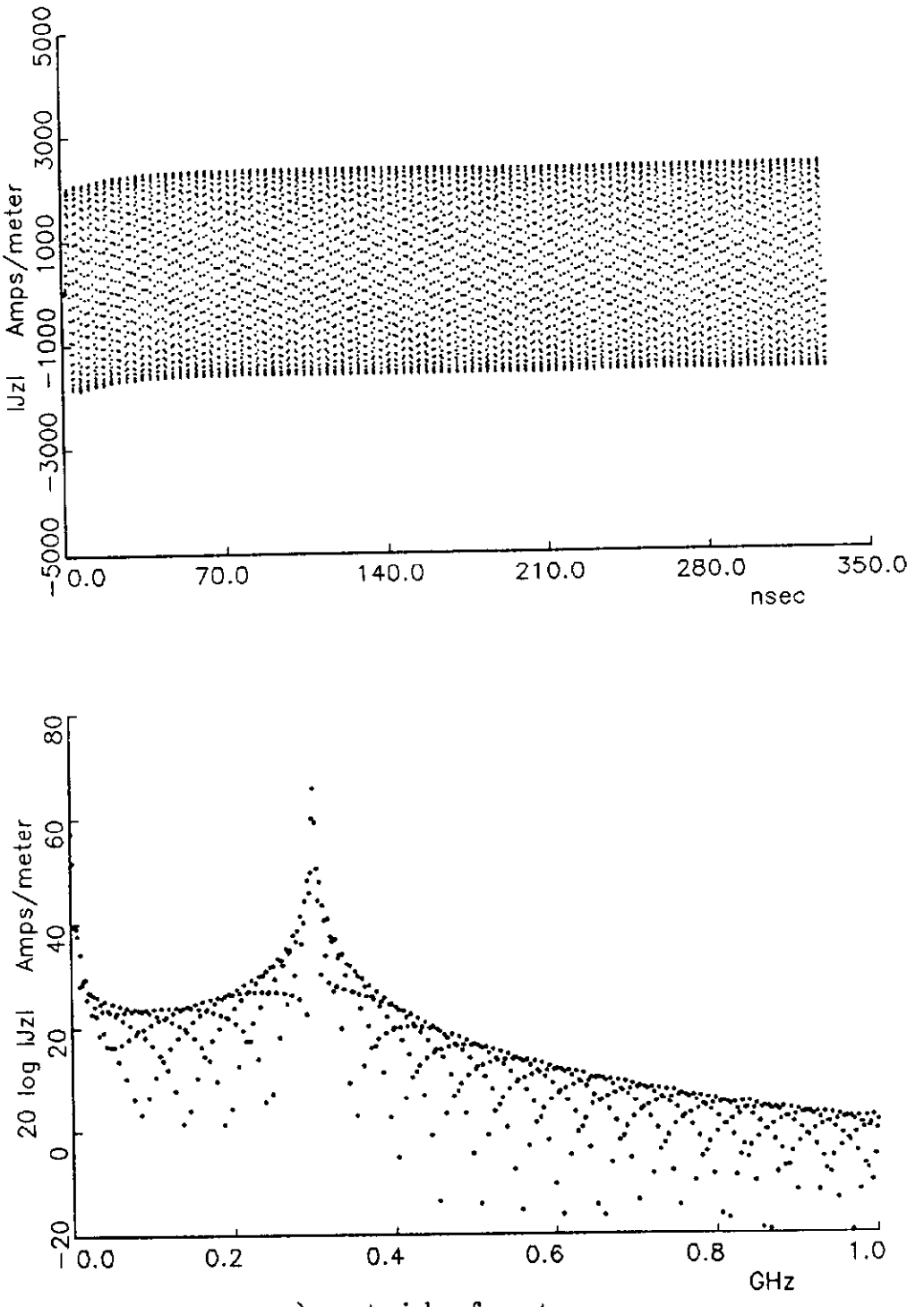


a) outside front

figure 6-8. Time and frequency domain plots of TM mode surface currents at six locations around the surface of a slotted cavity excited with a 300 MHz incident wave; a) outside front, b) outside right, c) outside back, d) inside front, e) inside right, f) inside back

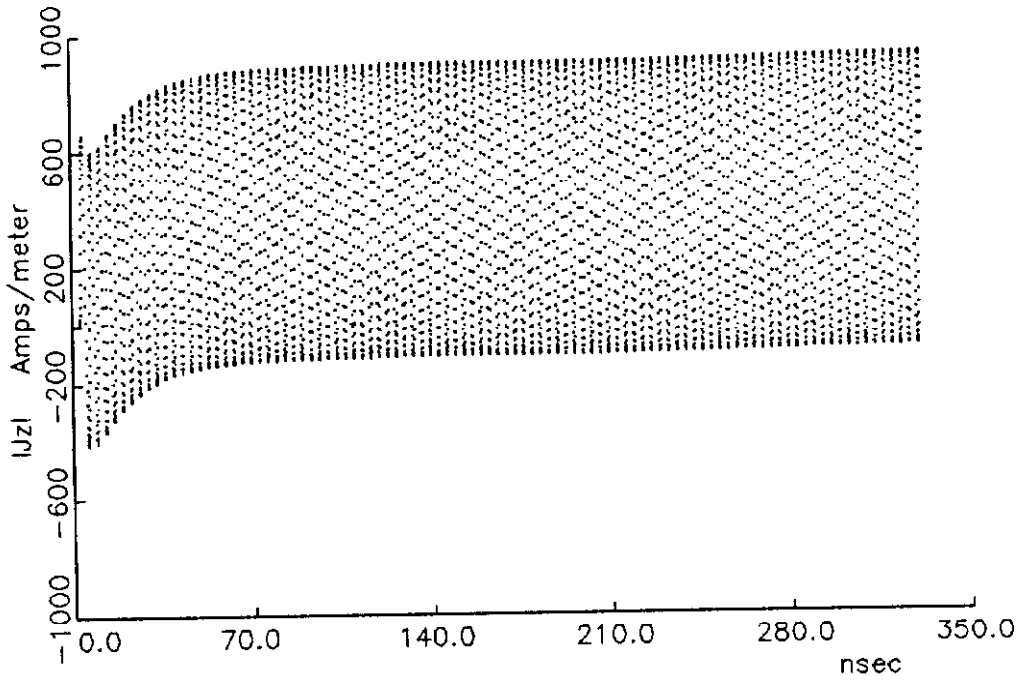


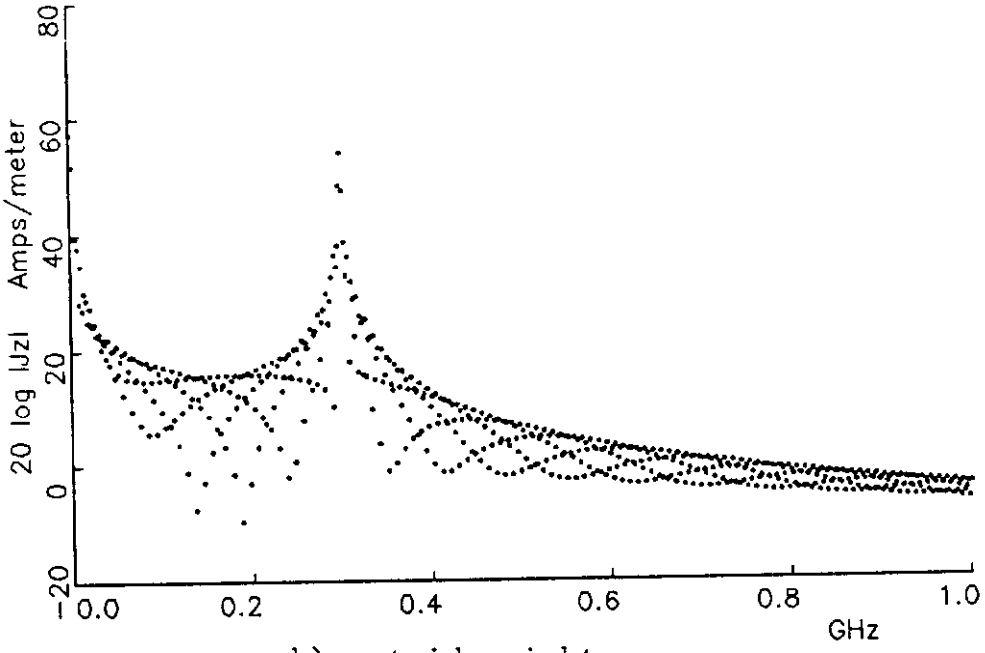


b) outside right

figure 6-8. (continued) Time and frequency domain plots of TM mode surface currents at six locations around the surface of a slotted cavity excited with a 300 MHz incident wave; a) outside front, b) outside right, c) outside back, d) inside front, e) inside right, f) inside back

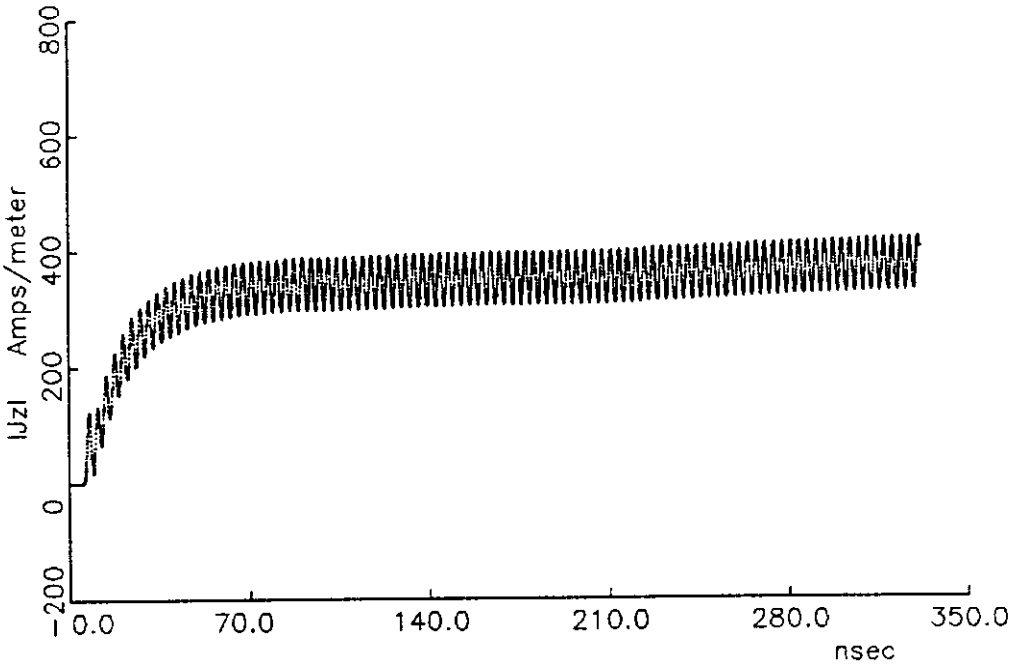


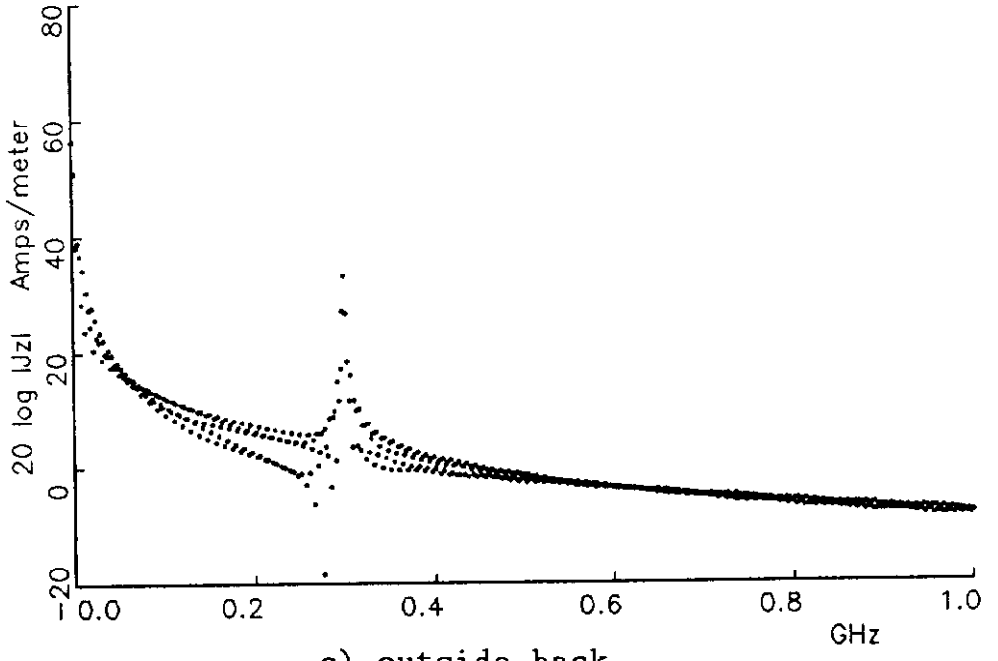


c) outside back

figure 6-8. (continued) Time and frequency domain plots of TM mode surface currents at six locations around the surface of a slotted cavity excited with a 300 MHz incident wave; a) outside front, b) outside right, c) outside back, d) inside front, e) inside right, f) inside back

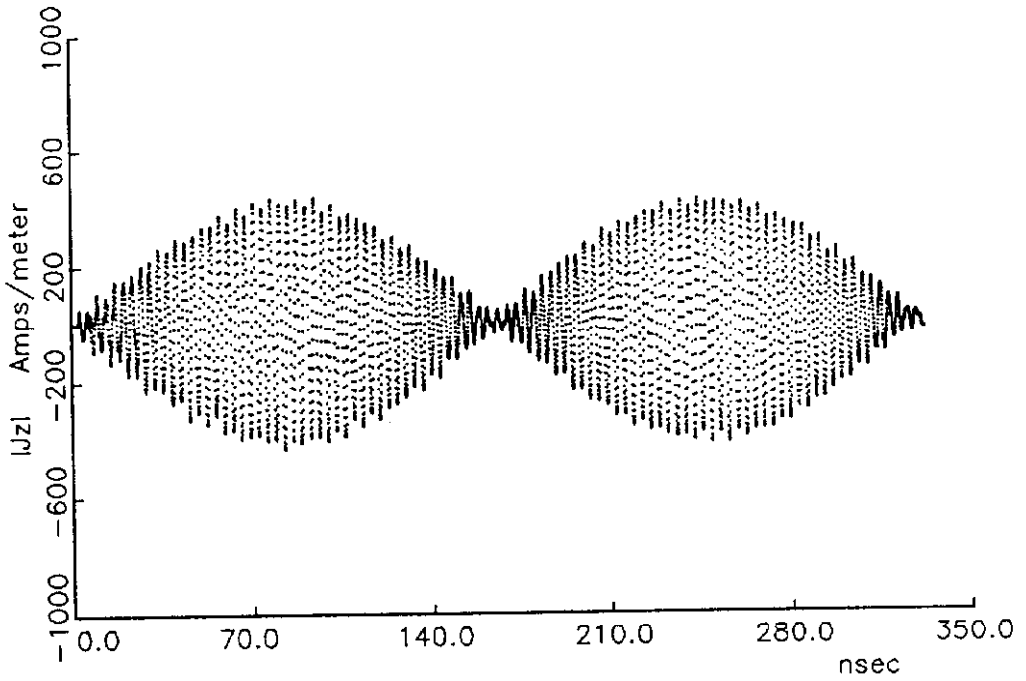


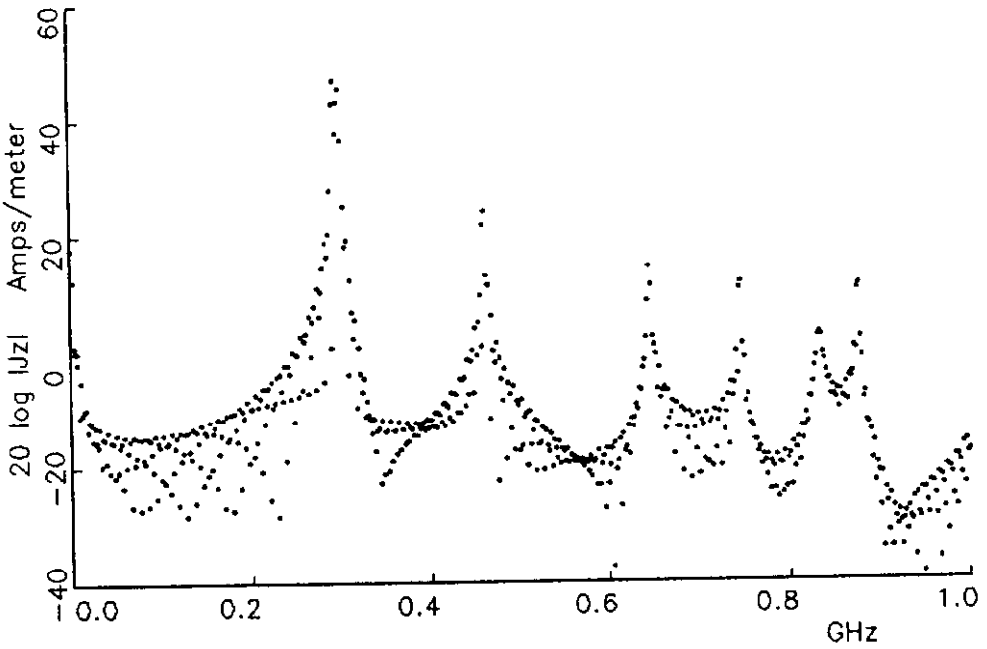


d) inside front

figure 6-8. (continued) Time and frequency domain plots of TM mode surface currents at six locations around the surface of a slotted cavity excited with a 300 MHz incident wave; a) outside front, b) outside right, c) outside back, d) inside front, e) inside right, f) inside back

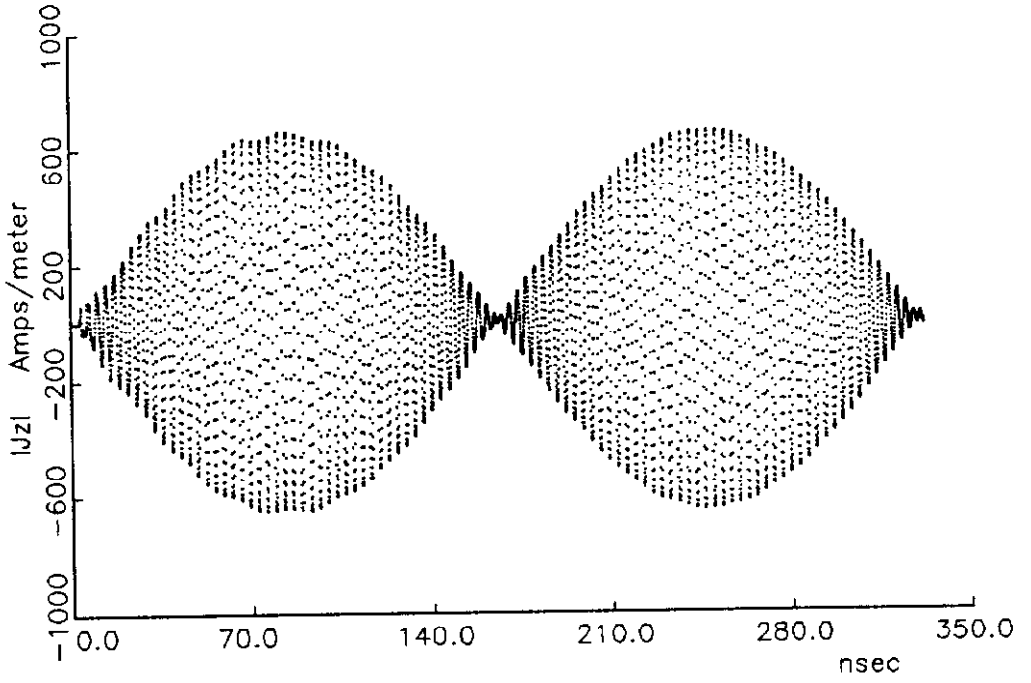


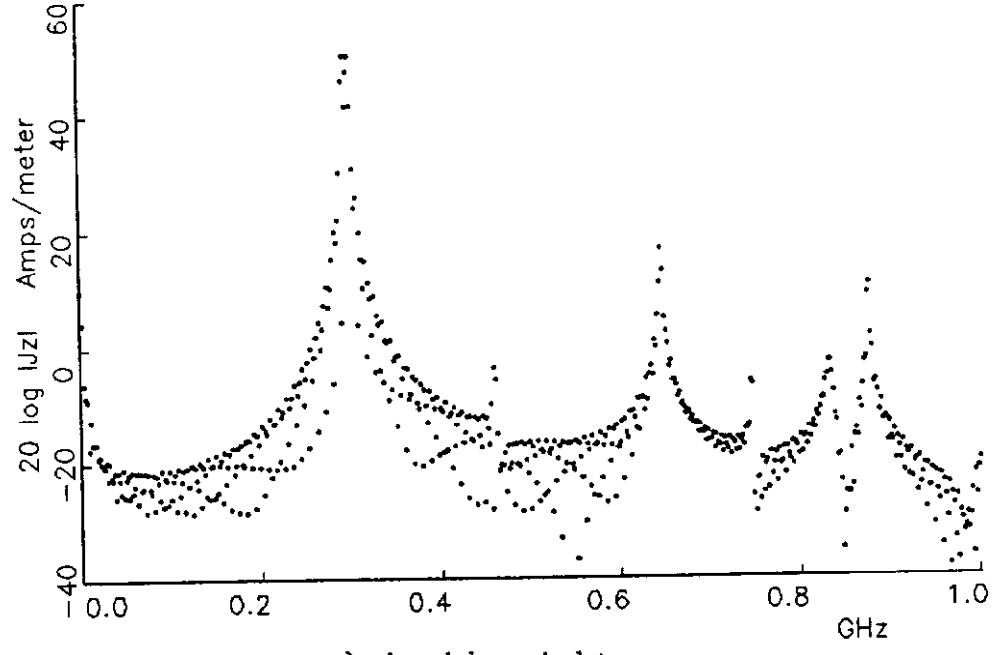


e) inside right

figure 6-8. (continued) Time and frequency domain plots of TM mode surface currents at six locations around the surface of a slotted cavity excited with a 300 MHz incident wave; a) outside front, b) outside right, c) outside back, d) inside front, e) inside right, f) inside back

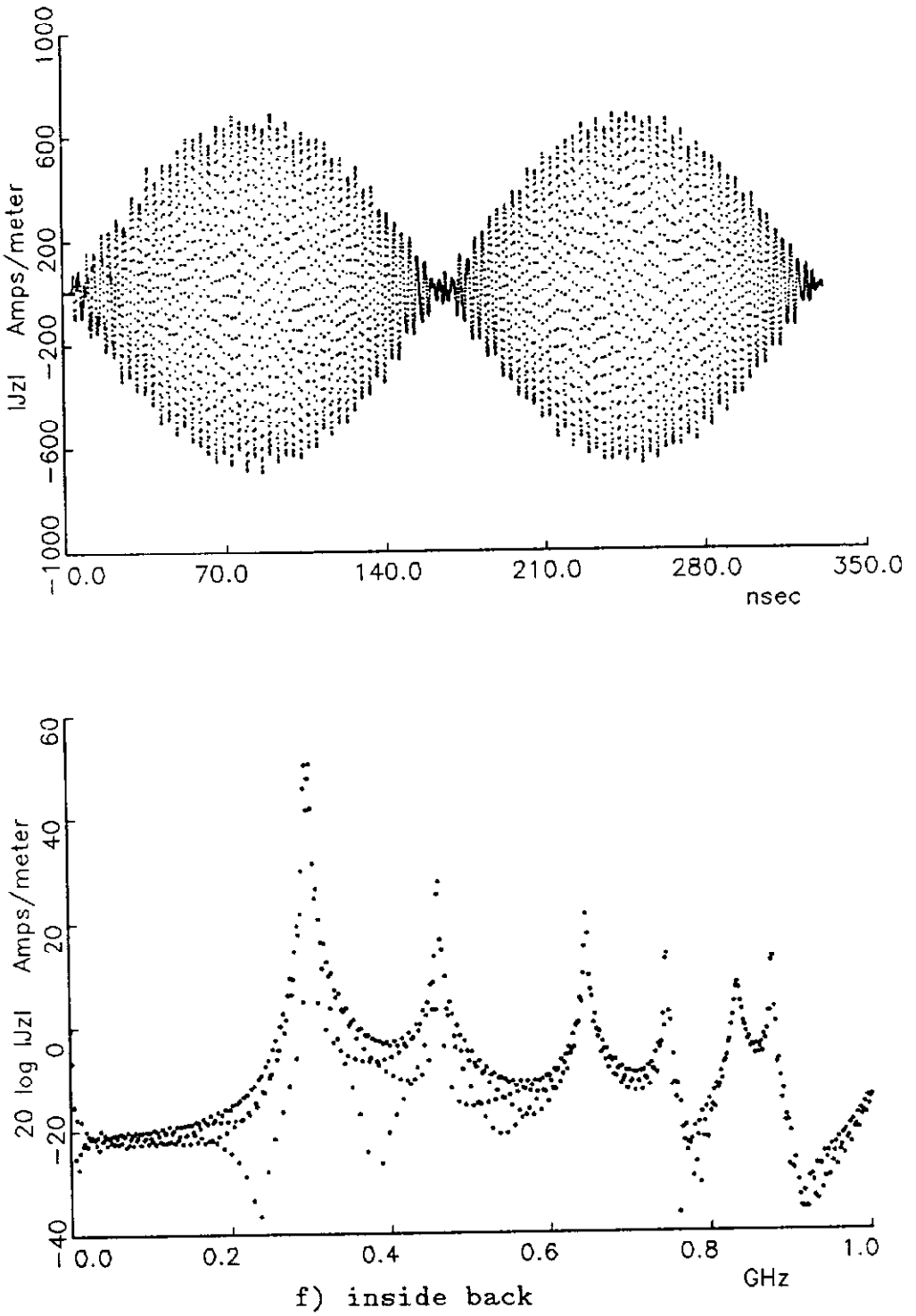


figure 6-8. (continued) Time and frequency domain plots of TM mode surface currents at six locations around the surface of a slotted cavity excited with a 300 MHz incident wave; a) outside front, b) outside right, c) outside back, d) inside front, e) inside right, f) inside back

Energy at all frequencies is generated by abruptly turning on the 300 MHz incident plane wave. The excitation in the frequency domain can be thought of as the convolution of a 300 MHz plane wave with a pulse function having a period of 8192 $\Delta t$, equal to 1 for 5000 $\Delta t$ and zero for (8192-5000) $\Delta t$. This is also what causes the patterns below the noise level in the frequency domain, most notable in the plots of the outside fields. This did not show up when the time record was truncated to 4096 points, prior to the application of the fast Fourier transform in figure (6-9). The nulls in these plots are caused by the window function which is slightly different in each because of the propagation delay difference between the three locations shown.

Another interesting phenomenon is the presence of 44.5 MHz in the TE case. On the inside this component has an amplitude of roughly 30 db and on the outside it is 10 times smaller. The TE case will excite currents in the structure which circulate around its cross section. The 20 db difference between the inside and outside amplitudes implies that the inside and outside are not coupled very strongly. However, the frequencies are identical at least to the resolution of the plot. The outside circumference is 4x20, or 80, cells; this is one half wavelength at 47.1 MHz. On both the inside and outside surfaces, there must be separate surface current modes whose resonant frequencies are shifted somewhat, and possibly coupled, through the complex impedance of the slot. For the inside TE case, this 44.5 MHz has a significant effect on the convergence of the 300 MHz component of the field.

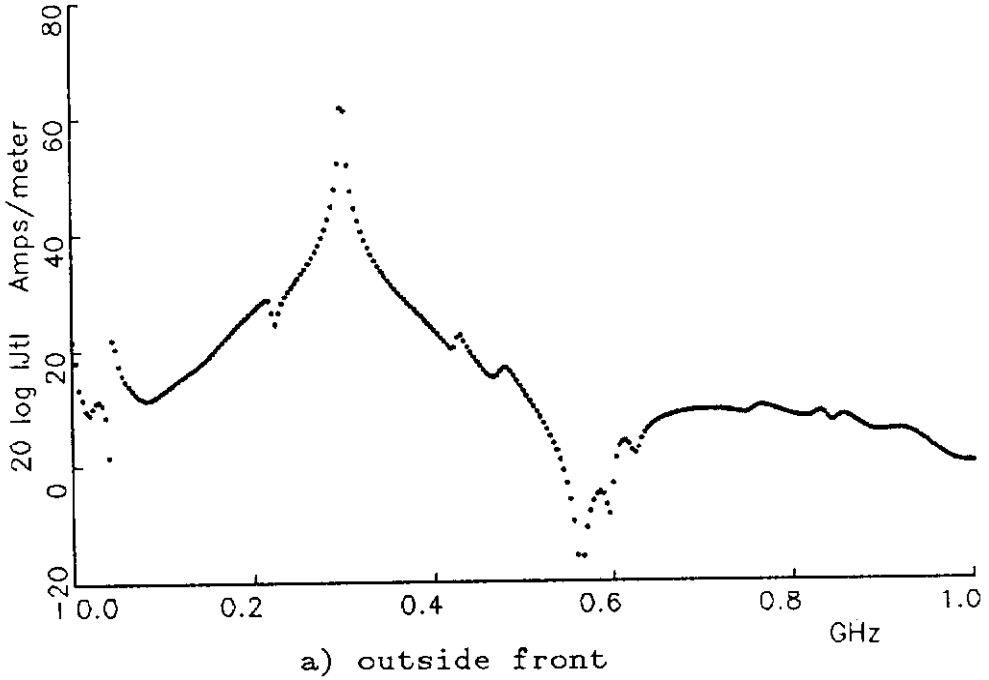


a) outside front

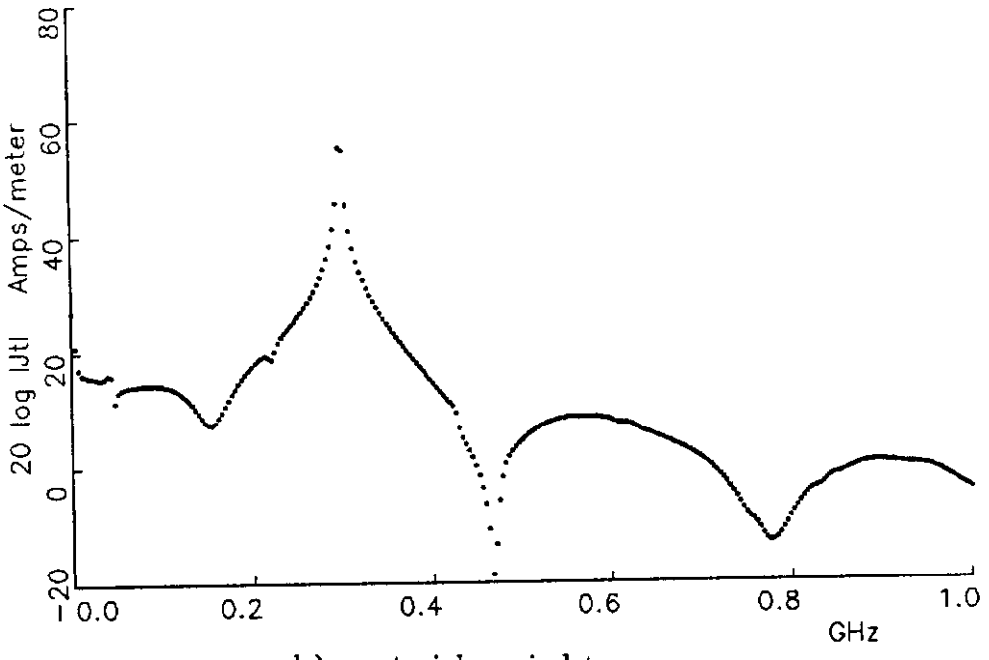


b) outside right

figure 6-9. Fourier transform of TE mode surface currents on the slotted cavity with the time domain record truncated to 4096 points; a) outside front, b) outside right, c) outside back

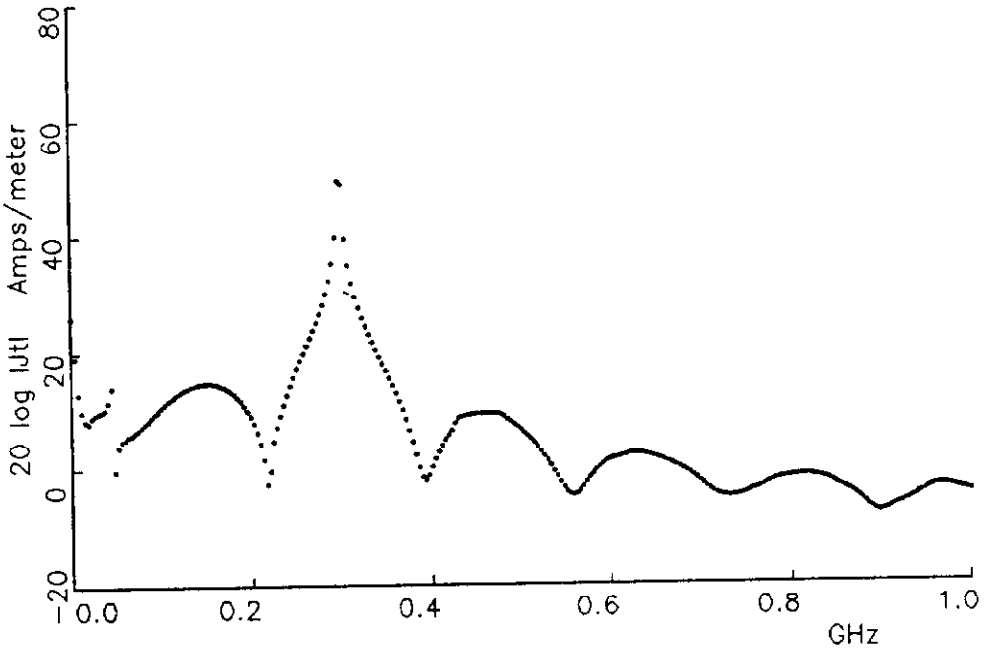


c) outside back

figure 6-9. (continued) Fourier transform of TE mode surface currents on the slotted cavity with the time domain record truncated to 4096 points; a) outside front, b) outside right, c) outside back

As an example, at the center of the inside right face, the 44.5 MHz modulation is 8% of the 300 MHz amplitude after 5000 time steps. The magnitude and phase algorithm, used in figure (6-5), will reduce this component by a factor of two. This algorithm calculates the magnitude from the maximum and minimum values of the field, which are separated by 1/2 of the 300 MHz period. In this period of time, the 44.5 MHz will have only a 27° phase advance, resulting in a maximum difference of 45% of its peak value.

The time domain plot at the center of the outside back surface, shown in figure (6-8), reveals the reason for the differences between the MOM and FD-TD results seen in figure (6-5) for the TM case. Because an infinitely long structure is being modeled, it will have a TM mode resonance at zero frequency. The offset, which arises because of this mode, caused the magnitude and phase algorithm to fail. From the frequency domain plot, the 300 MHz component has an amplitude of 33.12 db or 45.3 amps/meter at the center of the outside back. The MOM result was 38.7 amps/meter.

As shown in section (6.4), when this structure is excited with a pulse, it has a lowest order TM mode at a frequency of about 294 MHz, only 6 MHz away from the 300 MHz incident plane wave. The difference frequency would have a period of 167 nsec, which corresponds nicely with the 165 nsec period of the beat frequency appearing on the inside surfaces for the TM case, see figure (6-8). Noting that our first MOM/FD-TD comparison stopped after 15 cycles, 750 time steps or 49.7 nsec, the correlation between MOM and FD-TD

for the inside surface currents was largely due to the choice of time step. For the TM case the algorithm has difficulty with a DC offset, and does not average over a long enough period of time to smooth out the 6 MHz oscillations.

Finally, with a time step of $\Delta/2c$ = 66.3 psec, the bandwidth should be 7.54 GHz. Figure (6-10) is the Fourier transform from the TM case inside back surface, covering DC to 5 GHz. There is a clear discontinuity in the plot at 2.5 and 3.75 GHz. From the dispersion relation, the phase velocity goes to zero when the cell size equals; $\lambda/3$, or 2.5 GHz, for a 0° angle of propagation and $\lambda/4$, or 3.75 GHz, for a 45° angle of propagation. This dependence of phase velocity on wavelength or frequency has the effect of a low pass filter on the model. It also must shift resonant modes towards lower frequencies. The amount of shift depends on the angle at which energy of the mode travels or oscillates within the grid and its frequency. Because the velocity actually goes to zero, the model must compress all possible modes within the 3.75 GHz limit. If one knew the angle and thus the appropriate velocity shift, the spectrum could be corrected. Although easily done for a specific, well understood mode, this would be impractical in general because all angles are possible.

## 6.4 Slotted cavity with gaussian pulse excitation

For a rectangular two-dimensional cavity, as shown in figure (6-11) below, the resonant frequencies are given by equation (6.5).

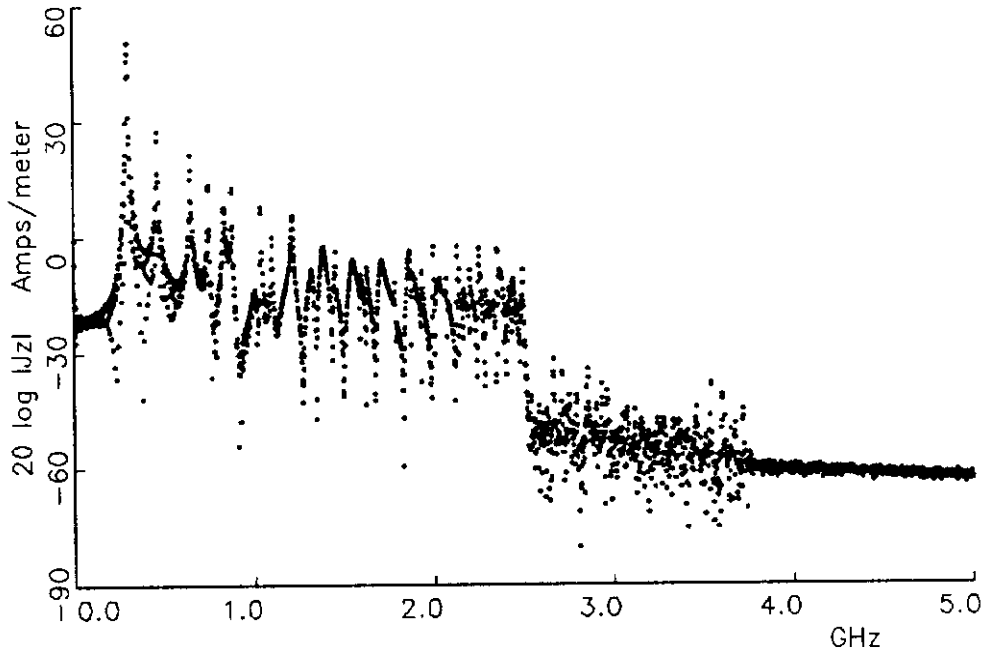


figure 6-10. 5 GHz fourier transform of the inside back surface current for the TM mode

$$\text{resonant frequency} = \frac{v}{2}\sqrt{\left(\frac{m}{a}\right)^2 + \left(\frac{n}{b}\right)^2} \qquad (6.5)$$

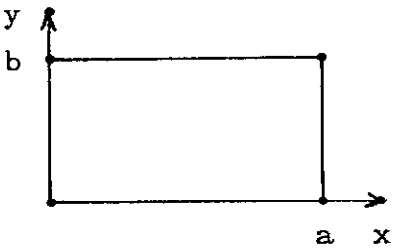


figure 6-11. Cross section of two-dimensional cavity resonator.

In equation (6.5), a is the x dimension width, and b is the y dimension width. The indices m and n are the mode numbers, m being the number of half wave variations of the magnitude of a field component along the x axis, and n that for the y axis. For example, with m = 1 and n = 2 the $TM_{12}$ mode has a z directed electric field given by (5);

$$Ez = E_o \sin\frac{m\pi x}{a} \sin\frac{n\pi y}{b} \qquad (6.6)$$

When m = 1, Ez is zero at x = 0 and a, for one half wave variation. For n = 2, Ez is zero at y = 0, b/2, and b, for two half wave variations. This type of resonator will not support a TM mode with m or n = 0, as it would require a tangential electric field at the surface of a conductor. For a square cavity, the resonant frequency of the $TE_{mn}$ mode is the same as that for the $TE_{nm}$, $TM_{nm}$ and $TM_{mn}$ modes. The presence of the slot will break this symmetry. Since the incident plane wave has no y directed field components, all modes may not be excited.

In order to study the modes of the slotted cavity, the structure was excited with an incident plane wave which had a gaussian time dependence. This is particularly nice, as a gaussian in the time domain is also a gaussian in the frequency domain.

$$g(t) = A\, e^{-\frac{1}{2}\left(\frac{t}{\sigma_t}\right)^2} \tag{6.7}$$

$$G(f) = \frac{A}{\sigma_f \sqrt{2\pi}}\, e^{-\frac{1}{2}\left(\frac{f}{\sigma_f}\right)^2} \tag{6.8}$$

The bandwidth in the frequency domain, $\sigma_f$, is just $1/2\pi\sigma_t$. In the FD-TD code, a time step of $\Delta t = \Delta/2c = 66.315$ psec and a spatial step of $\Delta = .0397888$ meters were used. Selecting a $\sigma_f$ of 200 MHz provided a $\sigma_t$ of 796 psec, or only 12 time steps. The gaussian pulse is delayed by 200 time steps, or 16.7 $\sigma_t$, in order to minimize any transients caused by abruptly turning on the source. Using a smaller $\sigma_t$ would allow probing higher frequencies but would require a rather coarse approximation of a gaussian time pulse. In addition, a larger bandwidth pulse would suffer more from distortion caused by dispersion at the higher frequencies. Thus a gaussian pulse will not excite the higher frequency modes which get compressed at the algorithm's cut off frequencies of 2.5 and 3.75 GHz. An impulse excitation would tend to excite these.

Figures (6-12) and (6-13) show the time domain response to a gaussian pulse at 6 locations around the surface of the scatterer for both the TE and TM cases respectively. Again, the TM case

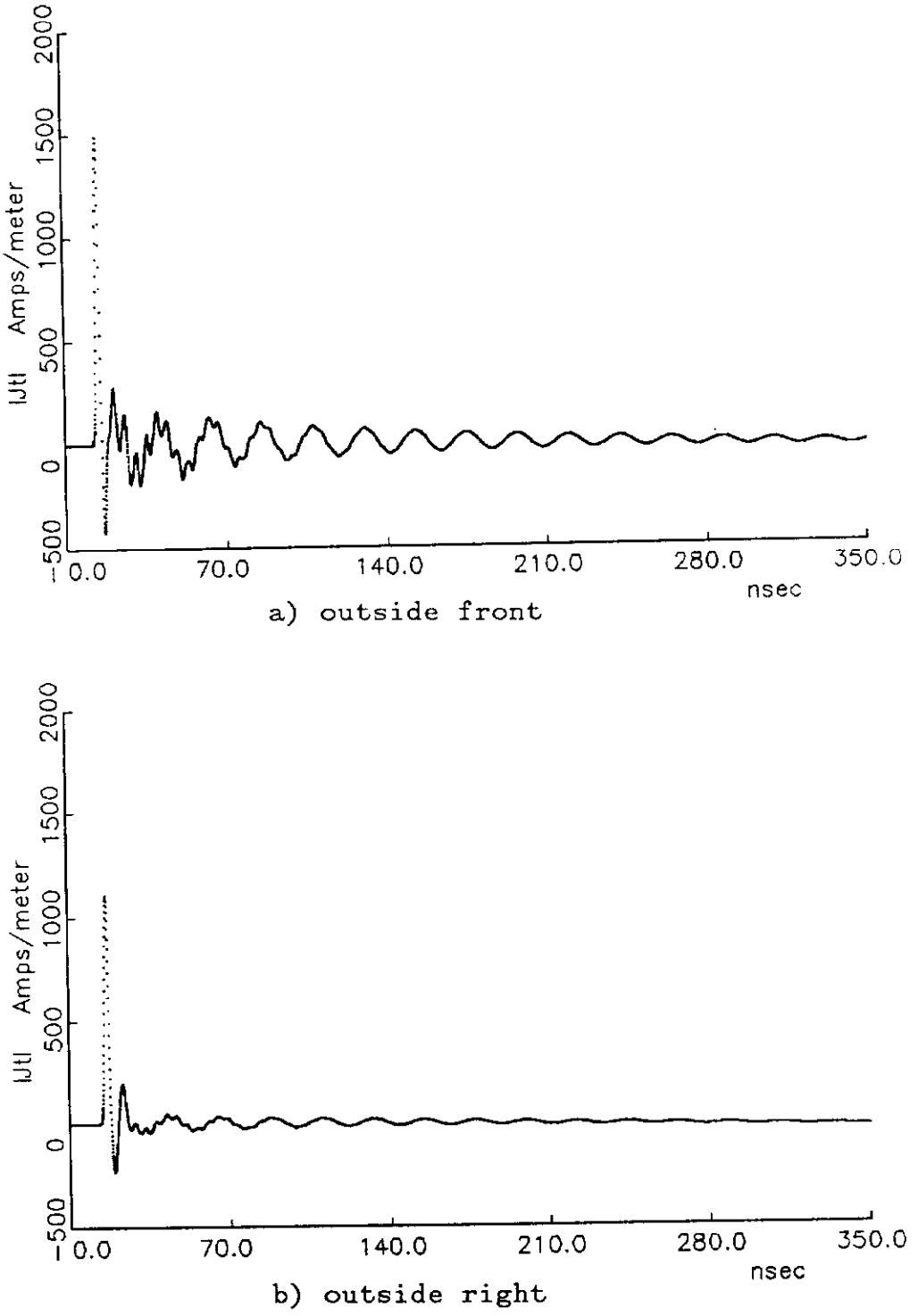


figure 6-12. Time domain plots of TE mode surface currents at six locations around the surface of a slotted cavity excited with a gaussian pulse incident wave; a) outside front, b) outside right, c) outside back, d) inside front, e) inside right, f) inside back

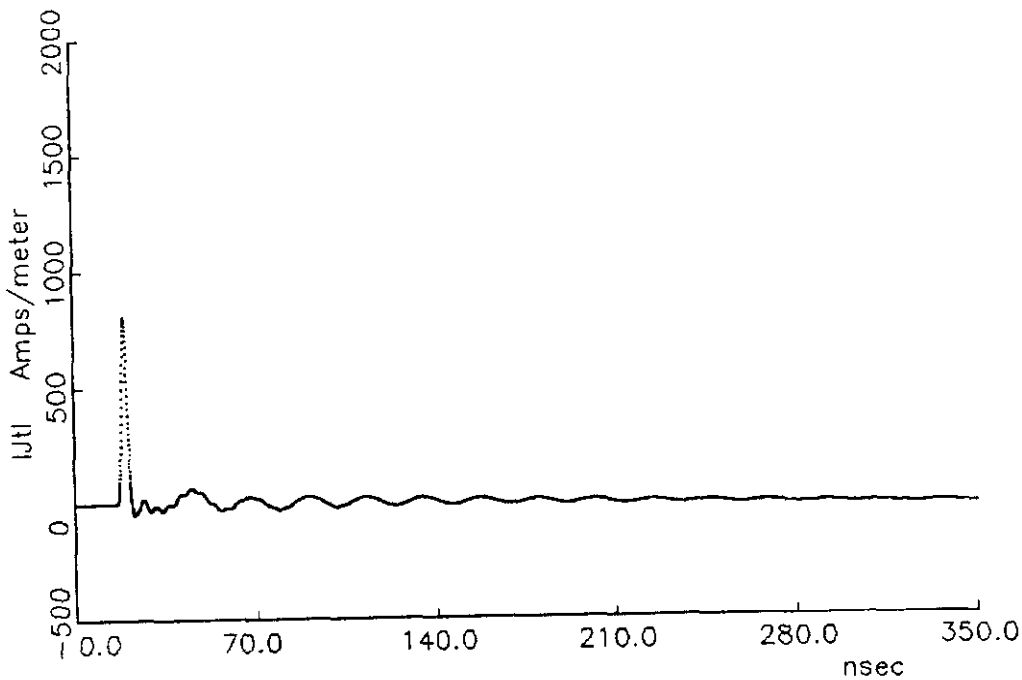


c) outside back

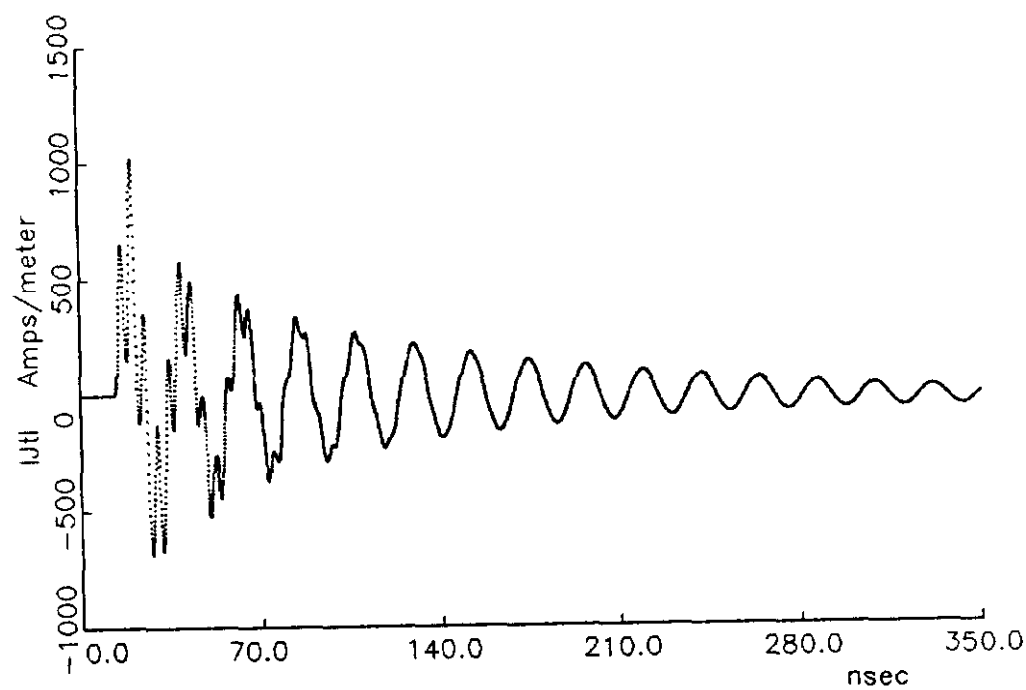


d) inside front

figure 6-12. (continued) Time domain plots of TE mode surface currents at six locations around the surface of a slotted cavity excited with a gaussian pulse incident wave; a) outside front, b) outside right, c) outside back, d) inside front, e) inside right, f) inside back

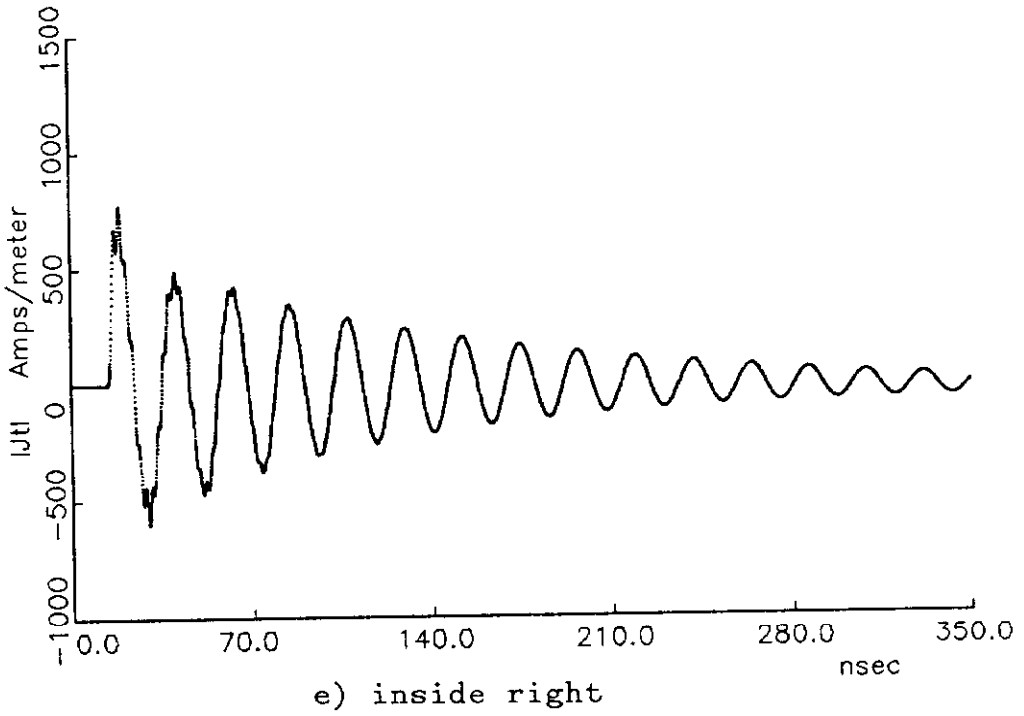


e) inside right

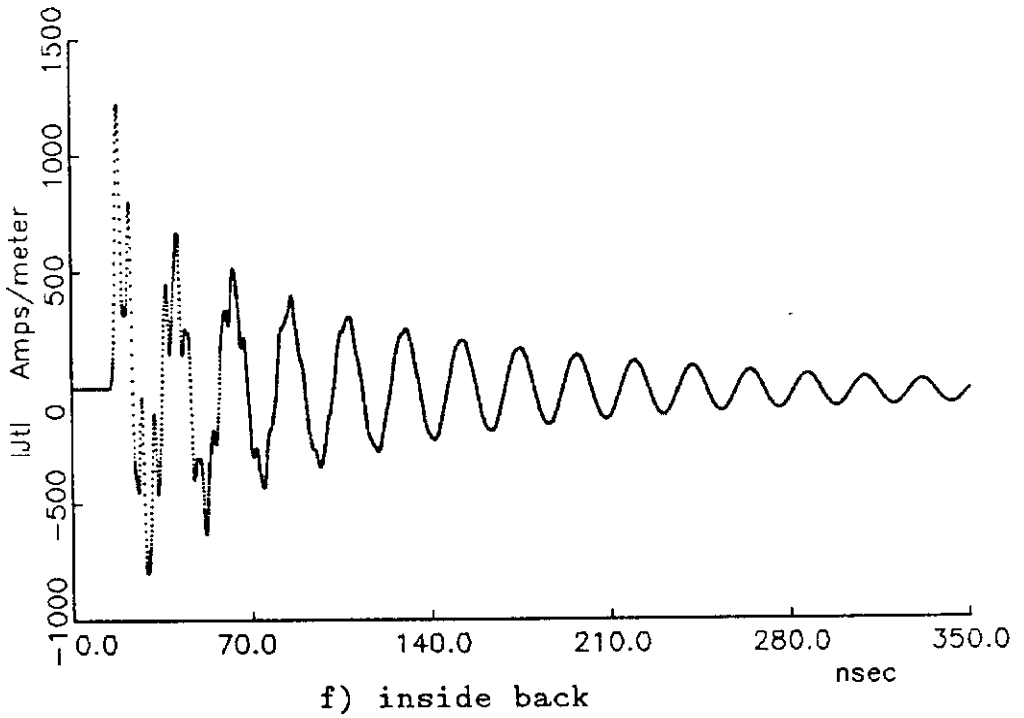


f) inside back

figure 6-12. (continued) Time domain plots of TE mode surface currents at six locations around the surface of a slotted cavity excited with a gaussian pulse incident wave; a) outside front, b) outside right, c) outside back, d) inside front, e) inside right, f) inside back

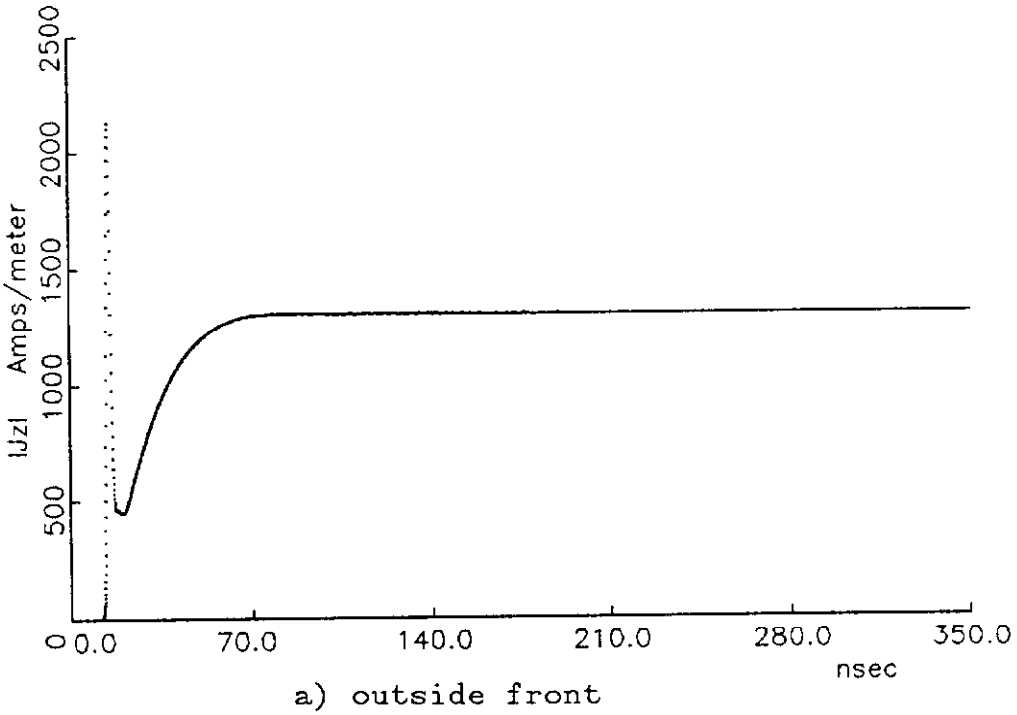


a) outside front

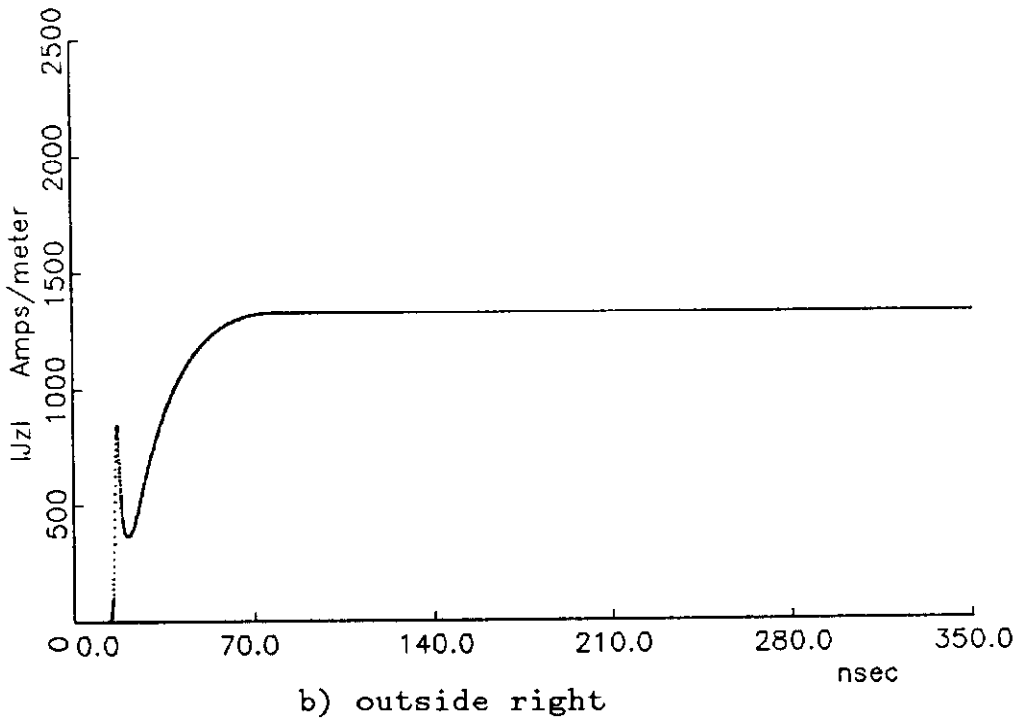


b) outside right

figure 6-13. Time domain plots of TM mode surface currents at six locations around the surface of a slotted cavity excited with a gaussian pulse incident wave; a) outside front, b) outside right, c) outside back, d) inside front, e) inside right, f) inside back

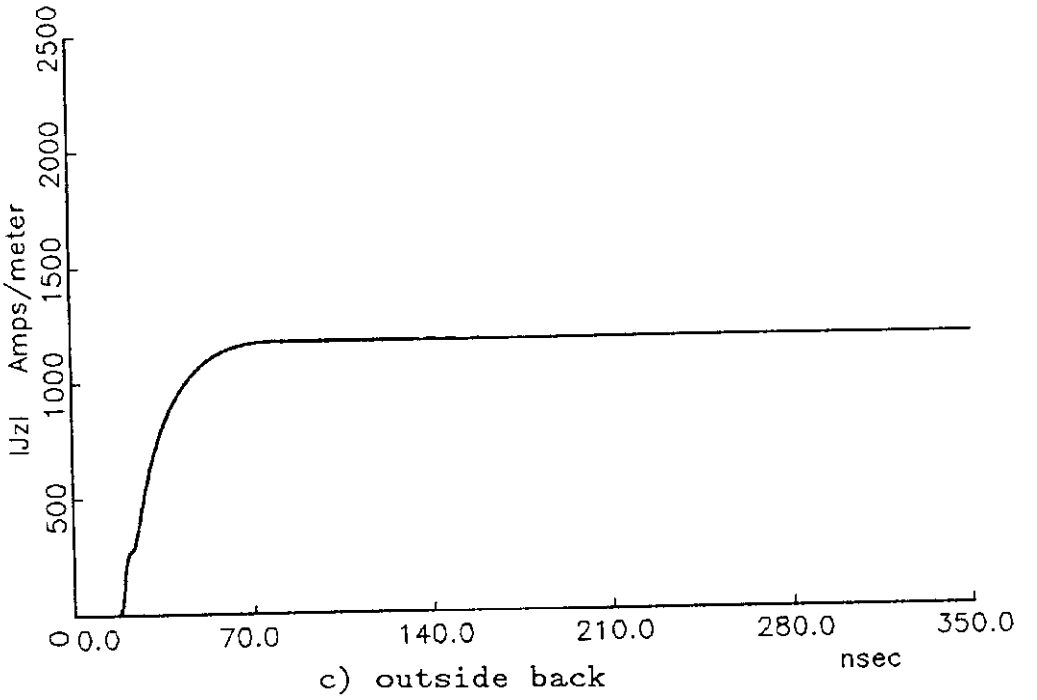


c) outside back

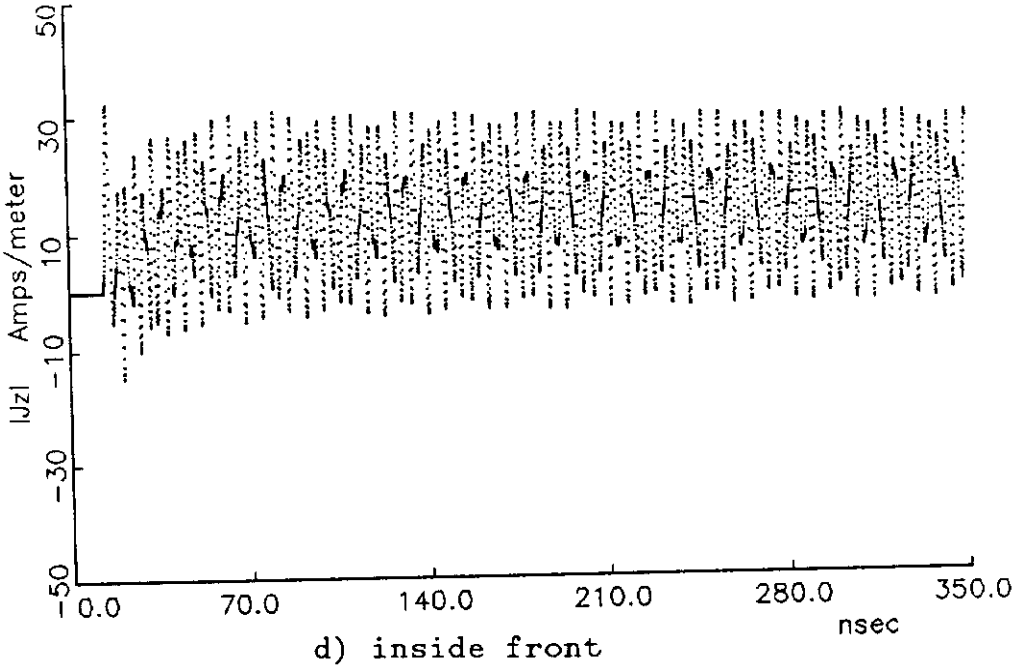


d) inside front

figure 6-13. (continued) Time domain plots of TM mode surface currents at six locations around the surface of a slotted cavity excited with a gaussian pulse incident wave; a) outside front, b) outside right, c) outside back, d) inside front, e) inside right, f) inside back

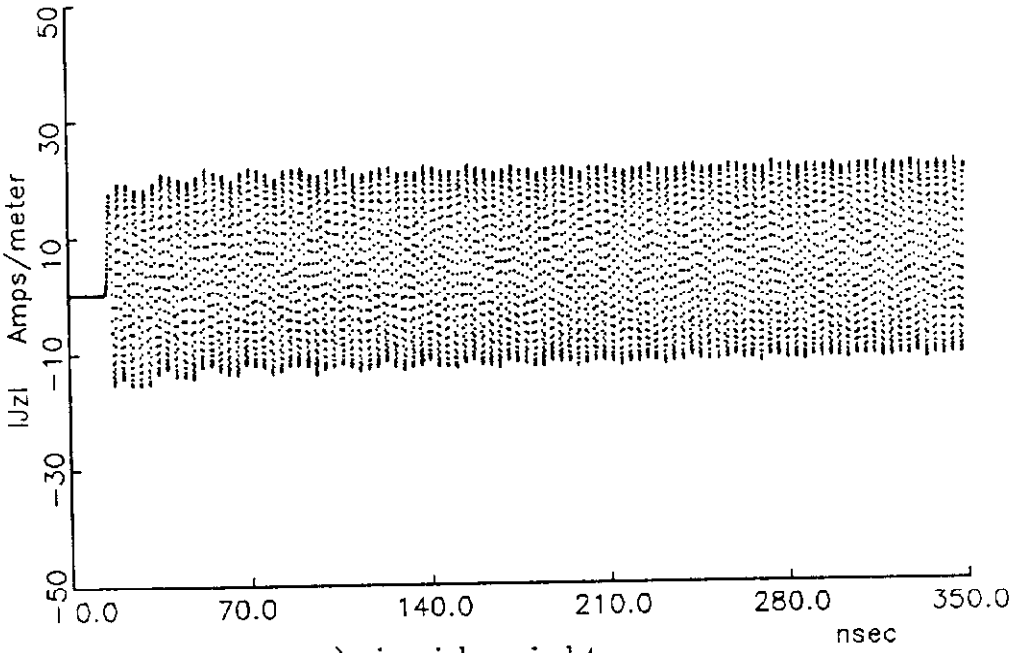


e) inside right

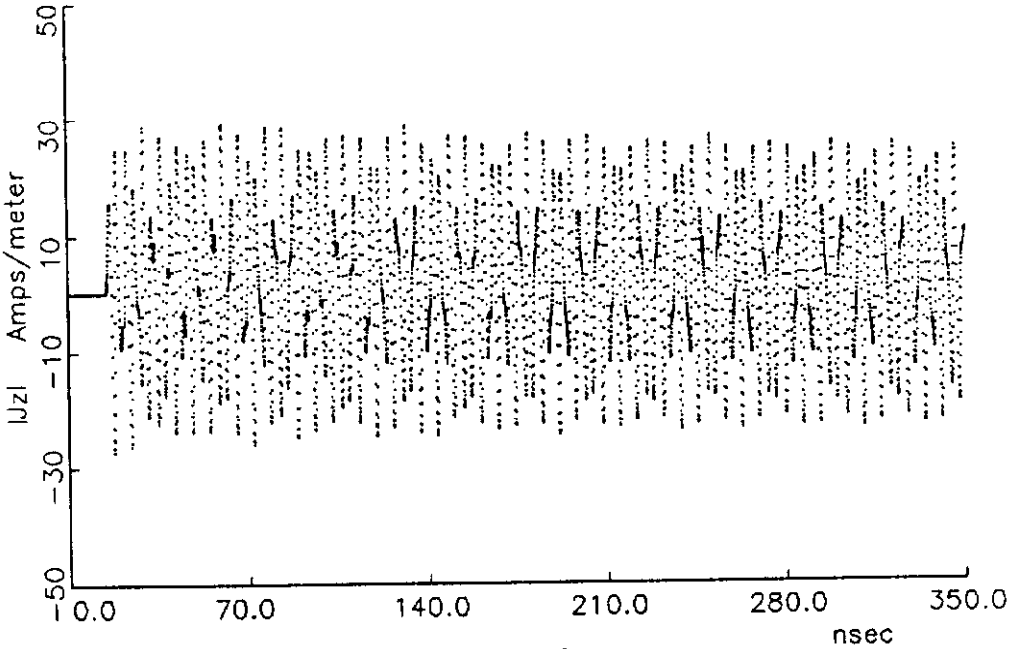


f) inside back

figure 6-13. (continued) Time domain plots of TM mode surface currents at six locations around the surface of a slotted cavity excited with a gaussian pulse incident wave; a) outside front, b) outside right, c) outside back, d) inside front, e) inside right, f) inside back

shows a response at DC and the TE case shows a response at 45 MHz, as described in the previous section. The DC shift in figure (6-13) for the outside back surface is the result of using only Maxwell's curl equations. Static field solutions exist which do do not satisfy the equations $\nabla \cdot \vec{D} = \rho$ and $\nabla \cdot \vec{B} = 0$. It does not pose a problem in this analysis as the low frequency portion of the Fourier transforms can simply be ignored.

A fast Fourier transform was applied to the TE and TM data from the inside center back, see figure (6-14). The frequencies obtained from this figure are listed below along with those calculated from equation (6.5). In view of the fact that the calculation does not take into account the presence of the slot, there is fair agreement between calculation and the FD-TD results.

| mode | FD-TD figure (6-14) | Calculated equation (6.5) |
|---|---|---|
| $TE_{11}$ | 221 MHz | 251 MHz |
| $TM_{11}$ | 294 | 251 |
| $TE_{12}$ | 428 | 468 |
| $TM_{12}$ | 461 | 468 |
| $TE_{22}$ | 603 | 592 |
| $TM_{22}$ | 647 | 592 |

Figure (6-15) shows the effect of normalizing the TM mode case of figure (6-14) with the fourier transform of a gaussian pulse. With the 200 MHz $\sigma_f$ gaussian pulse used, the useful bandwidth is less than 1 GHz.

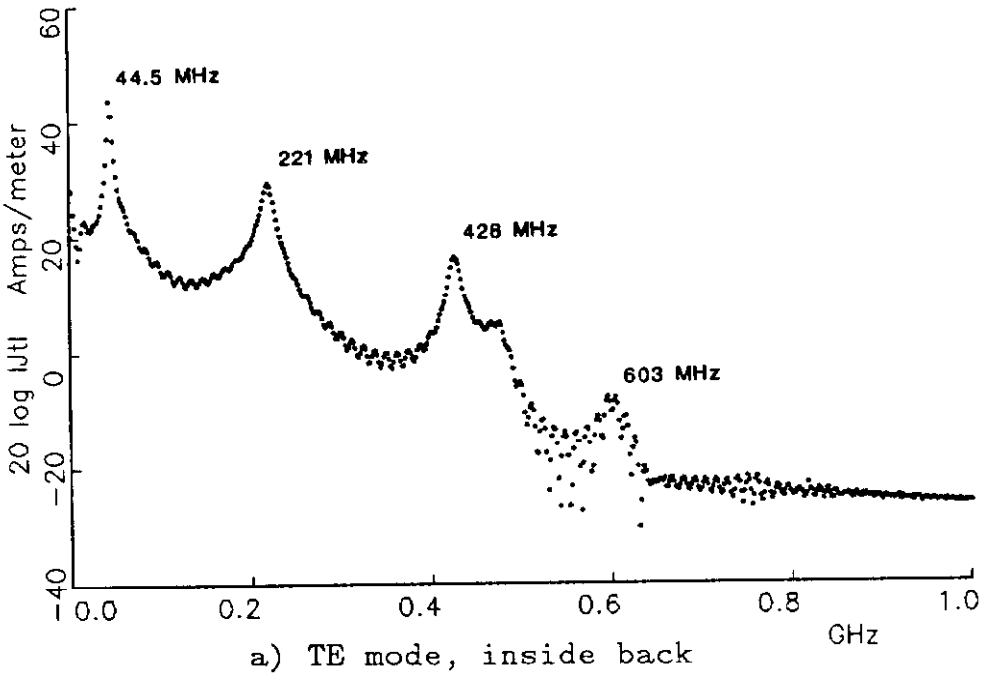


a) TE mode, inside back

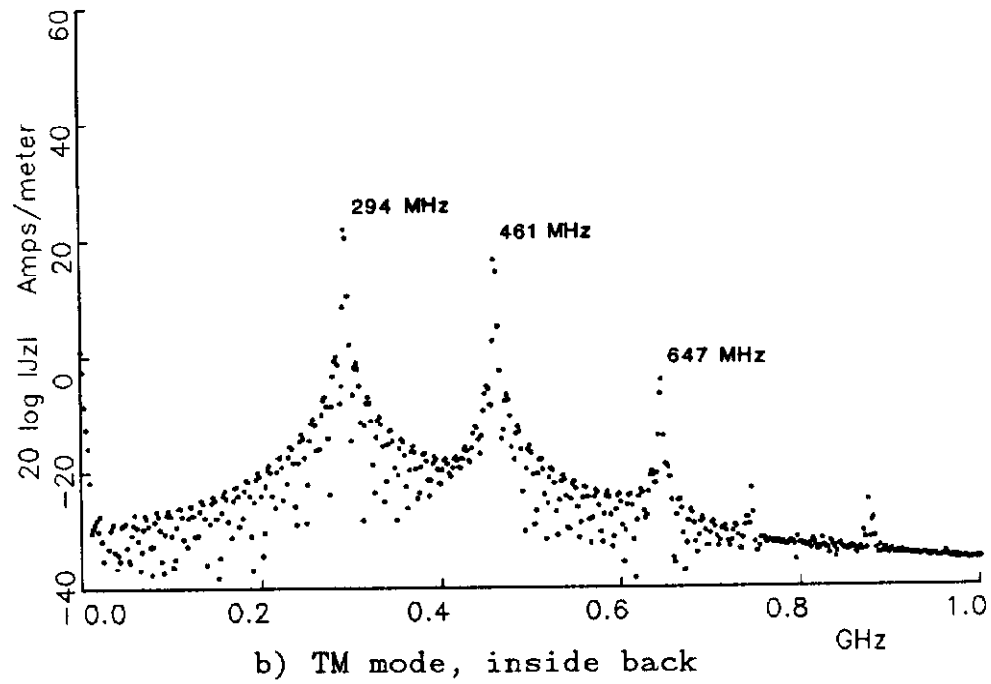


b) TM mode, inside back

figure 6-14. Fourier transform of a) TE and b) TM mode surface currents on the inside back surface of a slotted cavity excited with a gaussian pulse incident wave

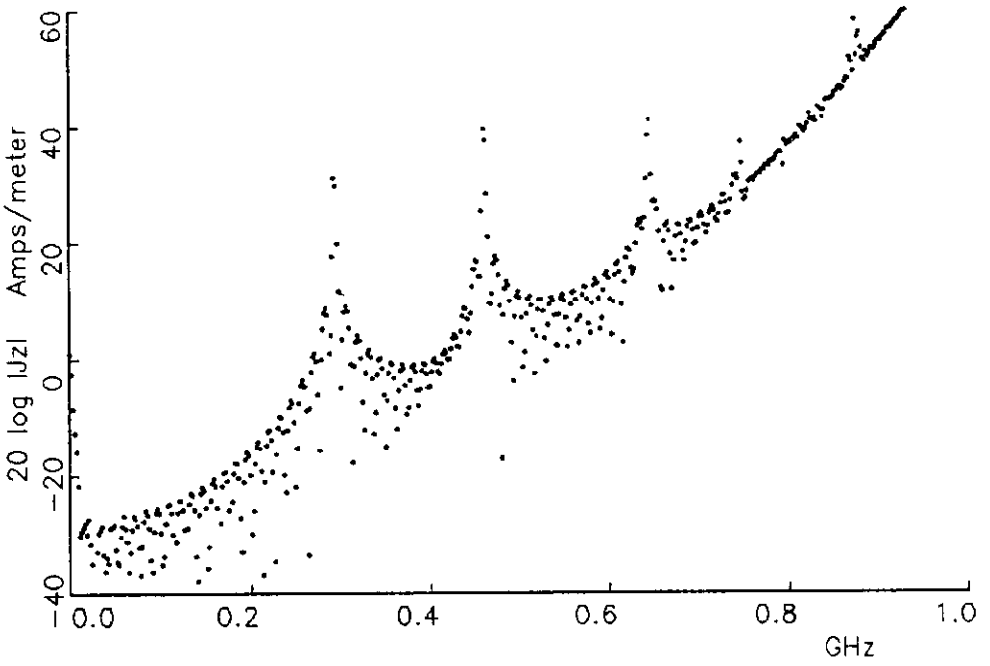


figure 6-15. Effect of normalizing figure (6-14), TM mode, with the Fourier transform of gaussian pulse

# VII. WINDOWS

## 7.1 Application of windows

The next topic discussed is the application of windows to the time domain functions prior to executing the Fourier transform. The windows used are listed below with their definition, assuming N time points (7).

rectangular $w(n) = 1$ (7.1)

Bartlett
$$w(n) = \begin{cases} \frac{2n}{N-1} & 0 \le n \le \frac{N-1}{2} \\ 2 - \frac{2n}{N-1} & \frac{N-1}{2} < n \le N-1 \end{cases} \quad (7.2)$$

Hanning $w(n) = \frac{1}{2}\left(1 - \cos\left(\frac{2\pi n}{N-1}\right)\right)$ (7.3)

Hamming $w(n) = .54 - .46 \cos\left(\frac{2\pi n}{N-1}\right)$ (7.4)

Blackman $w(n) = .42 - .5 \cos\left(\frac{2\pi n}{N-1}\right) + .08 \cos\left(\frac{4\pi n}{N-1}\right)$ (7.5)

Plots of each window's time function and expanded Fourier transform are shown in figure (7-1). To obtain the frequency response, a 1024 point time record containing the window function was generated then zero extended to 32768 points. A fast Fourier transform was then taken and the first 1024 points of that were plotted. This has the effect of increasing the frequency resolution by a factor of 32768/1024 or 32. The horizontal axis of the frequency plot is scaled by this factor, thus a frequency component at n indicates a frequency of n/Ndt, where N represents

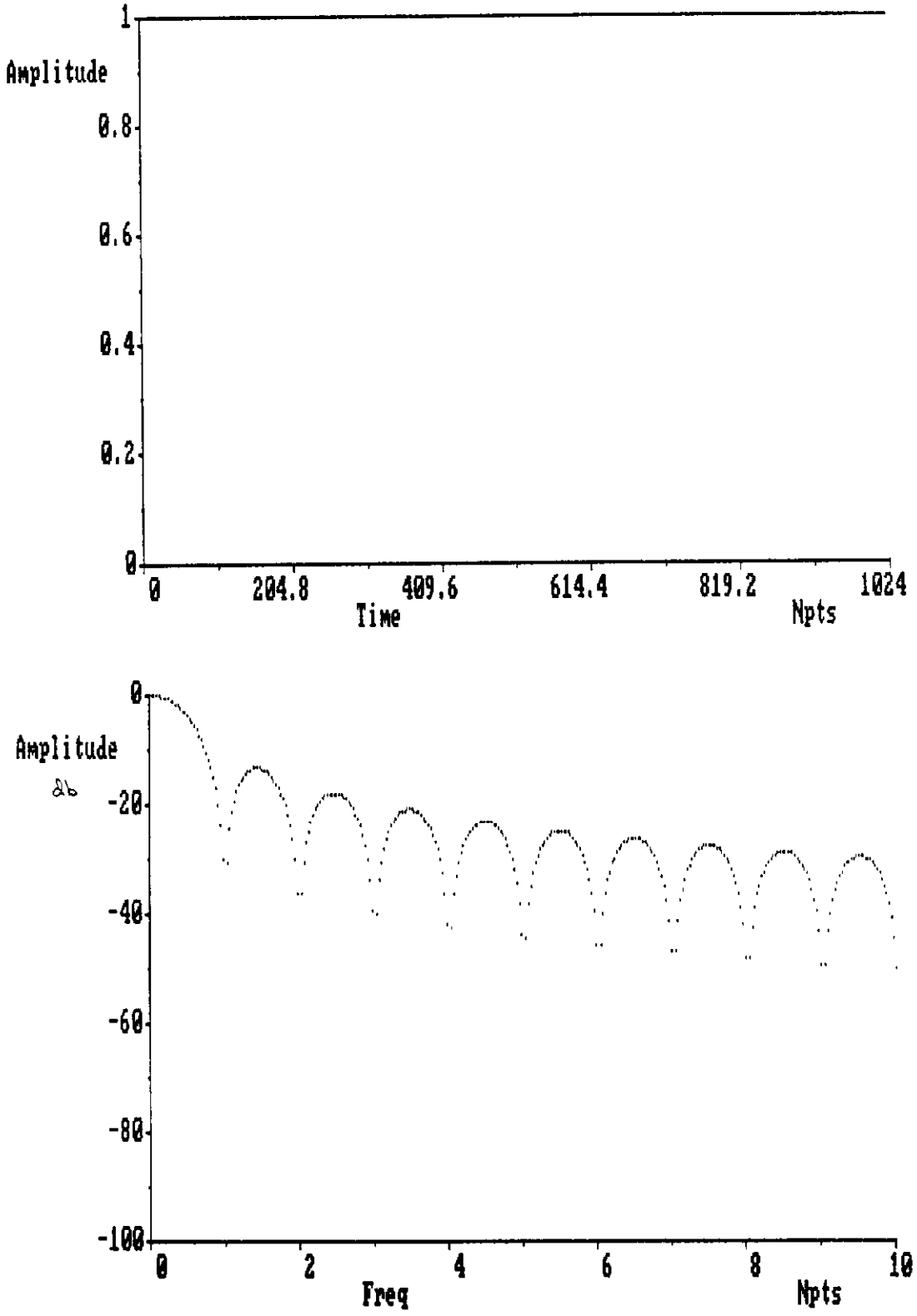


a) rectangular window

figure 7-1. Time and frequency domain plots of window functions; a) rectangular, b) Bartlett, c) Hanning, d) Hamming, e) Blackman

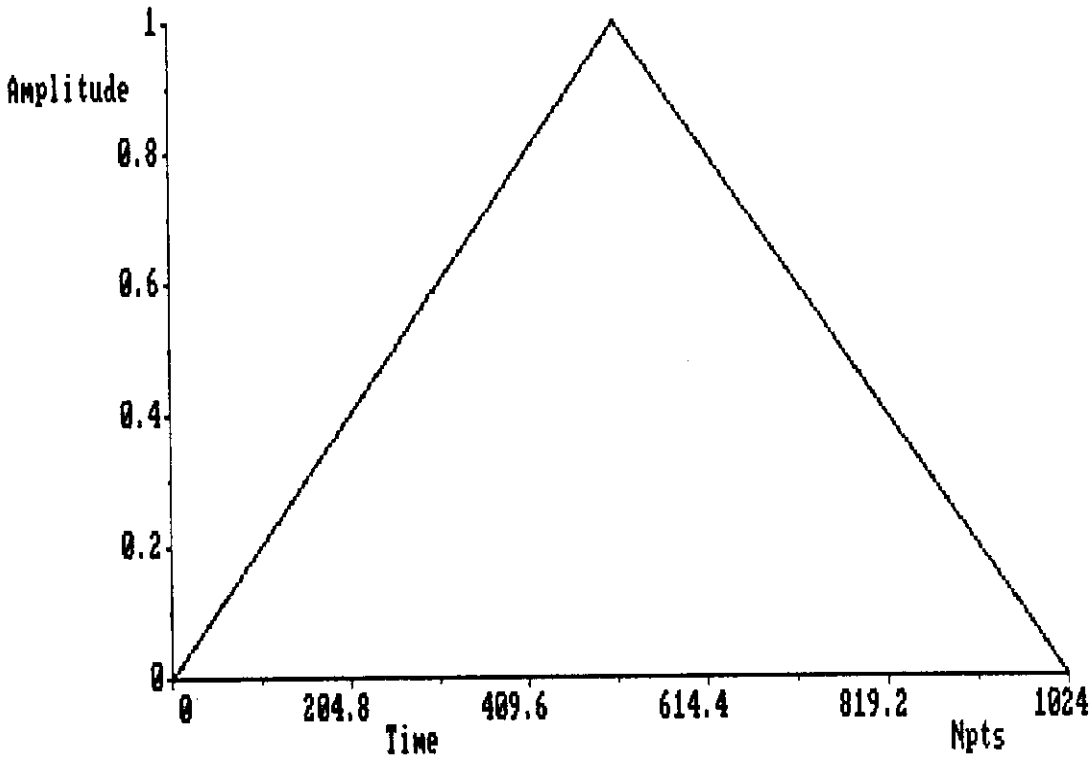


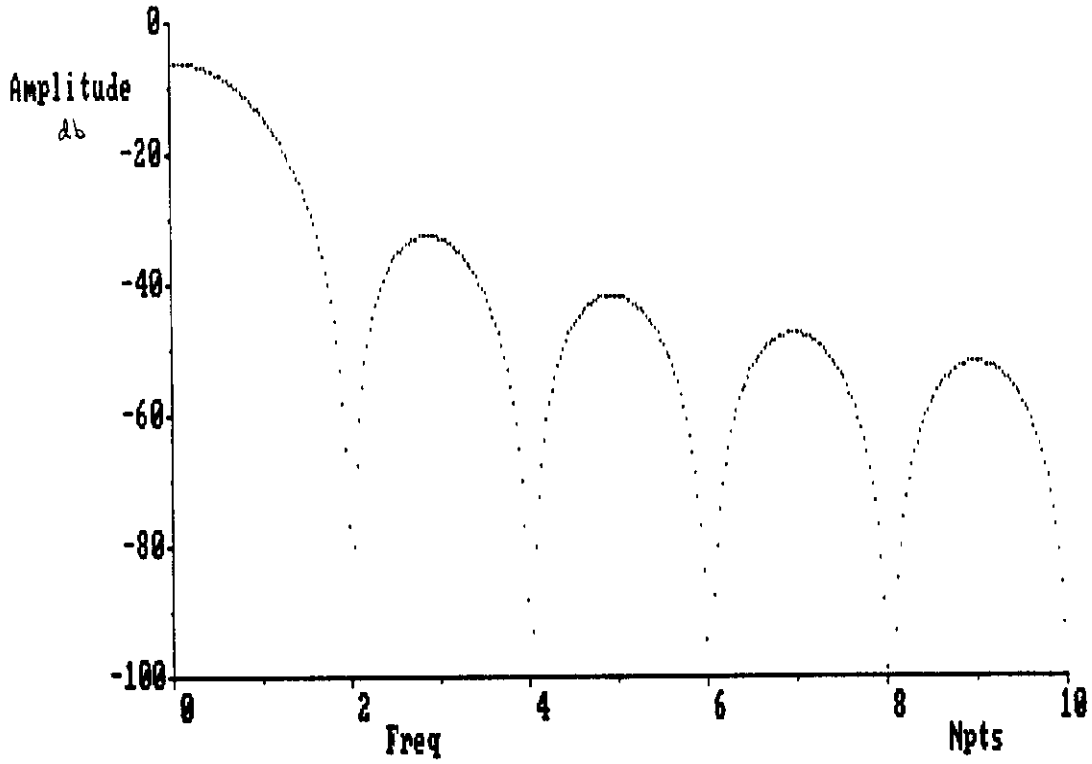


b) Bartlett window

figure 7-1. (continued) Time and frequency domain plots of window functions; a) rectangular, b) Bartlett, c) Hanning, d) Hamming, e) Blackman

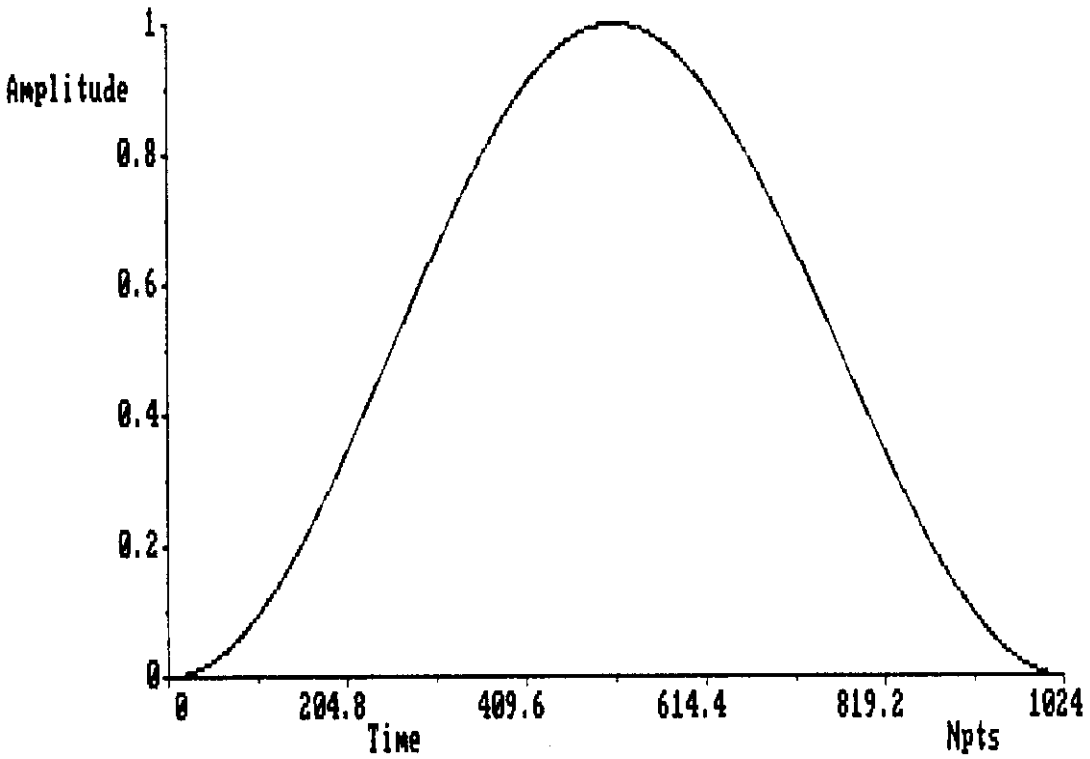


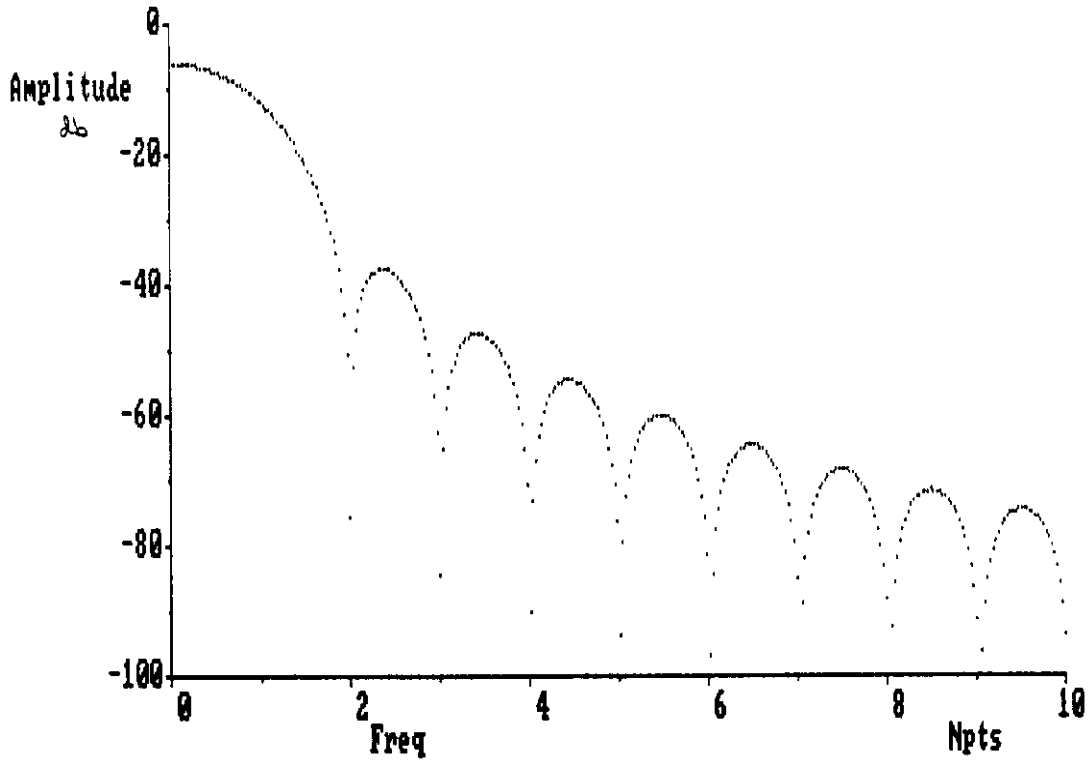


c) Hanning window

figure 7-1. (continued) Time and frequency domain plots of window functions; a) rectangular, b) Bartlett, c) Hanning, d) Hamming, e) Blackman

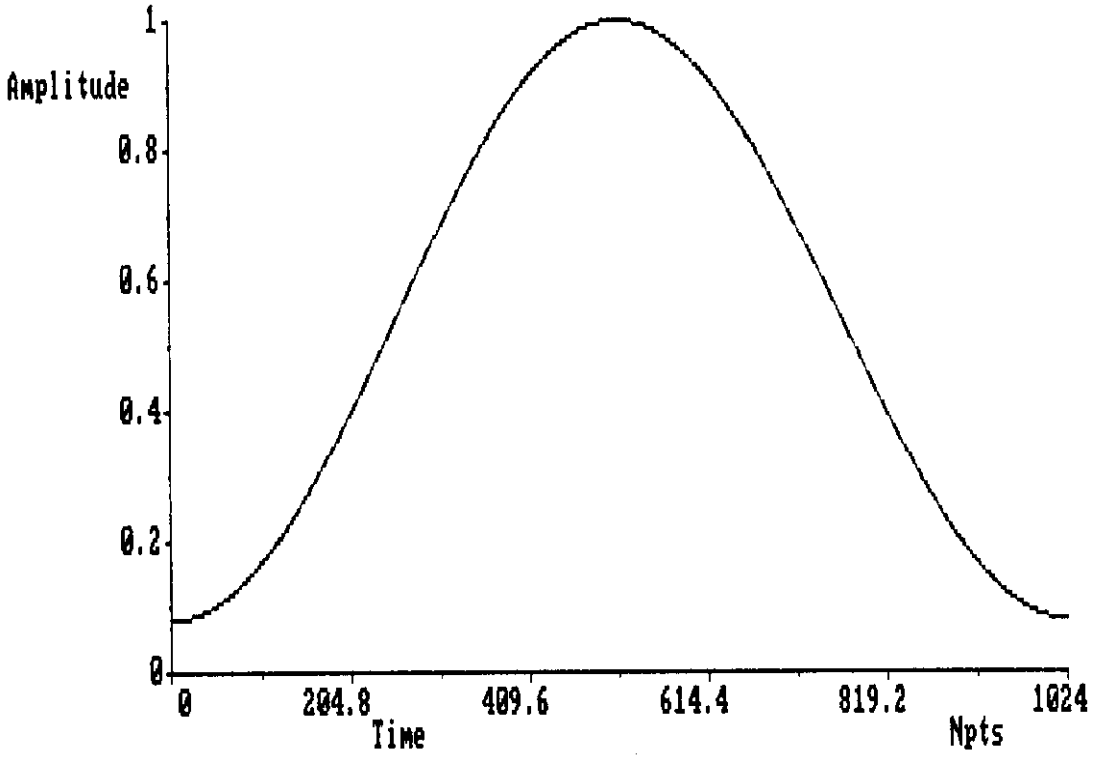


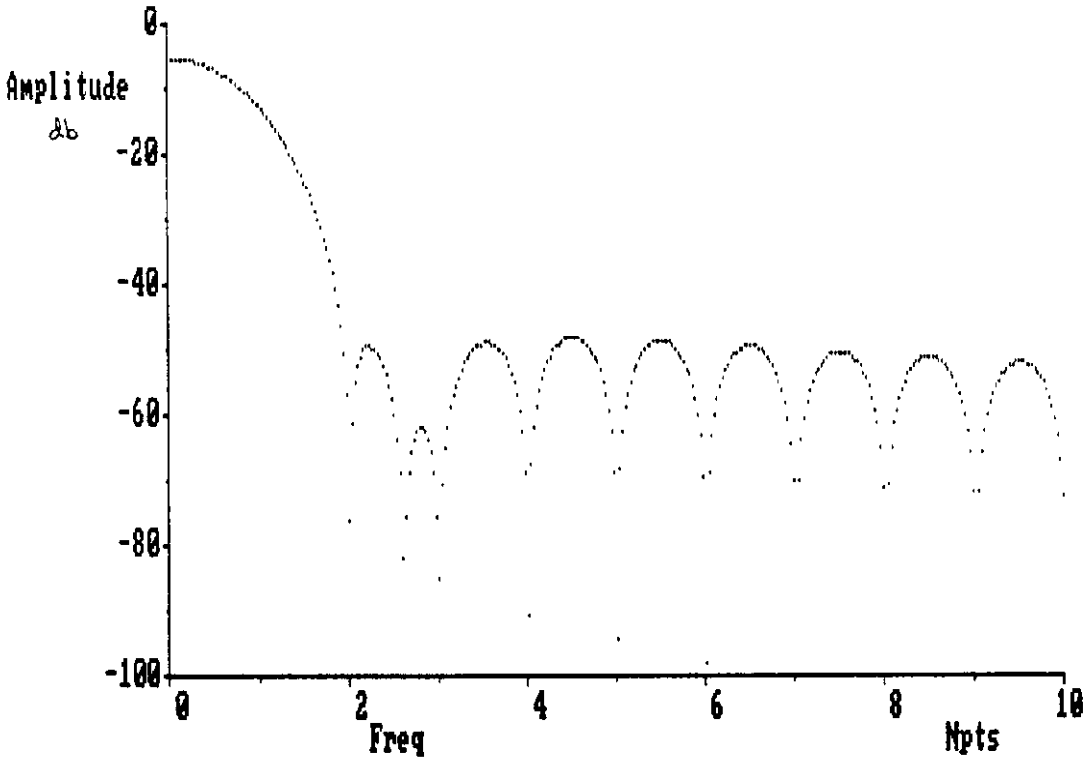


d) Hamming window

figure 7-1. (continued) Time and frequency domain plots of window functions; a) rectangular, b) Bartlett, c) Hanning, d) Hamming, e) Blackman

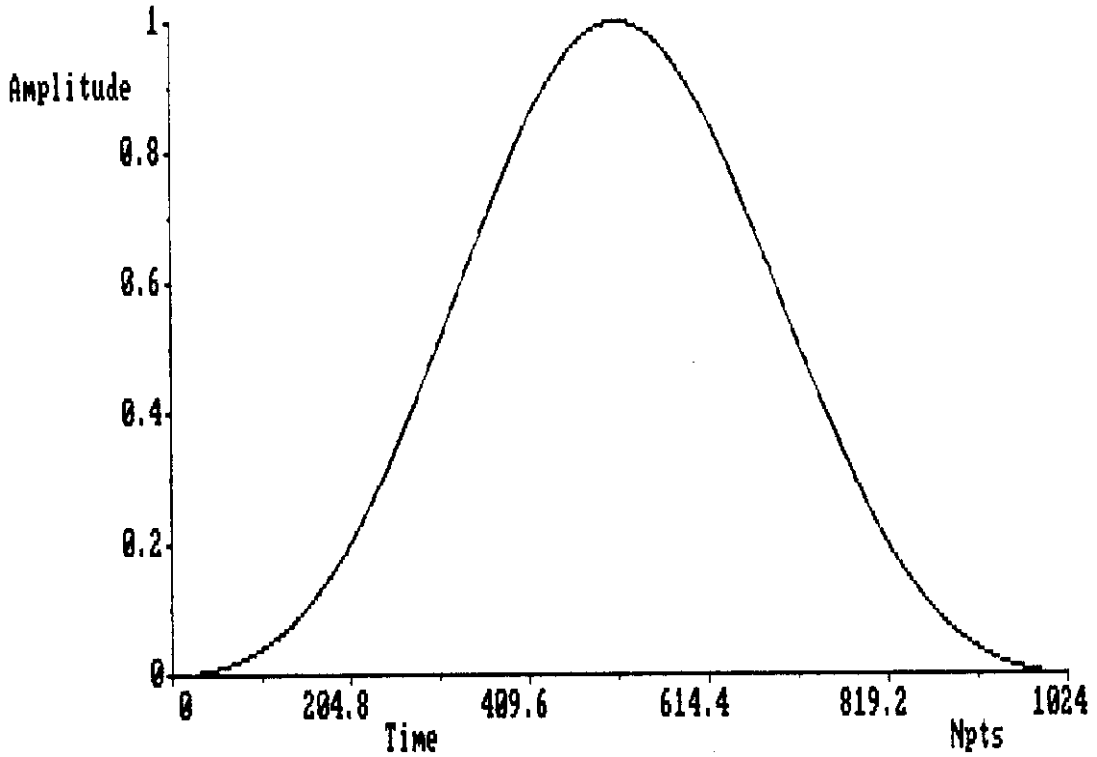


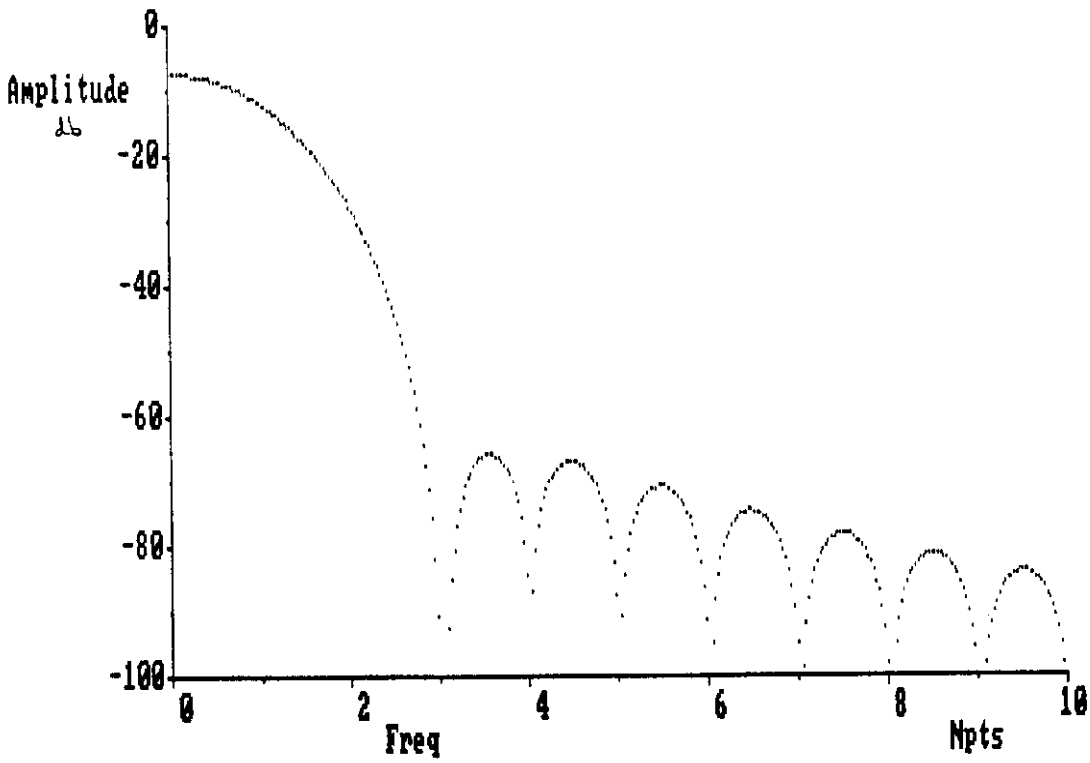


e) Blackman window

figure 7-1. (continued) Time and frequency domain plots of window functions; a) rectangular, b) Bartlett, c) Hanning, d) Hamming, e) Blackman

the total number of time samples, in this case 1024, and dt represents the time spacing between them.

The effect of applying the window, or multiplying in the time domain, can be estimated by mentally convolving the signal's Fourier transform with the window's Fourier transform. Let Fmax = 1/dt and Fres = 1/Ndt. The Fourier transform of a sine wave of frequency Fmax/4 would be a delta function in the frequency domain. The effect of a rectangular window can be obtained from figure (7-1). The delta function would fall exactly on the point N/4 for a fast Fourier transform, since N is a power of 2. Looking at the rectangular window, the neighboring points N/4 + 1, N/4 + 2, ... fall on the zeros of the window's transform. If, on the other hand, the window is applied to a sine wave of frequency Fmax/4 + Fres/2, the neighboring frequency domain points fall half way between the zeros, or on the window's local frequency maximum. The Fourier transform of these two sine waves are shown in figure (7-2). The frequency response of the other windows investigated fall off quicker than the rectangular window. This has the effect of reducing the noise level. The price payed for improving the noise level, or base line, is frequency resolution; compare for example the frequency width of the Blackman window with the rectangular window. This result is intuitive since the resolution is inversely proportional to the sampling period.

Figure (7-3) shows the Fourier transform of the inside back, gaussian excited TM case surface currents. The Blackman window has

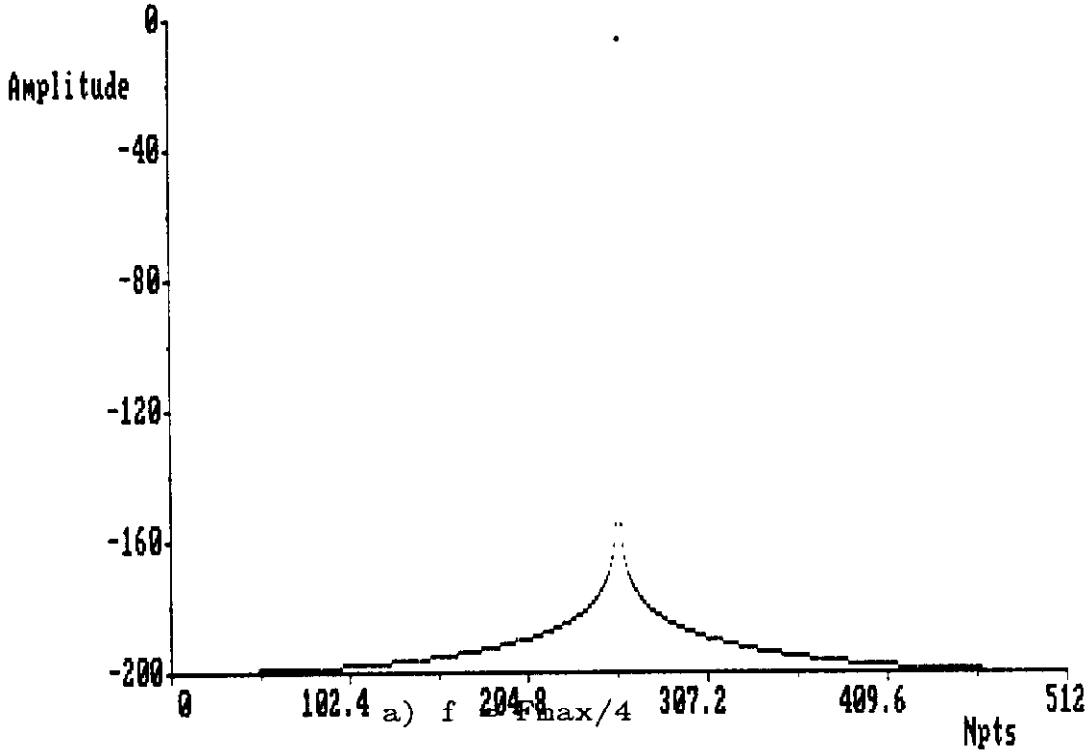


a) f = Fmax/4

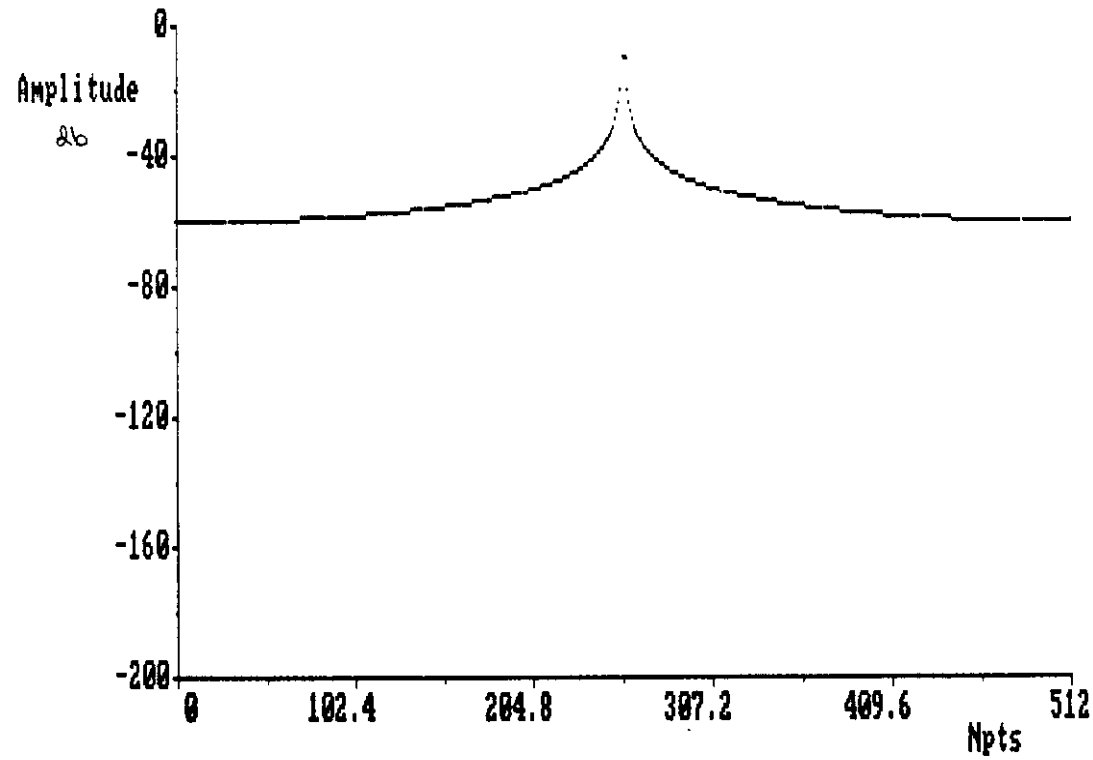


b) f = Fmax/4 + Fres/2

figure 7-2. Fourier transform of sine wave whose frequency is; a) Fmax/4 and b) Fmax/4 + Fres/2

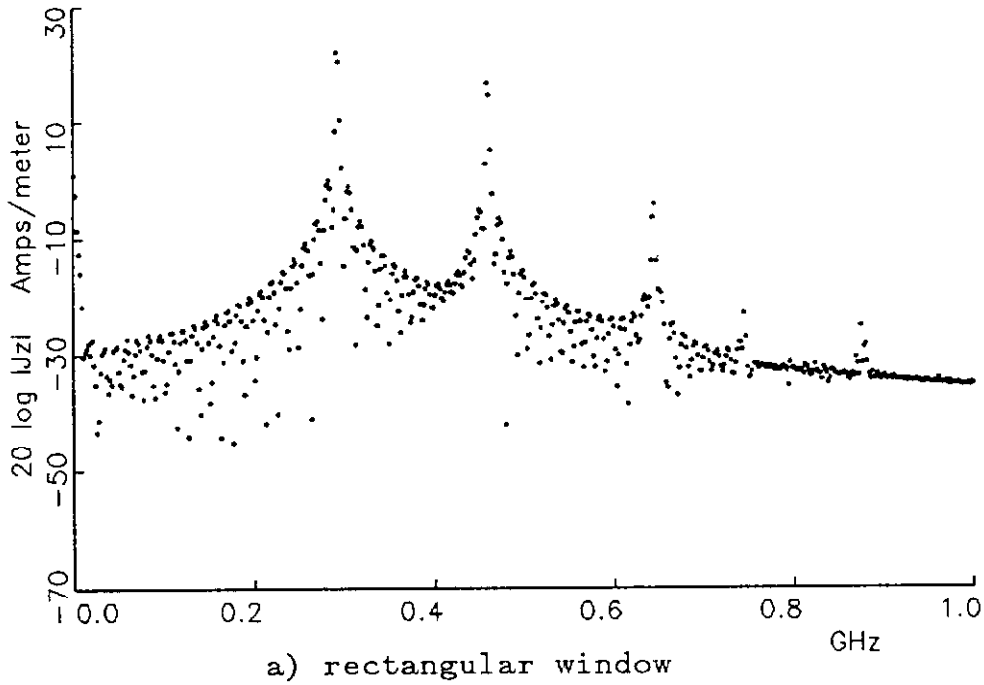


a) rectangular window

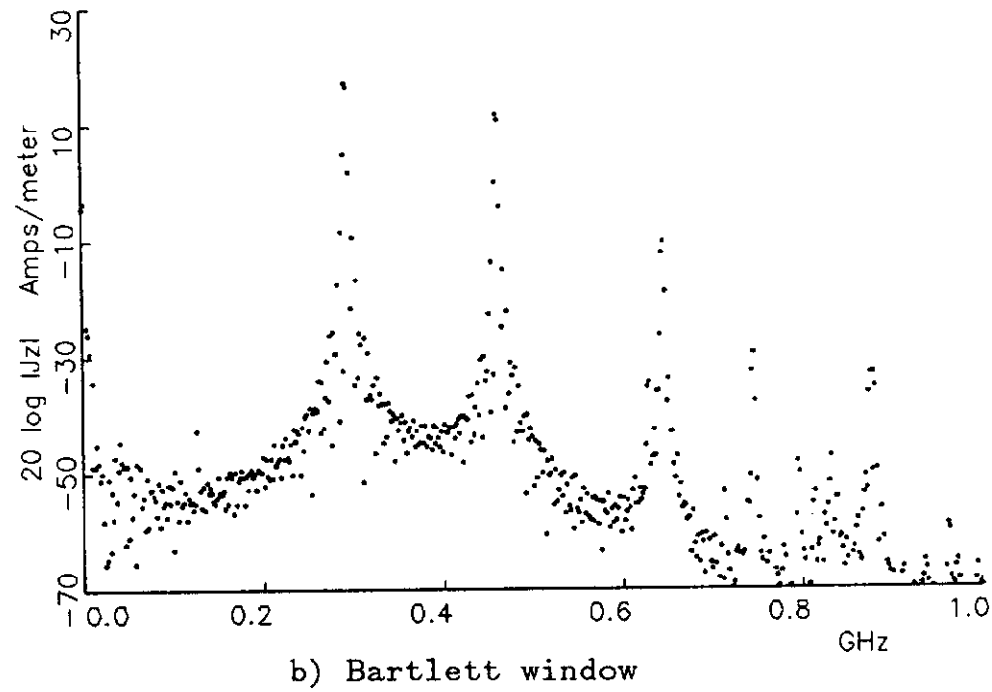


b) Bartlett window

figure 7-3. Comparison of the effect of applying windows prior to the fourier transform of TM mode surface currents at the inside back of the slotted cavity excited with a gaussian pulse; a) rectangular, b) Bartlett, c) Hanning, d) Hamming, e) Blackman

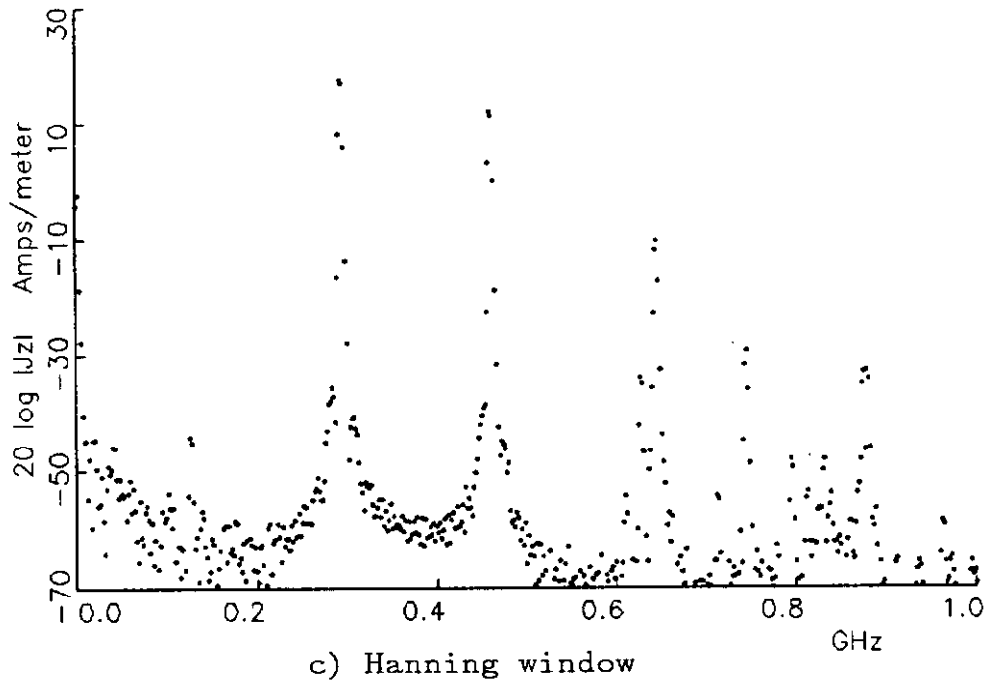


c) Hanning window

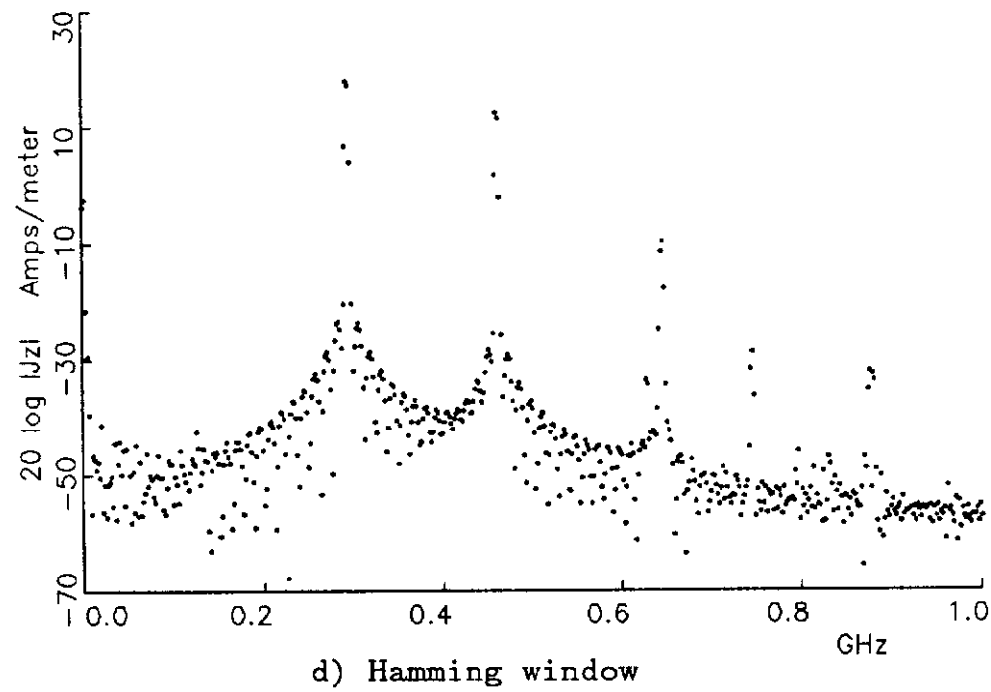


d) Hamming window

figure 7-3. (continued) Comparison of the effect of applying windows prior to the fourier transform of TM mode surface currents at the inside back of the slotted cavity excited with a gaussian pulse; a) rectangular, b) Bartlett, c) Hanning, d) Hamming, e) Blackman

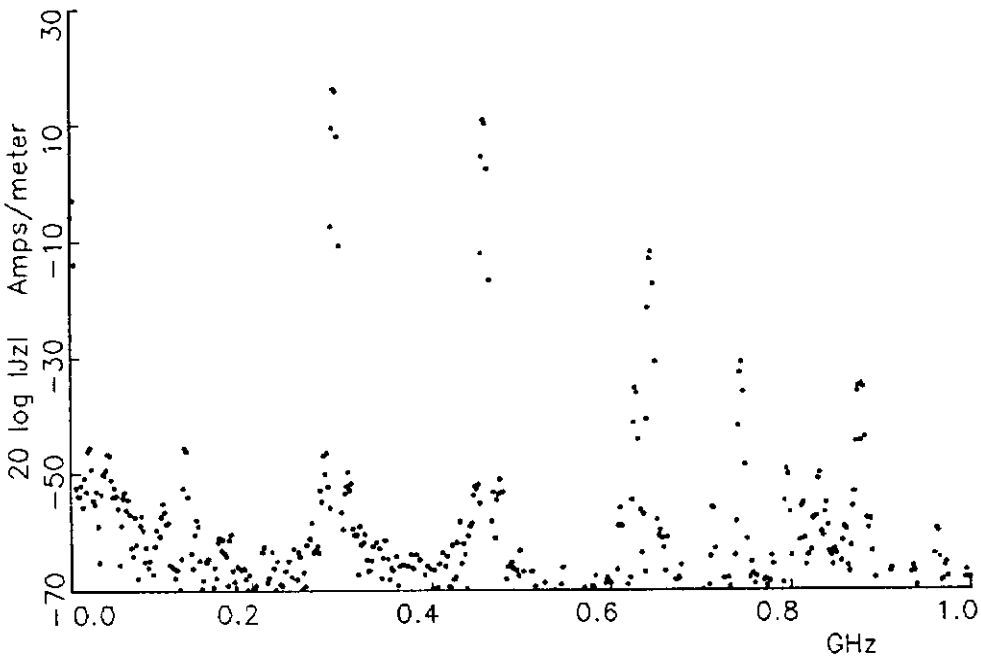


e) Blackman window

figure 7-3. (continued) Comparison of the effect of applying windows prior to the fourier transform of TM mode surface currents at the inside back of the slotted cavity excited with a gaussian pulse; a) rectangular, b) Bartlett, c) Hanning, d) Hamming, e) Blackman

a noise level 30 to 40 db lower than the rectangular window. Also, with this reduced noise level, structure that was not visible with a rectangular window is revealed. The effect of a window depends significantly on the exact frequency content of the original signal. Thus the Blackman window is not necessarily preferable, even though it gave the best results for this particular set of data.

# VIII. CONCLUSION

## 8.1 Single frequency analysis

The biggest problem encountered in single frequency analysis was due to the presence of spurious frequencies in the incident fields. These frequencies are generated by abruptly turning on the source. Because of the causality principal, the falling edge should have no effect.

For two-dimensional TM cases, the pole at zero frequency, caused by an infinite length, can be excited with the zero frequency component of these spurious frequencies. In a shadow region of the scatterer, the DC component was several times larger than the component at the excitation frequency. Because of this the magnitude and phase algorithm failed. For static fields, solutions to Maxwell's curl equations exist which do not satisfy the equations $\nabla \cdot \bar{D} = \rho$ and $\nabla \cdot \bar{B} = 0$.

For either the TE or TM cases the natural modes of the scatterer are excited by these spurious frequencies. For the slotted cavity a natural TM mode only 6 MHz from the driving frequency was excited to essentially the same amplitude as the incident field frequency component. The beat frequency generated from the sum of these two components showed no decay after 5000 time steps of the code indicating a large Q for this mode.

The amplitude of these spurious frequencies can be reduced by slowly turning on the incident fields. Using the rising edge of one of the window functions may prove worthwhile in this regard.

Ideally, the magnitude and phase algorithm would measure the response, or amplitude, of the fields at the frequency of the incident wave only and reject all other frequency components. This infinite frequency resolution would require an infinite time sampling period however. A good topic for further study would be the optimum receiver problem using some minimum amount of additional memory storage. It may prove worthwhile to implement a digital filter and track a few selected field points in the grid. The computation time and memory storage requirements may prohibit its use on all field points.

## 8.2 Transient analysis

Because the FD-TD algorithm works on the field components in place, additional computer storage must be allocated for time domain analysis. For the 46 by 48 cell lattice used in these studies approximately 324 Kbytes of storage was required. This could be reduced to about 108 Kbytes by removing the magnitude and phase algorithm not required for time domain analysis. In order to track all field quantities, 108 Kbytes of storage would be required for every time step or about 540 Mbytes for a 5000 time step run. In order to limit memory requirements, only a few selected points

can be tracked. Care must be used in selecting these points, as they may fall at a null field point for a mode of interest.

Another limiting factor is the amount of computer time required. A 5000 time step run of the 46 by 48 cell lattice required nearly an hour of CPU time on a Vax 8650 computer. The 5000 time steps resulted in a maximum measurable Q of only about 70, for a resonant frequency of 209 MHz.

In order to minimize dispersion, the cell size should be chosen to be about $\lambda/10$ at the highest frequency of interest. The time step size for two-dimensional cases is typically chosen to be $\Delta/2c$. The largest measurable Q for N time steps becomes;

$$Q = \frac{f_o}{\Delta f} = \frac{c}{\lambda}\,\frac{N\lambda}{2c10} = \frac{N}{20}$$

For a cell size of $\lambda/10$, the dispersion, or phase velocity error, will cause a frequency error of about 1%, roughly equivalent to the frequency resolution after 2000 time steps.

The Q of devices in an accelerator can reach several thousand, requiring the order of 40000 time steps, or 8 hours of cpu time, to accurately model. The number of time steps may be reduced by decreasing the cell size, but this would require more time per time step to solve because of the larger lattice. If the structure is excited with a single pulse, at some point the fields will become dominated by numerical noise.

Using windows prior to the application of a Fourier transform reduces frequency resolution. However, it does reduce the noise level in the frequency domain by about 30 db. For the example studied, mode lines were revealed that could not be detected without the window.

The useful bandwidth of the FD-TD algorithm is limited by dispersion. The phase velocity goes to zero between the frequencies of $c/3\Delta$ and $c/2\Delta$, depending on propagation angle. This has the effect of shifting all possible modes of the structure below these frequencies. A gaussian time domain pulse can be selected to excite the frequencies of interest while minimizing the amount of energy at these FD-TD cut off frequencies. This frequency limit is less than the one imposed by the time step size. The bandwidth available from a Fourier transform is given by $c/\Delta$; thus one could average groups of three successive time points prior to the application of the transform. The resulting frequency resolution would be unchanged but the transform would work on three times fewer points.

## 8.3 Advantages of computer modeling

At the current time, both the MOM and FD-TD algorithms are limited by computer speed and memory storage requirements. The alternative is to physically construct a model and test it. The cost of equipment and construction can be significant. Depending on the requirements, the time necessary for construction, testing,

and interpreting the results could outweigh that of an equivalent computer model.

A distinct advantage of computer modeling is that fields can be obtained without disturbing them. In order to excite or measure fields in a physical structure, some type of probe is required. The fields can be estimated by measuring the effect of pulling or dropping dielectric beads through an excited cavity or by measuring the impedance of a stretched wire. In both cases the presence of the probe must be taken into account when interpreting the results. Small antennas in the form of loops or studs may be used to measure fields directly. Their gain must be measured or calibrated at each frequency of interest and again their presence will load the cavity fields.

Even with current computer limitations both the MOM and FD-TD algorithms prove a powerful tool. As computer technology continues to grow their usefulness will only improve.

# CITED LITERATURE


1. Cooper, R. k., Menzel, M. T., Stokes, H. K. and Warren, J. L. : New Documentation From the Los Alamos Accelerator Code Group. Proc. 1987 IEEE Part. Acc. Conf., CH2387-9: 1780-1782, 1987.

2. Engquist, B. and Majda, A.: Absorbing Boundary Conditions for the Numerical Simulation of Waves. Math. Comp. Vol. 31: 629-651, 1977.

3. Harrington, R.F.: Field Computation by Moment Methods. New York, Macmillan, 1968.

4. Harrington, R.F.: Time-Harmonic Electromagnetic Fields. New York, McGraw-Hill, 1961.

5. Liao, S. Y.: Microwave Devices and Circuits. Englewood Cliffs, Prentice-Hall, 1980.

6. Mur, G. : Absorbing Boundary Conditions for the Finite-Difference Approximation of the Time-Domain Electromagnetic Field Equations. IEEE Trans. Electromagn. Compat. Vol. EMC-23: 377-382, 1981.

7. Oppenheim and Schaffer: Digital Signal Processing. Englewood Cliffs, Prentice-Hall, 1975.

8. Stahl, S. and Bogacz, S. A.: Coupled-Bunch Instability in a Circular Accelerator and Possible Cures: Longitudinal-Phase-Space Simulation. Phys. Rev. Vol. 37 No. 5: 1300-1306, 1988.

9. Taflove, A. and Umashankar, K. R.: Finite-Difference Time-Domain (FD-TD) Modeling of Electromagnetic Wave Scattering and Interaction Problems. IEEE Antennas Prop. Newsletter: 5-20, April 1988.

10. Taflove, A. and Umashankar, K.: Users Code for the Finite-Difference Time-Domain Method. Final Technical Report to Rome Air Development Center, Griffiss Air Force Base, NY, RADC-TR-82-16: 1982.

11. Taflove, A., Umashankar, K. R. and Jurgens, T. G.: Validation of FD-TD Modeling of the Radar Cross Section of Three-Dimensional Scatterers Spanning up to Nine Wavelengths. IEEE Trans. Antennas Prop. Vol. AP-33: 662-666, 1985.

12. Trefethen, L. N. and Halpern, L.: Well-Posedness of One-Way Wave Equations and Absorbing Boundary Conditions. Inst. Comput. Appl. Sci. and Eng. (ICASE), NASA Langley Res. Center, Hampton, VA, Report 85-30, 1985.

CITED LITERATURE (continued)

13. Taflove, A. and Umashankar, K.: Advanced Numerical Modeling of Microwave Penetration and Coupling for Complex Structures. Final technical report to Lawrence Livermore National Laboratory, Contract No. 6599805, 1987.

14. Weiland T.: Computer Modelling of Two and Three-Dimensional Cavities. IEEE Trans. Nuc. Sci. Vol. NS-32 No. 5: 2738-2742, 1985.

15. Weiland T.: On the Numerical Solution of Maxwell's Equations and Applications in the Field of Accelerator Physics. Part. Acc. Vol. 15: 245-292, 1984.

16. Weiland T.: On the Unique Numerical Solution of Maxwellian Eigenvalue Problems in Three Dimensions. Part. Acc. Vol. 17: 227-242, 1985.

17. Weiland T.: TBCI and Urmel - New Computer Codes for Wake Field and Cavity Mode Calculations. IEEE Trans. Nuc. Sci. Vol. NS-32 No. 5: 2738-2742, 1985.

18. Yee, K. S.: Numerical Solution of Initial Boundary Value Problems Involving Maxwell's Equations in Isotropic Media. IEEE Trans. Antennas Prop., AP-14: 302-307, 1966.